The Astronomical Journal, 165:134 (36pp), 2023 March https://doi.org/10.3847/1538-3881/acb4e3

Characterization of a Set of Small Planets with TESS and CHEOPS and an Analysis of Photometric Performance

Dominic Oddo[1], Diana Dragomir[1], Alexis Brandeker[2], Hugh P. Osborn[3,4], Karen Collins[5], Keivan G. Stassun[6], Nicola Astudillo-Defru[7], Allyson Bieryla[5], Steve B. Howell[8], David R. Ciardi[9], Samuel Quinn[5], Jose M. Almenara[10], César Briceño[11], Kevin I. Collins[12], Knicole D. Colón[13], Dennis M. Conti[14], Nicolas Crouzet[15], Elise Furlan[9], Tianjun Gan[16], Crystal L. Gnilka[8], Robert F. Goeke[3], Erica Gonzales[17], Mallory Harris[1], Jon M. Jenkins[8], Eric L. N. Jensen[18], David Latham[5], Nicholas Law[19], Michael B. Lund[9], Andrew W. Mann[19], Bob Massey[20], Felipe Murgas[21,22], George Ricker[23,24], Howard M. Relles[5], Pamela Rowden[25], Richard P. Schwarz[5], Joshua Schlieder[26], Avi Shporer[3], Sara Seager[23,27,28], Gregor Srdoc[29], Guillermo Torres[5], Joseph D. Twicken[8,30], Roland Vanderspek[3], Joshua N. Winn[31], and Carl Ziegler[32]

[1] Department of Physics and Astronomy, University of New Mexico, 210 Yale Boulevard NE, Albuquerque, NM 87106, USA; doddo@unm.edu
[2] Department of Astronomy, Stockholm University, AlbaNova University Center, SE-10691 Stockholm, Sweden
[3] Department of Physics and Kavli Institute for Astrophysics and Space Research, Massachusetts Institute of Technology, Cambridge, MA 02139, USA
[4] NCCR/Planet-S, Universität Bern, Gesellschaftsstrasse 6, 3012 Bern, Switzerland
[5] Center for Astrophysics, Harvard & Smithsonian, 60 Garden Street, Cambridge, MA 02138, USA
[6] Department of Physics and Astronomy, Vanderbilt University, Nashville, TN 37235, USA
[7] Departamento de Matemática y Física Aplicadas, Universidad Católica de la Santísima Concepción, Alonso de Rivera 2850, Concepción, Chile
[8] NASA Ames Research Center, Moffett Field, CA 94035, USA
[9] NASA Exoplanet Science Institute, Caltech/IPAC, Pasadena, CA 91125, USA
[10] Univ. Grenoble Alpes, CNRS, IPAG, F-38000 Grenoble, France
[11] Cerro Tololo Inter-American Observatory, Casilla 603, La Serena, Chile
[12] George Mason University, 4400 University Drive, Fairfax, VA 22030, USA
[13] NASA Goddard Space Flight Center, Greenbelt, MD 20771, USA
[14] American Association of Variable Star Observers, 185 Alewife Brook Parkway, Suite 410, Cambridge, MA 02138, USA
[15] Leiden Observatory, Leiden University, Postbus 9513, 2300 RA, Leiden, The Netherlands
[16] Department of Astronomy and Tsinghua Centre for Astrophysics, Tsinghua University, Beijing 100084, People's Republic of China
[17] Department of Astronomy and Astrophysics, University of California, Santa Cruz, Santa Cruz, CA, USA
[18] Department of Physics & Astronomy, Swarthmore College, Swarthmore, PA 19081, USA
[19] Department of Physics and Astronomy, The University of North Carolina at Chapel Hill, Chapel Hill, NC 27599-3255, USA
[20] Villa '39 Observatory, Landers, CA 92285, USA
[21] Instituto de Astrofísica de Canarias (IAC), E-38205 La Laguna, Tenerife, Spain
[22] Departamento de Astrofísica, Universidad de La Laguna (ULL), E-38206 La Laguna, Tenerife, Spain
[23] MIT Kavli Institute for Astrophysics and Space Research, Massachusetts Institute of Technology, Cambridge, MA 02139, USA
[24] MIT Department of Physics, Massachusetts Institute of Technology, Cambridge, MA 02139, USA
[25] Royal Astronomical Society, Burlington House, Piccadilly, London W1J 0BQ, UK
[26] Goddard Space Flight Center, National Aeronautics and Space Administration, Greenbelt, USA
[27] Earth and Planetary Sciences, Massachusetts Institute of Technology, 77 Massachusetts Avenue, Cambridge, MA 02139, USA
[28] Department of Aeronautics and Astronautics, MIT, 77 Massachusetts Avenue, Cambridge, MA 02139, USA
[29] Kotizarovci Observatory, Sarsoni 90, 51216 Viskovo, Croatia
[30] SETI Institute, Mountain View, CA 94043, USA
[31] Department of Astrophysical Sciences, Princeton University, 4 Ivy Lane, Princeton, NJ 08544, USA
[32] Department of Physics, Engineering and Astronomy, Stephen F. Austin State University, 1936 North St, Nacogdoches, TX 75962, USA
Received 2022 October 7; revised 2022 December 23; accepted 2023 January 15; published 2023 February 28

Abstract

The radius valley carries implications for how the atmospheres of small planets form and evolve, but this feature is visible only with highly precise characterizations of many small planets. We present the characterization of nine planets and one planet candidate with both NASA TESS and ESA CHEOPS observations, which adds to the overall population of planets bordering the radius valley. While five of our planets—TOI 118 b, TOI 262 b, TOI 455 b, TOI 560 b, and TOI 562 b—have already been published, we vet and validate transit signals as planetary using follow-up observations for four new TESS planets, including TOI 198 b, TOI 244 b, TOI 444 b, and TOI 470 b. While a three times increase in primary mirror size should mean that one CHEOPS transit yields an equivalent model uncertainty in transit depth as about nine TESS transits in the case that the star is equally as bright in both bands, we find that our CHEOPS transits typically yield uncertainties equivalent to between two and 12 TESS transits, averaging 5.9 equivalent transits. Therefore, we find that while our fits to CHEOPS transits provide overall lower uncertainties on transit depth and better precision relative to fits to TESS transits, our uncertainties for these fits do not always match expected predictions given photon-limited noise. We find no correlations between number of equivalent transits and any physical parameters, indicating that this behavior is not strictly systematic, but rather

might be due to other factors such as in-transit gaps during CHEOPS visits or nonhomogeneous detrending of CHEOPS light curves.

Unified Astronomy Thesaurus concepts: Exoplanet astronomy (486); Extrasolar rocky planets (511); Mini Neptunes (1063)

Supporting material: figure sets

1. Introduction

The number of officially confirmed and validated exoplanets has now exceeded 5200.[33] Because of this substantial sample size, our knowledge of exoplanetary systems, their properties, and formation and evolutionary processes has greatly expanded in the past three decades. It is now known that the distribution of planet radii between the size of Earth and Neptune is bifurcated in two distinct populations: super-Earths and sub-Neptunes (Parviainen & Aigrain 2015; Fulton & Petigura 2018; Berger et al. 2020; Petigura et al. 2022). Super-Earths are those planets that have radii between one and 1.5 times that of Earth and have densities indicative of rocky compositions (Dressing et al. 2015), whereas sub-Neptunes have radii between two and 3.5 times that of Earth and have relatively lower densities (Chouqar et al. 2020; Bean et al. 2021), suggesting different formation/evolution pathways for these different populations (Swain et al. 2019; Luque & Pallé 2022). Therefore, "the radius valley," as it is called, is the result of physical processes that shape this feature in the distribution of planet radii.

Large populations of precisely characterized planets are required to resolve the valley (MacDonald 2019; Petigura et al. 2022). The NASA Transiting Exoplanet Survey Satellite (TESS; Ricker et al. 2014) mission is poised to deliver on this requirement via its full-sky observations of transiting exoplanets, making it the largest survey for transiting exoplanets to date. Meanwhile, the ESA CHaracterizing ExOPlanets Satellite (CHEOPS; Broeg et al. 2013; Benz et al. 2021) is a larger space telescope, launched in 2019 December, with a 32 cm aperture for the purpose of precision follow-up of known planetary systems. CHEOPS has the capability to improve radius measurements and orbital properties of planets it observes. Thus, when these two photometric telescopes are used in tandem, further insights into important physical phenomena that govern the characteristics of known planets may be gleaned.

There is a growing sample of systems that have been observed by both TESS and CHEOPS, for which ultra-high-precision measurements are important. For example, these observations have illuminated properties of planets in multi-planet systems (Bonfanti et al. 2021; Hoyer et al. 2022; Serrano et al. 2022; Wilson et al. 2022), young planetary systems (Zhou et al. 2022), phase curves of KELT-1b (Parviainen et al. 2022), and spin–orbit misalignment of planets orbiting rapidly rotating stars (Garai et al. 2022), among others. These observations require precision on the ∼tens of ppm scales in order to draw meaningful conclusions. Given the different sizes of the primary apertures of these telescopes, it is reasonable to expect varying photometric performances from these telescopes, but quantifying these deviations has not yet been explored fully. Previous work comparing these telescopes has found that for a $V \approx 9$ mag solar-like star and a transit signal of ≈500 ppm, one CHEOPS transit is equivalent in photometric precision to eight TESS transits combined (Bonfanti et al. 2021). We expand on this by writing formalism for comparison between the two, which is presented in Section 6.3.

We present the characterization of 10 systems that were initially detected by TESS and subsequently observed by CHEOPS, including the validation of four new TESS planets. These are systems that host small planets that may border the radius valley, but whose properties were poorly constrained prior to their observations with CHEOPS. In this work, we present the largest single sample to date of planets that were observed by both of these telescopes and analyzed homogeneously. Importantly, our sample size gave us the opportunity to compare the relative photometric performances of TESS and CHEOPS, in addition to measuring the properties of these planets. We investigated the possibility that system properties are not influenced by our analysis by modeling and fitting with three different methods. We compare system properties and uncertainties on these values as a metric for the photometric performance of these telescopes.

Out of our 10 systems, five of them were already published as validated/confirmed planets. We attempted to validate five new planets in this work, but were only able to do so for four out of those five. Given the evidence presented in Section 4.5, we were not able to conclusively validate the planet candidate TOI 518.01. In our vetting process, we make use of follow-up observations for each of these new planets, including high-resolution imaging, ground-based photometric follow-up, and reconnaissance spectroscopic radial velocity (RV) characterization.

We describe photometric observations with TESS and CHEOPS in Section 2, along with other follow-up observations that were performed in order to validate new planets. We present our sample of systems in Section 3, including host star properties and how these values were derived. Next, we validate the systems that have not yet been validated in Section 4. We present our fitting and modeling of TESS and CHEOPS photometry in Section 5. We then discuss results in Section 6 and present our discussion in Section 7, concluding and summarizing in Section 8.

1.1. Target Selection

Here we describe how we selected the sample of TESS objects of interest (TOIs) for which we obtained CHEOPS observations. The main science goal of the CHEOPS proposals was to better constrain the density and bulk composition of small TESS planets, so we only selected TOIs smaller than 5 $R_{\rm Earth}$, and for which one or two CHEOPS transits were expected to substantially improve the precision on the planet radius measurement available at the time of proposal submission. We also ensured the TOIs had already undergone reconnaissance spectroscopic and photometric follow-up to rule out eclipsing binaries as the source of the transit signal.

We then applied two cuts based on brightness (G mag < 12 as recommended by the CHEOPS Announcement of

[33] From NASA Exoplanet Archive, https://exoplanetarchive.ipac.caltech.edu/ (NASA Exoplanet Science Institute 2020).

Table 1
TESS Observations of the Systems Presented Here

TOI ID	TIC ID	TESS Sectors	PM Cadence	EM Cadence	Camera-CCD	R.A.	Decl.
TOI 118	TIC 266980320	[1,28]	2 minutes	2 minutes	2–2	23:18:14.22	−56:54:14.35
TOI 198	TIC 12421862	[2,29]	2 minutes	2 minutes	1–2	00:09:05.16	−27:07:18.28
TOI 244	TIC 118327550	[2,29]	2 minutes	20 s	2–3	00:42:16.74	−36:43:04.71
TOI 262	TIC 70513361	[3,30]	2 minutes	2 minutes	2–3	02:10:08.32	−31:04:14.26
TOI 444	TIC 179034327	[4,5,31,32]	2 minutes	2 minutes	2–1 and 2–2	04:16:44.16	−26:45:59.07
TOI 455	TIC 98796344	[4,31]	2 minutes	20 s	2–4	03:01:50.99	−16:35:40.18
TOI 470	TIC 37770169	[6,33]	2 minutes	2 minutes	2–2 and 2–1	06:16:02.38	−25:01:53.08
TOI 518	TIC 264979636	[7,34[a]]	2 minutes	2 minutes	1–4	07:42:52.03	+08:52:00.86
TOI 560	TIC 101011575	[8,34]	2 minutes	2 minutes	2–3 and 2–4	08:38:45.19	−13:15:23.50
TOI 562	TIC 413248763	[8,35]	2 minutes	2 minutes	2–3	09:36:01.79	−21:39:54.23

Note.
[a] Poor data quality, not used.

Opportunity (AO) policies and procedures) and CHEOPS observability at a minimum of 50% efficiency. Lastly, we removed any targets found on the CHEOPS guaranteed time observing (GTO) program reserved target list at the time of proposal submission. The final sample for which we obtained CHEOPS observations consists of 10 TOIs.

2. Observations

In this section, we outline the observations of our targets, including with TESS and CHEOPS for all targets. For those targets that have not yet been validated, we briefly outline additional observations in Section 2.3.

2.1. TESS

TESS is a spacecraft with four telescopes conducting an all-sky survey of nearby bright stars in search of transiting exoplanets (Ricker et al. 2014). It was launched in 2018 April and systematically surveys 24 deg × 96 deg portions of the sky, called sectors, for approximately 27 days at a time. During its two-year primary mission (PM), it observed both the southern and northern ecliptic skies in 13 sectors each, for a total of 26 sectors. It followed a similar path during its 27-month first extended mission (EM1), part of whose purpose is to provide additional follow-up and shorter cadence observations of targets that were observed in the PM (its sky pattern in EM1 was slightly different, encompassing more of the ecliptic than in the PM). As such, each of our targets was observed in at least two TESS sectors, including the PM and the EM1. As of 2022 September, the second extended mission (EM2) had begun, but this work relies only on the PM and EM1.

To maximize sky coverage, visibility, and stability, TESS is on a 13.7-day lunar-resonant eccentric orbit (Gangestad et al. 2013). In the PM and EM1, it remained pointed at the same part of the sky for two orbits at a time, with data downlink between the two orbits, leading to regular data gaps in the middle of TESS sectors. The 2048 × 2048 imaging area on each CCD has a pixel scale of about $21''\,\mathrm{pix}^{-1}$. Pixel readout occurs continuously at 2 s cadence, which is then stacked to either two-minute postage stamps for 20,000 preselected targets[34] for each sector or 30-minute full frame images (FFIs) for the full field in the PM. During the EM1, FFI cadence was reduced from 30 to 10 minutes, and there were an additional 1000 preselected targets at 20 s cadence, along with 20,000 preselected two-minute targets. The number of preselected targets observed at 20 s cadence increased to 1300 by the end of EM1.

All of the systems that are the subject of this work were first observed by TESS during year one of its PM. All of our targets in the TESS Input Catalog (TIC; Stassun et al. 2018, 2019) were observed at two-minute cadence in the PM. TESS observations for these systems were processed by both the Science Processing Operations Center (SPOC; Jenkins et al. 2016) at NASA Ames Research Center and the Massachusetts Institute of Technology (MIT) Quick-Look Pipeline (QLP; Huang et al. 2020a, 2020b). SPOC and QLP are both pipelines for extracting light curves, except QLP extracts light curves exclusively from FFIs. These systems were flagged as potential candidates by either SPOC or QLP, vetted by the TESS vetting team, and designated as TOIs (Guerrero et al. 2021). Each of these TOIs was then reobserved by TESS in its EM1, providing a longer baseline of photometric observations, which refined uncertainties in the periods of our targets, as well as other parameters such as transit depth and planet radius. Eight of our systems were observed at two-minute cadence again, but TOI 244 and TOI 455 were observed at 20 s cadence in the EM1, as shown in Table 1. We used the shortest available cadence for all of our analysis, meaning we used two-minute-cadence light curves for a majority of our TESS light curves, but used 20 s cadence light curves for TOI 244 and TOI 455.

Because all of our targets were selected for observation in short cadence, we analyzed short cadence SPOC light curves for all of our systems. Additionally, SPOC applies Presearch Data Conditioning to its light curves, which were extracted via Presearch Data Conditioning Simple Aperture Photometry (PDCSAP), a procedure initially developed for the Kepler mission (Smith et al. 2012; Stumpe et al. 2012, 2014). We chose to work with PDCSAP light curves for our analysis, which is assumed to be corrected for instrumental effects.

A DOI for these TESS observations has been created and is hosted by MAST at the following web address: doi:10.17909/dshz-jz09.

2.2. CHEOPS

The CHEOPS mission is a European Space Agency small-class mission dedicated to studying bright, nearby exoplanet host stars for the purpose of making high-precision observations of transiting super-Earth and sub-Neptune planets. It was

[34] Lists of two-minute and 20 s cadence targets: https://tess.mit.edu/observations/target-lists/.

Table 2
Details of CHEOPS Visits for all Targets, Including Month of Observation, Visit Duration in Hours, Number of Frames, Observing Efficiency as Reported by the DRP, and MAD

TOI ID	Obs. Date	Visit Duration (hr)	Number of Frames	Efficiency (%)	MAD (ppm)
118	2021 Aug	7.4	305	68.5%	257
198	2021 Sep	8.4	472	93.4%	611
244	2021 Oct	10.9 and 10.6	484 and 488	73.7% and 76.3%	741 and 602
262	2020 Oct	16.2	1441	83.2%	205
444	2020 Dec	14.9	815	90.9%	252
455	2020 Oct	6.5	357	91.7%	278
470	2020 Dec	6.3	365	96.5%	588
518	2021 Dec and 2022 Mar	8.1 and 7.5	299 and 291	61.4% and 64.6%	406 and 443
560	2021 Jan	5.0	224	72.7%	215
562	2022 Mar	6.5	359	92.2%	358

launched in 2019 December and is currently in a Sun-synchronous orbit ∼700 km above Earth. There are two consequences of CHEOPS's orbital configuration that manifest themselves in our observations. First, the low-Earth orbit of the spacecraft renders certain parts of the sky unobservable by CHEOPS, but importantly this also means that stray light from the Earth will sometimes surpass acceptable levels during observation, leading to gaps in the data at these times. As such, there is an associated observing efficiency associated with each CHEOPS observation, which is the fraction of the observation that is successfully retained. Second, given its nadir-locked orbit (i.e., the *Z*-axis of the spacecraft is antiparallel to the nadir direction), the field of view rotates about the central optical axis with the same period as the spacecraft orbit.

We proposed five of these targets for observation in CHEOPS's first Announcement of Opportunity (AO-1), which spanned the period from 2020 March to 2021 March. We proposed a similar campaign for the remaining targets on our list in AO-2, which spanned the following year, from 2021 March to 2022 March.

Our observations were processed by the CHEOPS Data Reduction Pipeline (DRP; Hoyer et al. 2020), which calibrates and corrects for instrumental and environmental effects, such as bias, gain, and flat-fielding. The DRP performs three main functions, which are calibration, correction, and photometry. The calibration phase corrects for instrumental response, the correction phase accounts for environmental effects (such as stray light or cosmic rays), and the photometry phase transforms the calibrated and corrected images into light curves. The calibration phase consists of standard CCD reduction, including corrections for bias, gain, dark current, and flat-fielding. The correction phase accounts for smearing, bad pixels, depointing, pixel to sky mapping, and background and stray light. Finally, the DRP produces aperture photometry for radii from 15 up to 40 pixels.

In addition to DRP aperture photometry, we extracted light curves from our CHEOPS visits with the point-spread function (PSF) photometry package `PIPE`[35] developed specifically for CHEOPS (Brandeker et al. 2023, in preparation; see also descriptions in Szabó et al. 2021 and Morris et al. 2021), which has been proven to produce light curves consistent with aperture photometry but less affected by background stars (Serrano et al. 2022). Briefly, `PIPE` derives the PSF from the imagettes returned by the telescope, and then fits the PSF to each image cutout, i.e., imagette, to yield a light curve. PSF photometry has the advantage of reducing background noise from nearby stars relative to aperture photometry. Light curves generated with `PIPE` exhibited lower median absolute deviation (MADs) than those generated by the DRP. Therefore, we chose to use `PIPE` light curves for all of our CHEOPS visits, with the exception of TOI 455 because it is part of a highly blended stellar system. Our observations are described in Table 2, and our CHEOPS light curves are shown in Appendix B. Additionally, all of our CHEOPS detrended and raw extraction light curves are publicly available on online (ExoFOP TESS).[36]

2.3. Follow-up Observations

Here, we detail our follow-up observations, which were acquired to vet and validate the planetary signals for new systems.

2.3.1. Precise RVs of TOI 198 with VLT-ESPRESSO

From 2019 July 4th to September 12th, we acquired 23 spectra of TOI 198 with Echelle SPectrograph for Rocky Exoplanets and Stable Spectroscopic Observations (ESPRESSO) under ESO program-id 0103.C-0849(A). The spectrograph is stabilized in pressure and temperature for precise radial velocity measurements, operating in the wavelength domain from 380 to 788 nm with a resolving power of 140,000 in the high-resolution mode used here (Pepe et al. 2013). The raw data were reduced with the ESO dedicated pipeline and radial velocities were computed by a template-matching approach following Astudillo-Defru et al. (2017). That is, we obtained an enhanced signal-to-noise ratio (S/N) spectrum from all available spectra that is Doppler shifted in radial velocity where tellurics were neglected. Then we maximize the likelihood between individual spectra and the template to obtain the radial velocity, whose uncertainty is derived following Bouchy et al. (2001). These RVs are given in Table 7.

2.3.2. Reconnaissance Spectra with FLWO-TRES and CTIO/SMARTS-CHIRON

Reconnaissance spectra were obtained with the Tillinghast Reflector Echelle Spectrograph (TRES; Fűrész 2008), which is mounted on the 1.5 m Tillinghast Reflector Telescope at the

[35] https://github.com/alphapsa/PIPE

[36] https://exofop.ipac.caltech.edu/tess/

Fred Lawrence Whipple Observatory (FLWO) atop Mount Hopkins, in Arizona. TRES is an optical, fiber-fed echelle spectrograph with a wavelength range of 390–910 nm and a resolving power of $R \sim 44{,}000$. The TRES spectra were extracted as described in Buchhave et al. (2010), and a multi-order relative velocity analysis was performed for TOI 262 and TOI 444 by cross-correlating the strongest observed spectrum as a template, order by order, against the remaining spectra, for each target. We used methods designed for M dwarf stars (TRES41; Irwin et al. 2018) to derive the rotational velocities for TOI 198 and TOI 244. TRES41 uses the wavelength range 707–717 nm, which is dominated by Titanium(II) Oxide, to cross-correlate an observed spectrum against Barnards star to estimate the rotational velocity of the star. Stellar parameters were derived for TOI 444, TOI 470, and TOI 518 using the Stellar Parameter Classification (SPC; Buchhave et al. 2012) tool. SPC cross-correlates an observed spectrum against a grid of synthetic spectra based on Kurucz atmospheric models (Kurucz 1992) to derive effective temperature, surface gravity, metallicity, and rotational velocity of the star.

Reconnaissance spectra for each of the systems we validate were also obtained with the CHIRON fiber-fed cross-dispersed echelle spectrometer (Tokovinin et al. 2013) at the Cerro Tololo Inter-American Observatory (CTIO)/Small and Moderate Aperture Research Telescope System (SMARTS) 1.5 m telescope. CHIRON has a spectral resolving power of $R = 80{,}000$ over the wavelength range of 410,870 nm. Spectra from CHIRON were reduced as per Paredes et al. (2021). The radial velocities were measured following the procedure from Zhou et al. (2020) via a least-squares deconvolution of each observation against a synthetic nonrotating template generated from the ATLAS9 model atmospheres (Castelli & Kurucz 2003).

2.3.3. High-contrast Imaging with Gemini Zorro/'Alopeke, Keck2-NIRC2, Palomar-PHARO, and SOAR-HRCam

In an effort to measure the impact of possible contamination from nearby stars and rule out the possibility of stellar companions, we obtained high-contrast imaging with multiple large, ground-based telescopes. Bound stellar companions, in addition to diluting transit signals and leading to the underestimation of planet radii (Ciardi et al. 2015), can create false-positive transit signals if they are eclipsing binaries (EBs).

We obtained high-contrast images from Gemini Zorro/'Alopeke (Scott et al. 2021), Keck2-NIRC2 (Wizinowich et al. 2000), Palomar-PHARO (Hayward et al. 2001), and SOAR-HRCam (Tokovinin 2018). Our Gemini observations are described in Table 5. These observations are more precisely described in Section 4.

2.3.4. Ground-based Photometry with LCOGT

The TESS pixel scale is $\sim 21''$ pixel^{-1}, and photometric apertures typically extend out to roughly $1'$, which generally results in multiple stars blending in the TESS aperture. We acquired ground-based time-series follow-up photometry of our planet candidates as part of the TESS Follow-up Observing Program Sub Group 1 (TFOP SG1; Collins 2019)[37] to attempt to detect the transit-like events on target and to rule out or identify nearby eclipsing binaries (NEBs) as the potential sources of the TESS detections.

We observed full predicted transit windows of TOI 198.01, TOI 244.01, TOI 444.01, and TOI 470.01 using the Las Cumbres Observatory Global Telescope (LCOGT; Brown et al. 2013) 1.0 m network. We observed TOI 198.01 on UT 2022 September 14 and TOI 244.01 on UT 2019 August 1 from the South Africa Astronomical Observatory (SAAO) node in Pan-STARRS z-short (zs) band. We observed TOI 444.01 on UT 2020 October 31 from the Siding Spring Observatory node in zs-band, and TOI 470.01 on UT 2021 October 23 from the Cerro Tololo Inter-American Observatory (CTIO) node in both Sloan g' and zs bands. We used the `TESS Transit Finder`, which is a customized version of the `Tapir` software package (Jensen 2013), to schedule our transit observations. The 1 m telescopes are equipped with 4096×4096 SINISTRO cameras having an image scale of $0.''389$ per pixel, resulting in a $26' \times 26'$ field of view. The images were calibrated by the standard LCOGT `BANZAI` pipeline (McCully et al. 2018). Differential photometric data were extracted with `AstroImageJ` (Collins et al. 2017) using target star circular photometric apertures, which exclude all flux from the nearest known Gaia DR3 stars that are bright enough to be capable of causing the TESS detection. Transit-like events that are consistent with the depths, durations, and ephemerides measured by TESS were detected in the follow-up apertures, confirming that the TOI 198.01, TOI 244.01, TOI 444.01, and TOI 470.01 signals occur on-target relative to known Gaia DR3 stars. These observations are further discussed in Section 4.

3. Stellar Properties

3.1. Published System Parameters

Some of these planets have been published in previous works. We give stellar parameters as computed by these authors in Table 3. Given that these are parameters for systems that are already well characterized, we do not perform any further stellar analysis, and use these parameters to calculate planet properties later. We include the reference from which these parameters were taken for each star at the bottom of the tables.

3.2. SED Analysis of New Systems

As an independent determination of the basic stellar parameters for previously unpublished systems, we performed an analysis of the broadband spectral energy distribution (SED) of each star together with the Gaia EDR3 parallax (with no systematic offset applied; see, e.g., Stassun & Torres 2021). This was in order to determine an empirical measurement of the stellar radius, following the procedures described in Stassun & Torres (2016) and Stassun et al. (2017, 2018). Depending on the photometry available for each source, we pulled the B_T and V_T magnitudes from *Tycho-2* (Gaia Collaboration 2020); the *BV* g, r, and i magnitudes from *APASS* (Al 2020); the JHK_S magnitudes from the Two Micron All Sky Survey (2MASS; Skrutskie et al. 2003); the W1–W4 magnitudes from the Wide-field Infrared Survey Explorer (WISE); the G, $G_{\rm BP}$, and $G_{\rm RP}$ magnitudes from Gaia (Gaia Collaboration 2018); and the far-ultraviolet (FUV) and/or near-ultraviolet (NUV) fluxes from the Galaxy Evolution Explorer (GALEX; Sandstrom 2019). Together, the available photometry generally spans the stellar

[37] https://tess.mit.edu/followup (NExScI 2022).

Table 3
Stellar Parameters for Previously Published Targets, TOI 118, TOI 262, TOI 455, TOI 560, and TOI 562

Parameter	Unit	TOI 118	TOI 262	TOI 455	TOI 560	TOI 562
G mag.	mag	9.650	8.678	10.058	9.270	9.880
TESS mag.	mag	9.179	8.134	8.840	8.592	8.741
Spect. type		G5V	K0V	M3.0	K4V	M2.5V
$T_{\rm eff}$	K	5527 ± 65	5310 ± 124	3340 ± 150	4511 ± 110	3505 ± 51
[Fe/H]	dex	0.04 ± 0.04	$+0.26 \pm 0.07$	-0.34 ± 0.09	0.00 ± 0.09	-0.12 ± 0.16
$\log(g)$		4.40 ± 0.11	4.54 ± 0.28		4.62 ± 0.12	4.94 ± 0.07
$R_\star$	$R_\odot$	1.03 ± 0.03	0.853 ± 0.021	0.265 ± 0.011	0.65 ± 0.02	0.337 ± 0.015
$M_\star$	$M_\odot$	0.92 ± 0.03	0.913 ± 0.029	0.257 ± 0.014	0.73 ± 0.02	0.342 ± 0.011
$\log(R'_{\rm HK})$		-5.07 ± 0.03	-5.18 ± 0.06		-4.47 ± 0.02	-5.37
$P_{\rm rot}$	days		67 ± 1		12.2 ± 0.2	77.8 ± 2.1
Age	Gyr	10.0 ± 2.0	$\geqslant 0.8$		0.48 ± 0.19	
Source		Esposito et al. (2019)		Winters et al. (2022)	Barragán et al. (2022)	Luque et al. (2019)

Table 4
Derived Stellar Parameters for the TOIs We Validate from SED Analysis

Parameter	Unit	Source	TOI 198	TOI 244	TOI 444	TOI 470	TOI 518
G mag	mag	Gaia DR2	10.915	11.549	9.612	11.245	10.564
TESS mag	mag	TIC	9.928	10.347	9.056	10.700	10.143
Spect. type		SIMBAD	M0V	M2	K1/2V	late G	early G
Av	mag		0.0	0.0	0.12 ± 0.02	0.07 ± 0.03	0.05 ± 0.05
$T_{\rm eff}$	K	SED	3650 ± 75	3450 ± 75	5225 ± 70	5190 ± 90	5845 ± 70
		TIC	3782 ± 157	3407 ± 157	5091 ± 124	5112 ± 125	5891 ± 122
[Fe/H]	dex	SED/TRES	-0.7 ± 0.5	0.0 ± 0.3	0.08 ± 0.08	0.10 ± 0.08	0.00 ± 0.08
$\log(g)$	cgs	SED/TRES	4.75 ± 0.25	4.75 ± 0.25	4.64 ± 0.10	4.54 ± 0.10	4.46 ± 0.10
		TIC	4.783 ± 0.005	4.820 ± 0.004	4.567 ± 0.082	4.524 ± 0.086	4.714 ± 0.101
$F_{\rm bol}$	erg s^{-1} cm^{-2} $\times 10^{-9}$	SED	1.765 ± 0.041	1.336 ± 0.047	3.895 ± 0.014	0.830 ± 0.001	1.44 ± 0.051
$R_{\rm star}$	$R_\odot$	SED	0.441 ± 0.019	0.399 ± 0.019	0.779 ± 0.053	0.831 ± 0.053	1.027 ± 0.025
$M_{\rm star}$	$M_\odot$	SED	0.467 ± 0.023	0.424 ± 0.021	0.96 ± 0.13	0.87 ± 0.09	1.07 ± 0.06
$\log(R'_{\rm HK})$			-5.05 ± 0.08		-4.46 ± 0.05		-4.76 ± 0.05
$P_{\rm rot}$	days	pred, $R'_{\rm HK}$	45.4 ± 5.3		13.0 ± 3.0	18.28 ± 3.99	15.9 ± 1.6
Age	Gyr	pred,$P_{\rm rot}$	5.3 ± 1.0		0.57 ± 0.14	1.4 ± 0.6	2.7 ± 0.6

Note. We compare some parameters, including $T_{\rm eff}$ and $\log(g)$ to values from the TIC.

SED over the approximate wavelength range 0.2–22 μm (see Appendix C).

We performed fits to the photometry using Kurucz stellar atmosphere models, with the principal parameters being the effective temperature ($T_{\rm eff}$), metallicity ([Fe/H]), and surface gravity ($\log g$), for which we adopted the spectroscopically determined values when available. We included the extinction, A_V, as a free parameter but limited to the full line-of-sight value from the Galactic dust maps of Schlegel et al. (1998); for systems that have small distances according to Gaia, we fixed $A_V \equiv 0$. The resulting fits shown in Appendix C have a reduced χ^2 ranging from 0.7 to 1.6 (in some cases excluding the GALEX photometry, if a UV excess indicative of chromospheric activity is present; see below), and the best-fit parameters are summarized in Table 4.

Integrating the model SED gives the bolometric flux at Earth, $F_{\rm bol}$. Taking the $F_{\rm bol}$ together with the Gaia parallax directly gives the luminosity, $L_{\rm bol}$. Similarly, the $F_{\rm bol}$ together with the $T_{\rm eff}$ and the parallax gives the stellar radius, $R_\star$. Moreover, the stellar mass, $M_\star$, can be estimated from the empirical eclipsing-binary-based relations of Torres et al. (2010) or the M_K-based relationships of Mann et al. (2019) for the cooler stars, and the (projected) rotation period can be calculated from $R_\star$ together with the spectroscopically measured $v \sin i$. The mean stellar density, $\rho_\star$, follows from the mass and radius. When available, the GALEX photometry allows the activity index, $\log R'_{\rm HK}$, to be estimated from the empirical relations of Findeisen et al. (2011). All quantities are summarized in Table 4.

Where possible, we have also estimated the system ages from the $R'_{\rm HK}$ activity and/or the stellar rotation, using the activity-age and/or rotation-age empirical relations of Mamajek & Hillenbrand (2008), which are applicable for $T_{\rm eff} \lesssim 6500$ K, or the relations of Engle & Guinan (2018) quantities, which are also summarized in Table 4.

4. Validation of New TESS Planets

In this section, we vet and validate four new planets, which is the process of identifying potential sources of the transit signal and calculating the probability that the given signal is likely to be due to a planet transiting the host star in question. We vet and validate transit signals for the following planets: TOI 198 b, TOI 244 b, TOI 444 b, and TOI 470 b. Our observations of TOI 518.01 to date were not sufficient to validate it as a planet. We briefly discuss our observations of TOI 518 and the reasons it could not be validated in Section 4.5. Our validation process included analyzing our photometric observations of these targets with TESS and

CHEOPS, as well as follow-up observations with high-resolution imaging and reconnaissance spectroscopy, which serve multiple purposes. These follow-up observations may either reveal or rule out the possibility of nearby stellar-mass companions to the target star, provide stellar parameters for our target stars, or, if they are precise enough, reveal the mass of the orbiting companion, or limits on that value. As part of our statistical analysis of our photometric observations with TESS, we use the Bayesian statistical validation analysis code TRICERATOPS (Tool for Rating Interesting Candidate Exoplanets and Reliability Analysis of Transits Originating from Proximate Stars; paper: Giacalone et al. 2021; code: Giacalone & Dressing 2022). Among the sources of astrophysical false positives, TRICERATOPS calculates the probability that the transit-like signal is due to an eclipsing binary, including the probability that a planet exists but orbits either the primary or secondary component of the binary (PEB and SEB, respectively). This code also calculates the probability that the signal is the result of a foreground star or EB that dilutes or mimics the possible transit signature, or a background star or EB that may have the same effect. Finally, TRICERATOPS calculates the probability that the given signal is off target and due to a nearby star or EB.

For each of our validated targets, we show the star field around the target star with TESS pixels overlaid, as well as the SPOC report difference image centroid offset (as in Figure 3, Twicken et al. 2018; Li et al. 2019). For the star field, the yellow star in the center of the figure indicates the target star, and other dots represent other stars in the field according to their measured positions in Gaia DR2, scaled in color by their TESS magnitudes. Additionally, we include directional arrows pointing north and east. The gray dashed line represents an equidistant circle of radius 200″ from the target star in each star field image. In all cases our centroid offset plots show the in-transit centroid location from multiple sectors. The red asterisk denotes the location of the target, the pink cross denotes the 1σ centroid offset, and the blue circle represents the 3σ centroid offset. In each case except TOI 518 (for which we analyze only one TESS sector), the green crosses represent the centroid location for each sector.

Five TOIs were observed using the 'Alopeke and Zorro speckle instruments on the Gemini North/South 8 m telescopes (Scott et al. 2021; Howell & Furlan 2022). Both speckle instruments provide simultaneous speckle imaging in two bands (562 and 832 nm) with output data products that include reconstructed images and robust contrast limits on companion detections. A number of different sets of speckle observations were obtained for each star and processed in our standard reduction pipeline (see Howell et al. 2011). Figure 1 shows our final 5σ contrast curves and the 832 nm reconstructed speckle image, and the details of our observations are shown in Table 5. These contrast curves are also used by TRICERATOPS to aid in our statistical vetting.

In addition to light-curve photometry, we employ high-resolution imaging, which is part of the standard process for validating transiting exoplanets to assess the possible contamination of bound or unbound companions on the derived planetary radii (Ciardi et al. 2015). Close stellar companions (bound or line of sight) can confound exoplanet discoveries in a number of ways. The detected transit signal might be a false positive due to a background eclipsing binary, and even real planet discoveries will yield incorrect stellar and exoplanet parameters if a close companion exists and is unaccounted for (Furlan & Howell 2020). Additionally, the presence of a close companion star may mask the detection of small planets (Lester et al. 2021). Given that nearly half of solar-like stars are in binary or multiple star systems (Matson et al. 2018), high-resolution imaging provides crucial information toward our understanding of exoplanetary formation, dynamics, and evolution (Howell et al. 2021a, 2021b).

We also use diagnostics from our CHEOPS photometry (which has a pixel scale of $\sim 1''$) to validate these planets. For example, we estimate the contributions of background flux in our CHEOPS light curves and analyze the centroid position of the flux both in transit and out of transit. Although we did not use the DRP light curves, DRP diagnostics are still useful. The CHEOPS DRP (Hoyer et al. 2020) uses field star properties derived from Gaia DR2 to simulate the brightnesses of nearby stars in CHEOPS light curves, where magnitudes are converted to CHEOPS magnitudes. Then, based on the relative position of the background stars in or near the chosen aperture and their brightnesses in the CHEOPS band, the DRP estimates the flux contribution from background stars in the light curve and reports this as a percentage for each frame. This contribution is then divided out from the light curve in each CHEOPS frame such that the light curve is de-biased from background sources. Therefore, noting potential sources of background contamination with CHEOPS's extremely high-precision photometry is useful for characterizing whether the transit signal is on target. We demonstrate an example of this in Figure 2.

Using TESS photometry and these high-resolution contrast curves, TRICERATOPS reports a false positive probability (FPP) and nearby FPP (NFPP) for each target. FPP represents the aggregate probability that the observed transit is due to something other than a transiting planet around the target star, and NFPP is the same except that it suggests the origin of the signal is a nearby known TICv8 star. In order for the planet candidate to be considered statistically validated, we require $\mathrm{FPP} < 0.015$ and $\mathrm{NFPP} < 10^{-3}$, as recommended by Giacalone et al. (2021). To account for intrinsic scatter in the statistical calculation, we ran 20 trials of calculating the FPP and NFPP, and report the mean and standard deviation of these values for each of our validated systems. Twenty trials allows us to explore the possibility that our result is not sensitive to intrinsic scatter in the calculation.

Further, we employ reconnaissance spectroscopic observations of our validated systems. We employed spectroscopic observations from both FLWO-TRES and SMARTS-CHIRON, whose observations of specific targets are delineated in the following subsections. We use spectroscopic observations in this paper for the purpose of ruling out a stellar-mass companion, with the exception of TOI 198 b, for which we have high-precision radial velocities from Very Large Telescope (VLT)-ESPRESSO and are thus able to place constraints on the planet mass.

In addition to the high-resolution imaging, we have utilized Gaia to identify any wide stellar companions that may be bound members of the system. Typically, these stars are already in the TESS Input Catalog and their flux dilution to the transit has already been accounted for in the transit fits and associated derived parameters. We searched for possible widely separated companions based upon similar parallaxes and proper motions (Mugrauer & Michel 2020, 2021). Additionally, the Gaia DR3 astrometry provides insight on the possibility of

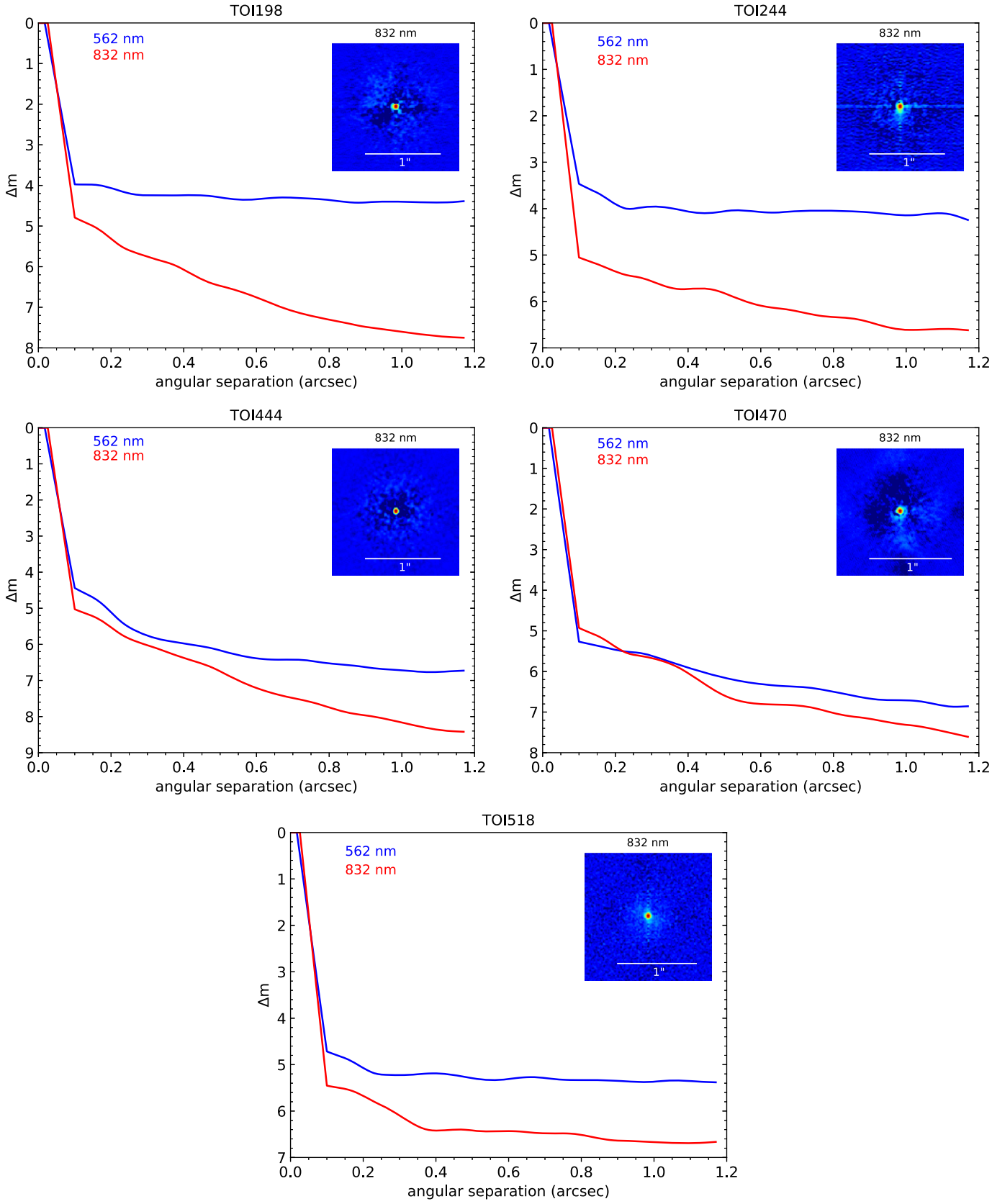

Figure 1. Contrast curves in 562 and 832 nm (blue and red, respectively) for TOI 198, TOI 244, TOI 444, TOI 470, and TOI 518 from Gemini observations with insets showing the central star at 832 nm.

Table 5
Our Speckle Observations with Gemini of the Five TOIs We Validate, Including Target Observed, Date of Observation, Distance to Star (in pc), whether a Luminous Companion Was Detected, the Achieved Contrast in Δmag, and the Inner and Outer Visibility Limits

TOI	TIC	UT Date	Dist (pc)	Companion?	Contrast (Δmag)	Inner (au)	Outer (au)
198	12421862	2020 Aug 4	23.7	N	5.0–8.0	0.5	28
244	118327550	2020 Aug 4	22	N	5–6.5	0.44	26
444	179034327	2020 Jan 9	57.4	N	5.0–8.0	1.15	69
470	37770169	2021 Feb 24	130.5	N	5–7.5	2.6	157
518	264979636	2021 Feb 9	159.8	N	5–6.8	3.2	192

inner companions that may have gone undetected by either Gaia or the high-resolution imaging. The Gaia Renormalized Unit Weight Error (RUWE) is a metric, similar to a reduced chi-square, where values that are $\lesssim$1.4 indicate that the Gaia astrometric solution is consistent with the star being single; RUWE values $\gtrsim$1.4 may indicate an astrometric excess noise, possibly caused by the presence of an unseen companion (Ziegler et al. 2020).

4.1. Validation of TOI 198 b

We analyzed two TESS sectors' worth of data for TOI 198, including one in the PM and one in EM1. Two transit events were initially identified by the SPOC pipeline (Jenkins 2002; Jenkins et al. 2010, 2020) at Barycenter-corrected TESS Julian Date (BTJD = BJD–2457000) 1356.3754 and 1376.8027 as a potential planet candidate with a 20.427 days period in 2018 October. Three transit events were identified by QLP, where the middle transit fell between the two previously identified signals at a time of BTJD = 1366.574 for a period of 10.218 days. The SPOC light curve was later reprocessed, during which the third transit event was identified at the same time as the QLP signal, but the significance of this signal was dubious. During the EM1 sector (S29), only one transit signal was identified, but due to the timing of the observation, it remained ambiguous whether the period of the signal was truly 10.2 days or 20.4 days. Further, our CHEOPS observation was scheduled at a time that also did not break the period alias. However, our LCOGT 1 m observation on UT 2022 September 14 detected the transit-like event on target relative to known Gaia DR3 stars and confirmed the 10.2 days alias as the true orbital period.

We further validated the transit signal by checking the centroid position for each TESS sector to assure that the signal was on target. Shown in the bottom of Figure 3, the centroid of the difference image agrees very well with the expected position of the target star, meaning the transit signal is indeed on target. We saw no discrepancies between the even- and odd-numbered transits, consistent with less than 1σ depth difference.

We obtained high-resolution-imaging observations of TOI 198 with the Gemini-'Alopeke imager on 2020 October 4th, which is shown in the top left panel Figure 1. The image has a pixel scale of 0.″01, with an estimated PSF size of 0.″02. We find that this star is single at least out to 1.″2, with no companion brighter than 5–8 mag below that of the target star beyond 0.″1.

We also obtained three epochs of reconnaissance spectra for TOI 198 with SMARTS-CHIRON. While TOI 198's low temperature (see Table 4) renders it unreliable for spectroscopic classification with this telescope, we were able to deduce from these RVs that the lines are narrow, which is indicative of a single, slowly rotating star. Additionally, we see no large RV variation between our epochs, as shown in Table 6.

Further, we obtained 23 high-precision radial velocity epochs of TOI 198 with the VLT-ESPRESSO (Pepe et al. 2021) instrument between 2019 July 4th and 2019 September 12th, shown in Figure 4 and in Table 7. With these observations, we were able to not only rule out the presence of a stellar-mass companion to TOI 198, but also constrain the mass of TOI 198 b. The radial velocity time series were modeled with a Keplerian model using `Radvel`[38] (Fulton et al. 2018). Our independent analysis of transit data allowed us to use informative priors on the orbital period and time of central transit. We fixed a circular orbit ($e = 0$) and added a radial velocity jitter term. `Radvel` performs a Markov Chain Monte Carlo (MCMC) technique to obtain the credible intervals of the parameters. We obtained a semi-amplitude of $K_b = 2.04^{+0.55}_{-0.56}$ [m s^{-1}], equivalent to a planetary minimum mass of 4.0 ± 1.1 $M_\oplus$.

Finally, our assessment of this star with Gaia showed that based upon similar parallaxes and proper motions, there are no additional widely separated companions identified by Gaia. TOI 198 has a Gaia EDR3 RUWE value of 1.09, indicating that the astrometric fits are consistent with the single star model.

Our statistical vetting with `TRICERATOPS` supports the conclusion that the transit signals are from a transiting planet that orbits the target star, with FPP = 0.0142 ± 0.0016 and NFPP = 0.00023 ± 0.00005.

Given the information at hand, we are able to conclude that TOI 198 is a star that has no massive companions, and that the transit signal we see is likely due to a transiting planet. Thus, we consider TOI 198 b to be validated.

4.2. Validation of TOI 244 b

We analyzed two TESS sectors' worth of data for TOI 244, including one in the PM and one in EM1. Four transit events were identified in each of the sectors by the SPOC pipeline at BTJD = 1357.3647 with a period of 7.39719 days. As shown by the top panel of Figure 5, the field around TOI 244 is relatively uncrowded, and there are no stars brighter than $\Delta\text{mag} \approx 7.5$ in the TESS band closer than 110″, or approximately five TESS pixels away. This would indicate that there are no meaningful contributions from nearby stars in the aperture for this target. Our two visits to TOI 244 with CHEOPS also exhibit extremely low levels of flux contributions from nearby stars. The DRP simulated images of nearby stars in both of our CHEOPS visits, which occurred in 2021 October. The light curves of simulated stars near TOI 244 exhibit average contributions of 6.89×10^{-4}% and 6.74×10^{-4}% for our first and second visits, respectively.

[38] https://radvel.readthedocs.io/en/latest/

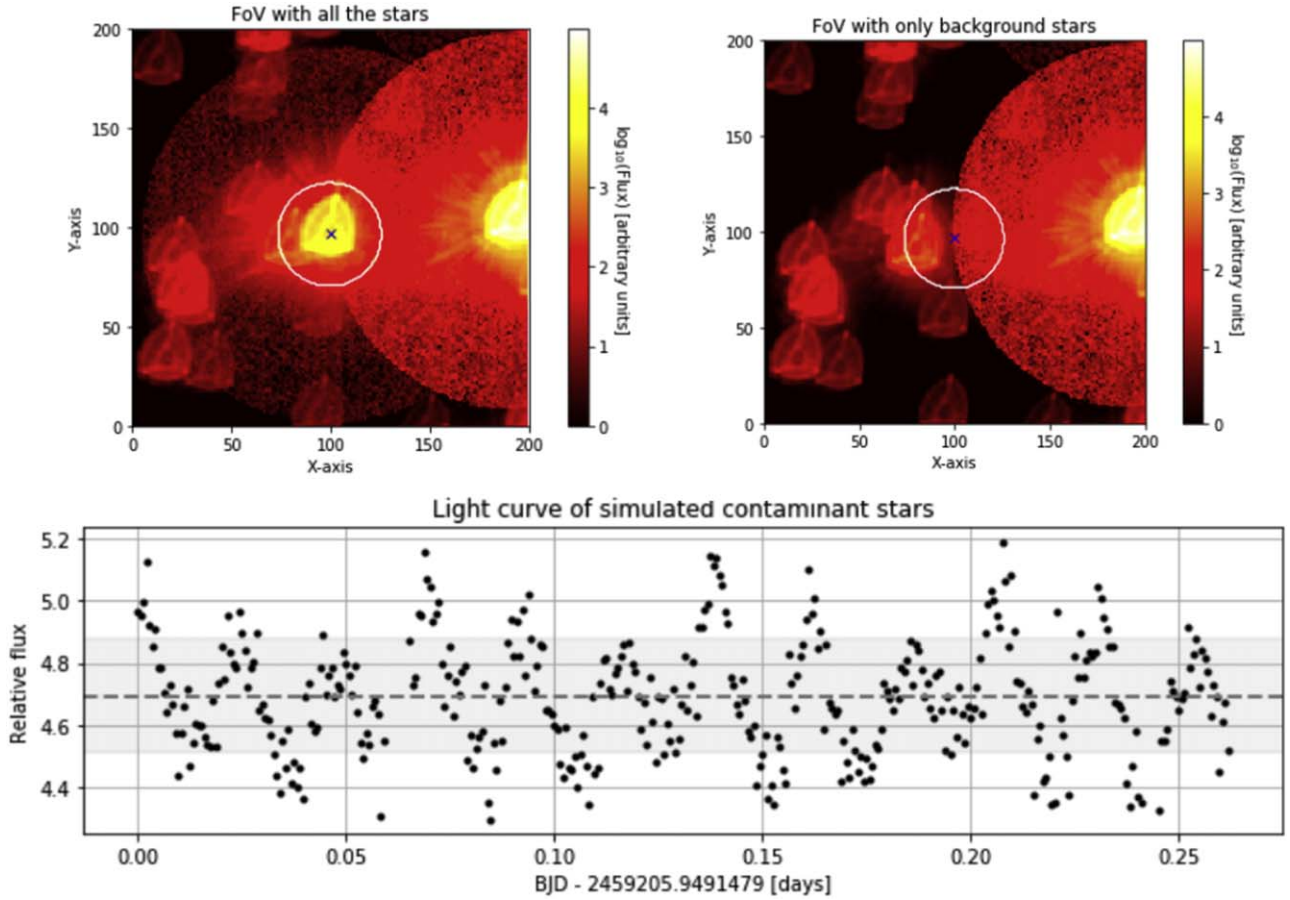

Figure 2. Diagnostics of contamination from nearby stars in the CHEOPS light curve for TOI 470. Top left: CHEOPS field of view, including both our target star (centered on black "X") and field stars. Top right: DRP simulated image of only field stars without a target star, exhibiting relative fluxes of nontarget stars. Note the difference in color scales between field stars with and without a target star. Bottom: simulated contributions to the CHEOPS light curve from field stars, which is subtracted from the light curve. The average contribution from off-axis stars is 4.7% for this light curve.

Further, we confirm that the transit signals we see are on the target star. Our centroid difference image of in-transit and out-of-transit flux (bottom panel Figure 5) shows that while there is some offset in the position of the centroid position of in-transit flux during sector two from its expected position, the centroid position is overall consistent with being in the expected position. The centroid position of in-transit flux does not appear to move strictly toward any other star. Further, for either of our CHEOPS observations, there is no centroid offset from its central position larger than 2 pix, which means the transit signal is indeed on target. Using `TRICERATOPS`, we find an NFPP consistent with zero.

TOI 244 was observed by LCOGT on UT 2019 September 30 using a $5\farcs8$ target aperture that excludes flux from the nearest known Gaia DR3 stars and detected a 1 ppt transit-like event on target.

We obtained high-resolution speckle images of this star with the 8.0 m Gemini telescope equipped with the 'Alopeke instrument at central wavelengths of 832 and 562 nm. Our images had a pixel scale of $0\farcs01$ pixel^{-1}, with an estimated PSF of $0\farcs02$. We obtained an estimated contrast of $\Delta\mathrm{mag} = 5.98$ at $0\farcs5$ in the 832 nm band, as shown in Figure 1 (top right). A $\sim$1000 ppm event could be caused by a star as dim as $\Delta\mathrm{mag} \sim 7.5$. Given that the only two stars brighter than $\Delta\mathrm{mag}$ 7.5 are at a distance from the target so as not to cause significant contamination, we believe they only marginally contaminate the TESS aperture. This indicates that TOI 244 is a single star.

Similar to TOI 198, we were unable to reliably use our follow-up reconnaissance spectra of TOI 244 with SMARTS-CHIRON to classify the star. While our phase coverage was poor, narrow spectroscopic lines indicate that this star is single and slowly rotating. Our two epochs are unable to independently rule out a stellar-mass companion at the ephemeris of the transiting candidate, but our high-contrast speckle imaging showed no indication of a luminous companion. Therefore, between these two pieces of evidence, we are able to rule out a stellar companion. Further, given that our RVs span nearly 400 days, we are able to rule out any massive companion at a wider orbit.

Finally, our assessment of this star with Gaia showed that based upon similar parallaxes and proper motions, there are no additional widely separated companions identified by Gaia. TOI 244 has a Gaia EDR3 RUWE value of 1.25, indicating that the astrometric fits are consistent with the single star model.

Our statistical vetting with `TRICERATOPS` supports the conclusion that the transit signals we see are due to a planet orbiting the target star, as we report $\mathrm{FPP} = (1.203 \pm 0.814) \times 10^{-5}$. For the above reasons, we consider the planetary nature of the transit signals around TOI 244 to be validated.

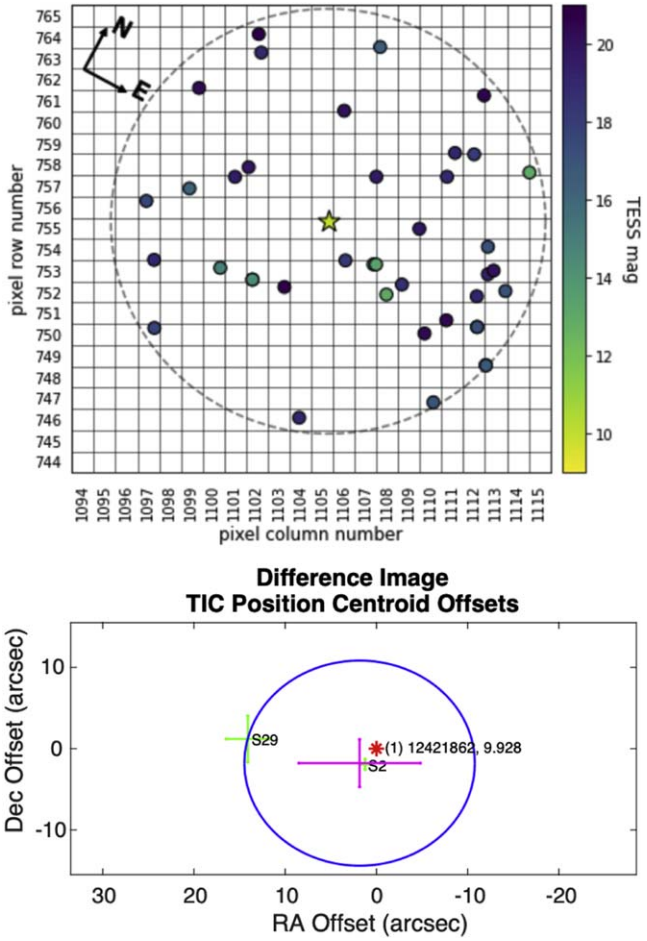

Figure 3. Top: field stars near TOI 198 (TIC 12421862; indicated as a yellow star) with TESS pixels overlaid. TOI 198 resides in a relatively uncrowded portion of the sky, and there are no stars brighter than Δmag $\approx$ 3.3 in the TESS band closer than 60″, or approximately 3 TESS pixels away. Bottom: centroid difference image between in-transit flux and out-of-transit flux from TESS observations of TOI 198.

4.3. Validation of TOI 444 b

We analyzed four TESS sectors' worth of data for TOI 444, including two each in the PM and EM1. We examined difference images from all four sectors (bottom panel of Figure 6), where the centroid position in the difference image is shown by a green cross. Although the sector four centroid position approaches the 3σ circle, we see no significant evidence of centroid offset for this target, indicating that the transit signal is on target. Another potential indicator of a false positive is a difference in the parameters of even-numbered transits in the light curve and odd-numbered transits, which may indicate that they are primary and secondary eclipses of an EB. However, the SPOC report for this TOI showed no statistically significant difference between even and odd transits.

The CHEOPS DRP estimated that contamination from background stars accounted for only 0.1% of the flux in the OPTIMAL aperture, meaning that the signal is very likely uncontaminated. We also checked the centroid location in each CHEOPS image to ensure that the in-transit and out-of-transit flux were on target. The centroid shifted at most 1.0 pixels from the mean in both the X and Y directions, indicating that the CHEOPS light curve and transit were on target.

Table 6
SMARTS-CHIRON RVs for the TOIs We Validate

BJD_UTC	vrad	svrad
TOI 198		
2458650.88886	20.551	0.085
2458653.90559	20.477	0.165
2459200.60414	20.387	0.068
TOI 244		
2458824.62649	15.254	0.219
2459209.62434	15.205	0.179
TOI 444		
2458531.59407	1.106	0.029
2459218.64491	1.130	0.027
2459454.85929	1.095	0.024
TOI 470		
2458545.63013	30.296	0.044
2459349.44464	30.390	0.022
TOI 518		
2458570.58672	45.460	0.039
2458626.45015	45.507	0.029

Note. The implications of these RVs are delineated in the respective subsection for each validated planet.

As a further check that the transit signal was on target, TOI 444 was observed by LCOGT on UT 2020 October 31 using a follow-up aperture that excludes all flux from the nearest Gaia DR3 neighbors and detected a 1.4 ppt transit-like event on target.

We performed reconnaissance spectroscopy to determine whether the star had an unresolved massive companion, shown in Table 8. A radial velocity on the order of km s^{-1} would indicate the presence of such a companion, but observations of this star with both FLWO-TRES and the CHIRON spectrometer at SMARTS showed that it is a single G dwarf. Further, the star observed by multiple high-resolution imagers, including the Zorro and 'Alopeke imagers at Gemini North, HRCam at the Southern Astrophysical Research (SOAR) Telescope in Chile, and NaCo at the VLT in Chile. For simplicity, we show only the Gemini contrast curve, but all images of this star indicated that it had no close companion at Δmag < 5 at 0.″1 of separation.

Finally, our assessment of this star with Gaia showed that based upon similar parallaxes and proper motions, there are no additional widely separated companions identified by Gaia. TOI 444 has a Gaia EDR3 RUWE value of 1.13, indicating that the astrometric fits are consistent with the single star model.

We applied the `TRICERATOPS` statistical vetting. `TRICERATOPS` returned FPP $= (3.26 \pm 6.68) \times 10^{-6}$ and NFPP $= (1.44 \pm 0.95) \times 10^{-16}$ for TOI 444 b, and a visual inspection of the stellar field showed no bright stars in or near the TESS aperture for this light curve.

4.4. Validation of TOI 470 b

TOI 470 was observed in sector six of the TESS PM and sector 33 of the EM1. Figure 7 shows the field around TOI 470 (top) and the SPOC centroid image (bottom). The top panel is

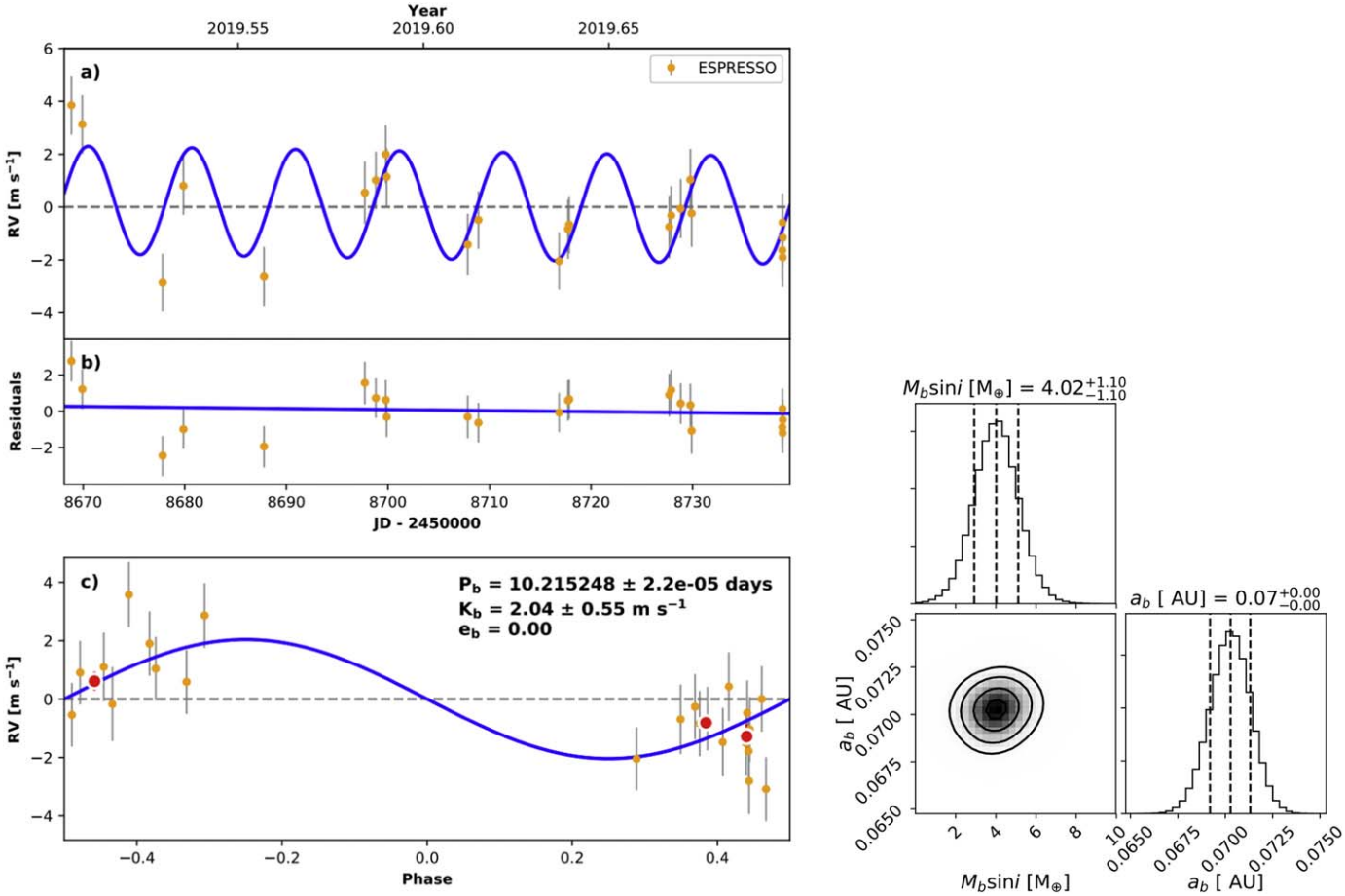

Figure 4. Left: (a) best-fit one-planet Keplerian orbital model for TOI 198. The maximum likelihood model is plotted. The thin blue line is the best-fit one-planet model. We add in quadrature the RV jitter term(s) listed in Table 2 with the measurement uncertainties for all RVs. (b) Residuals to the best-fit one-planet model. (c) RVs phase-folded to the ephemeris of planet b. The small point colors and symbols are the same as in panel (a). Right: corner plot showing posterior distribution for TOI 198 b mass.

Table 7
ESPRESSO Radial Velocities for TOI 198

Time (JD)	RV (m s^{-1})	RV Uncert. (m s^{-1})
2458668.84736	20278.25	0.41
2458669.91176	20277.53	0.39
2458677.81612	20271.54	0.36
2458679.87403	20275.20	0.35
2458687.79316	20271.76	0.46
2458697.72404	20274.94	0.56
2458698.80579	20275.41	0.35
2458699.78268	20276.40	0.37
2458699.86914	20275.54	0.35
2458707.85215	20272.98	0.55
2458708.90561	20273.91	0.34
2458716.85516	20272.36	0.30
2458717.74245	20273.56	0.42
2458717.85335	20273.73	0.33
2458727.69072	20273.65	0.58
2458727.89349	20274.08	0.42
2458728.83222	20274.34	0.43
2458729.78372	20275.43	0.56
2458729.90453	20274.16	0.73
2458738.82735	20272.77	0.42
2458738.84339	20273.81	0.39
2458738.86206	20272.50	0.42
2458738.87890	20273.24	0.41

color-coded by TESS magnitude, and TOI 470 is shown as a star. Although the field appears to be crowded, there are no stars brighter than 14th magnitude within 80″ of the target star, which contribute little to the light curve. Additionally, there are two bright stars relatively nearby: TIC 37770142, to the north-northwest, and TIC 37794435 (T mag = 9.05 and 8.37, respectively). These stars are too far from TOI 470 to contribute significantly to the light curve. This is evident from the centroid image, which is a data product of the SPOC pipeline. The centroid position is consistent in the difference image, and the target is within the 1σ area, suggesting that the transit signal is on target. Further, we saw no statistically significant difference between the depths of even- and odd-numbered transits, indicating that these are likely transit events and not primary and secondary eclipses of an EB.

Figure 2 shows the simulated CHEOPS DRP images, including background stars based on Gaia DR2 star maps, as well as the estimated contamination as a function of time in the CHEOPS light curve. Clearly, there are bright stars near the aperture, and in particular, TIC 37794435 is visible on the right sides of the top two panels in this figure. There is light from this star that bleeds into the aperture for our CHEOPS light curve, despite the fact that this is the smallest aperture we use to make a CHEOPS light curve, and is the main contributor of noise in this light curve. However, this noise contribution appears to be well characterized throughout the light curve, as

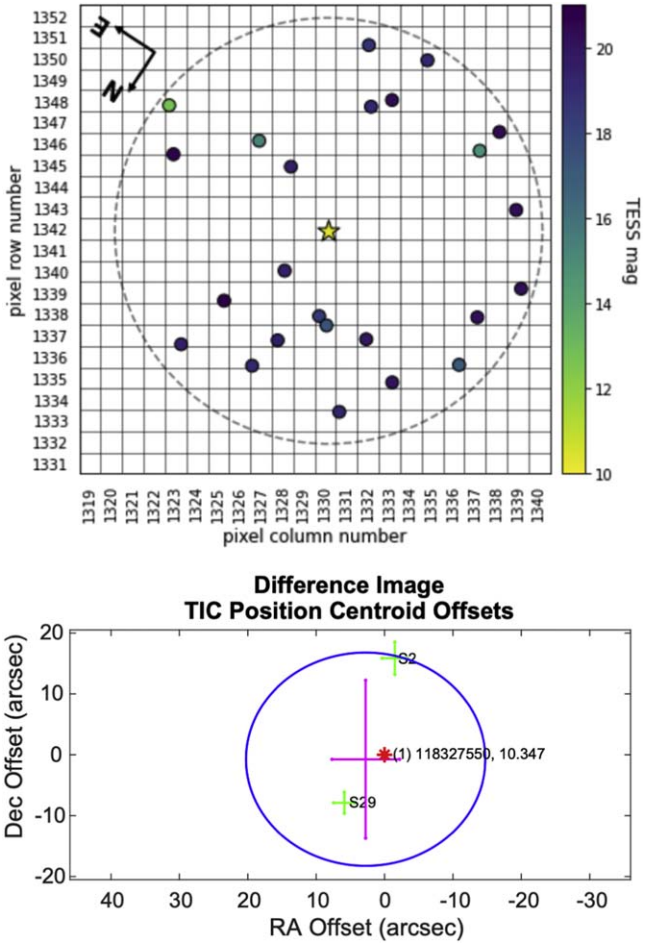

Figure 5. Top: field stars near TOI 244 (TIC 118327550; indicated as a yellow star) with TESS pixels overlaid. TOI 244 resides in a relatively uncrowded portion of the sky, and there are no stars brighter than Δmag $\approx$ 5.0 in the TESS band closer than 110″, or approximately five TESS pixels away. Bottom: centroid difference image between in-transit flux and out-of-transit flux from TESS observations of TOI 244.

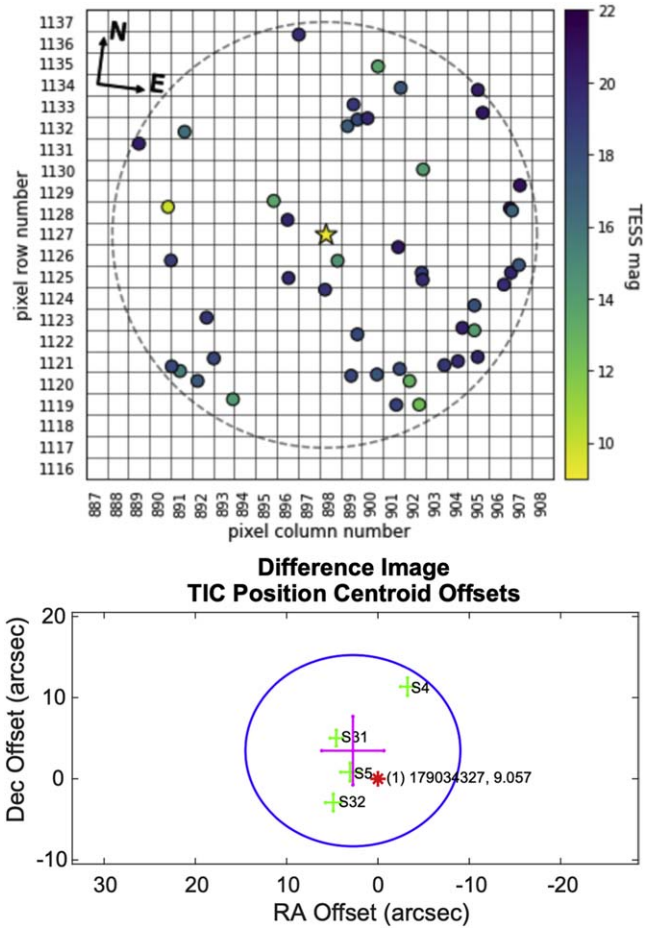

Figure 6. Top: field stars near TOI 444 (TIC 179034327; indicated as a star) with TESS pixels overlaid. The closest star to TOI 444, TIC 179034325, has a TESS magnitude of 14.4, and does not contribute significantly in the TESS bandpass. Bottom: centroid difference image between in-transit flux and out-of-transit flux from TESS observations of TOI 444.

the contamination level in the DEFAULT light curve remains relatively consistent around 4.7%, with an rms spread of 0.2%.

TOI 470 was observed by LCOGT on UT 2021 January 28 in both a blue (Sloan g') and red (zs) filter. Transit-like events with depths consistent with TESS were detected on target in both filters relative to known Gaia DR3 stars.

We checked the singularity of TOI 470 with both reconnaissance spectroscopy and high-resolution imaging. Low-resolution spectroscopy via the TRES instrument at FLWO and the CHIRON instrument at SMARTS, which tests whether the star has a high radial velocity, showed that the target star is indeed a single G dwarf. Our star was also observed via high-resolution speckle imaging with the Gemini Zorro instrument in both the 562 and 832 nm bands, as well as the SOAR-HRCam *I* band (centered at 879 nm). Additionally, the star was imaged with adaptive optics at Keck2 on the NIRC2 instrument in *K* band (centered at 2.196 μm). The Gemini and Keck2 images showed that TOI 470 is a single star to better than Δmag $>$ 6.16 mag at 0.″5, and the SOAR image showed that the star is single to an estimated contrast of Δ6.8 mag at 1.″0. For clarity, we show only the Gemini contrast curve in Figure 1 (middle right).

Finally, our assessment of this star with Gaia showed that based upon similar parallaxes and proper motions, there are no additional widely separated companions identified by Gaia. TOI 470 has a Gaia EDR3 RUWE value of 1.17, indicating that the astrometric fits are consistent with the single star model.

Our statistical vetting with `TRICERATOPS` supports the conclusion that the transit signals are from a transiting planet that orbits the target star, returning FPP $= 0.0034 \pm 0.0012$ and NFPP $= 0.0009 \pm 0.0003$ for TOI 470 b, just under the threshold for NFPP.

Table 8
Radial Velocities Collected with FLWO-TRES for TOI 444

Time (BJD)	RV (m s^{-1})	RV Uncert. (m s^{-1})	SNRe
2458516.685280	−34.50	33.86	33.8
2458528.614782	−66.17	33.86	26.0

4.5. Observations of TOI 518

TOI 518 was observed in sector seven of the TESS PM and sector 34 of the EM1. Photometric performance was nominal for sector seven, but there appeared to be stray light that corrupted the sector 34 light curve, rendering it untenable. Therefore, our TESS analysis of this target relies on only one sector. Figure 8 shows the field of stars around TOI 518 (top

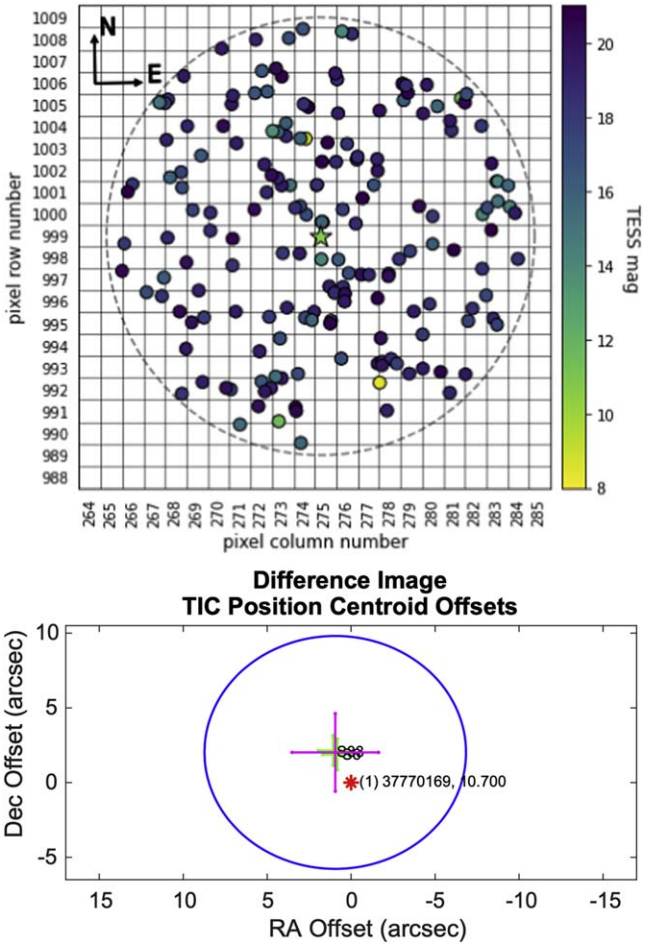

Figure 7. Top: field stars near TOI 470 (TIC 37770169; indicated as a star) with TESS pixels overlaid, and TESS magnitude is indicated by the color bar. Although the field appears crowded, there are no stars brighter than 14th magnitude closer than 80″, which is several TESS pixels away. The field star of note is to the north and west of TOI 470, which is also visible in the difference image. This star, TIC 37770142 (T mag = 9.05) is nearly 100″ away from TOI 470 and does not contribute significant flux in the aperture for our star. The other bright star in the field, TIC 37794435 (T mag = 8.37), is even farther away, at a separation of nearly 150″, and does not contribute any flux to the light curve. Bottom: centroid difference image between in-transit flux and out-of-transit flux from TESS observations of TOI 470.

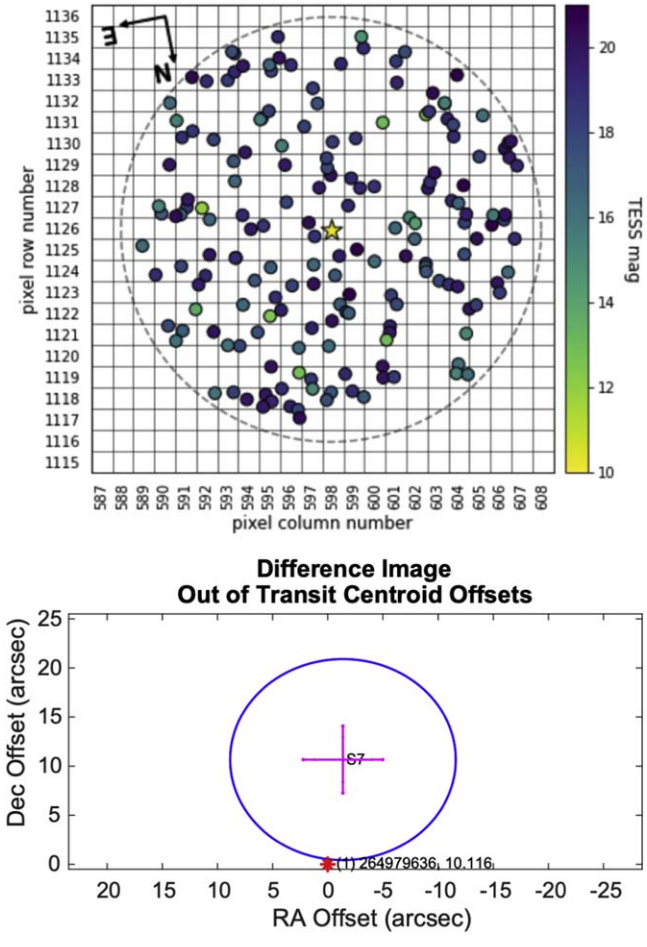

Figure 8. Top: field stars near TOI 518 (TIC 264979636; indicated as a star) with TESS pixels overlaid, and TESS magnitude is indicated by the color bar. Bottom: centroid difference image between in-transit flux and out-of-transit flux from TESS observations of TOI 518.

panel) and the centroid position (bottom panel). Although the field around our target appears to be relatively crowded, there are no stars brighter than 12th magnitude closer than 120″, which is several TESS pixels away. In the centroid position image, the centroid is south of TOI 518, representing a greater than 3σ centroid offset. It is thus questionable whether the transit signal is on target based on our TESS observations.

In both of our CHEOPS visits to this star, the contamination from nearby stars is very low, with a median contribution of 0.047% for the first visit in 2021 December and 0.056% for the second visit in 2022 March. The slight difference between these numbers is due to the relative sky motions of stars near our target as estimated by their proper motions from Gaia DR2. Centroid analysis of the CHEOPS photometry showed that the centroid position during the visit moved no more than 3″, indicating that the transit events seen by CHEOPS were indeed on target.

High-resolution-imaging observations from multiple large telescopes, including the 8 m Gemini North telescope, the 10 m Keck2 telescope, the Palomar 5 m telescope, and the SOAR 4.1 m telescope, indicated that the star is single. Keck2 and Palomar employed near-infrared (NIR) adaptive optics, whereas SOAR and Gemini employed optical speckle imaging, and all of these sensitivity curves are shown in Figures 1 (bottom row) and 9 (all panels). While the optical observations tend to provide higher resolution, the NIR AO tends to provide better sensitivity, especially to lower-mass stars. The combination of the observations in multiple filters enables better characterization for any companions that may be detected. Gaia DR3 is also used to provide additional constraints on the presence of undetected stellar companions, as well as wide companions.

The Palomar Observatory observations of TOI 518 were made with the PHARO instrument (Hayward et al. 2001) behind the natural guide star AO system P3K (Dekany et al. 2013) on 2019 April 18 in a standard five-point quincunx dither pattern with steps of 5″ in the narrow-band Br-γ filter ($\lambda_o = 2.1686$; $\Delta\lambda = 0.0326$ μm).

The Keck Observatory observations were made with the NIRC2 instrument on Keck II behind the natural guide star AO system (Wizinowich et al. 2000) on 2019 March 25 UT in the standard three-point dither pattern that is used with NIRC2 to avoid the left lower quadrant of the detector, which is typically noisier than the other three quadrants.

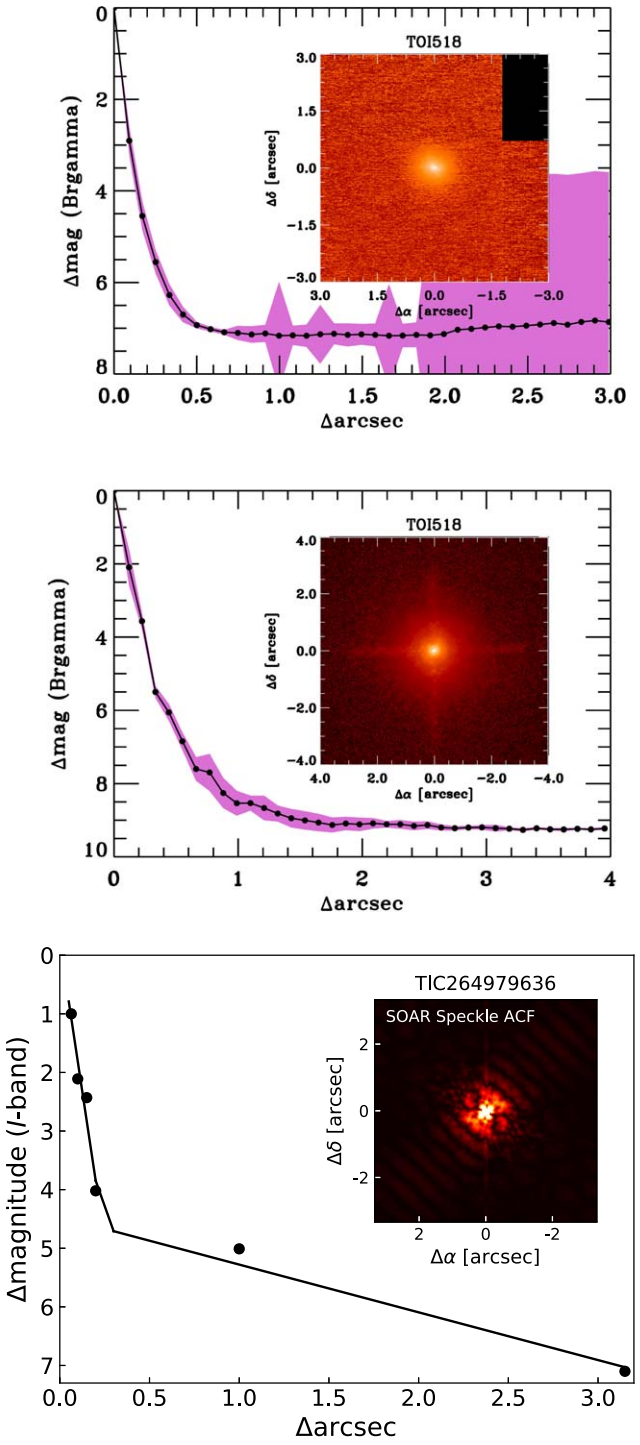

Figure 9. More contrast curves for TOI 518 (TIC 264979636), indicating that this star is single and not a blended EB. Top: Keck2 10 m AO sensitivity curve and image inlet. Middle: Palomar 5 m AO sensitivity curve and image inlet. Bottom: SOAR speckle sensitivity curve and image inlet.

The sensitivities of the final combined AO image were determined by injecting simulated sources azimuthally around the primary target every 20° at separations of integer multiples of the central source's FWHM (Furlan et al. 2017). The brightness of each injected source was scaled until standard aperture photometry detected it with 5σ significance. The resulting brightness of the injected sources relative to TOI 518 set the contrast limits at that injection location. The final 5σ limit at each separation was determined from the average of all of the determined limits at that separation, and the uncertainty on the limit was set by the rms dispersion of the azimuthal slices at a given radial distance. The final sensitivity curves for the Palomar and Keck data are shown in Figure 9; no additional stellar companions were detected in agreement with observations from SOAR and Gemini.

We searched for stellar companions to TOI 518 with speckle imaging on the 4.1 m SOAR telescope (Tokovinin 2018) on 2019 December 12 UT, observing in Cousins *I* band, a similar visible bandpass as TESS. As shown in Figure 9, this observation was sensitive to a 5.8 mag fainter star at an angular distance of 1″ from the target. More details of the observations within the SOAR TESS survey are available in Ziegler et al. (2020). The 5σ detection sensitivity and speckle autocorrelation functions from the observations are shown in Figure 9. No nearby stars were detected within 3″ of TOI 518 in the SOAR observations.

Finally, our assessment of this star with Gaia showed that based upon similar parallaxes and proper motions, there are no additional widely separated companions identified by Gaia. TOI 518 has a Gaia EDR3 RUWE value of 1.02, indicating that the astrometric fits are consistent with the single star model.

Our statistical vetting with `TRICERATOPS` supported the conclusion that these transit events are not likely to be from a nearby source, with NFPP $= 0.0004 \pm 0.00004$ in 20 trials for TOI 518.01. However, initial inspection of the two transits in the TESS light curve shows that they are shallow and slightly V-shaped. In some cases, this could indicate an EB with grazing eclipses, but at the very least this makes the radius of the transiting object uncertain, given a large uncertainty in the impact parameter, which is the projected distance between the midline of the stellar disk and the planet. As such, `TRICERATOPS` returned FPP $= 0.1555 \pm 0.2062$, which indicates that there is a significant chance that this signal may be an astrophysical false positive and warrants closer inspection.

According to our statistical analysis, potential false-positive scenarios—from highest to lowest probability—include the following: (1) a planet orbiting the target star at the given period but diluted by an unresolved foreground or background star (known as DTP), (2) an eclipse caused by an unresolved stellar companion with twice the period of the reported period (denoted SEBx2P), or (3) a planet orbiting the primary star of an unresolved stellar binary (PTP). These are scenarios that cannot easily be accounted for with high-contrast imaging alone.

Reconnaissance RVs may help account for these false-positive scenarios by constraining the mass of a potential massive companion. However, our reconnaissance RVs with FLWO-TRES and SMARTS-CHIRON were not taken at quadrature with respect to the estimated orbital period (∼17.87 days), meaning we could not reliably constrain the presence of any massive companion. Further characterization with radial velocities could confirm this system as having no massive companion.

For all of the above reasons, we cannot consider the transit events around TOI 518 validated. Therefore, moving forward we treat this planet candidate cautiously, with the understanding that this transit signal has not yet been statistically validated as a planet, although it is close. Thus, we refer to this signal as TOI 518.01.

5. Methodology: Photometric Modeling, Fitting, and Comparisons

In an effort to reduce the effects of systematics, we applied three independent methods to model and fit physical transiting planet parameters to our photometric data. Prior to fitting transit models to these light curves, we detrended these observations from various sources of both instrumental and astrophysical noise. Detrending, modeling, and fitting are discussed in the following section.

5.1. Obtaining and Detrending TESS Light Curves

As previously mentioned, we chose to analyze SPOC PDCSAP light curves from TESS observations of these systems. To extract light curves, Simple Aperture Photometry (SAP) is applied to pixel data, which is simply summing the pixel values within a predefined aperture as a function of time. The SPOC pipeline applies various calibrations and corrections. Calibrations include standard CCD reduction (bias, dark, and flat-field calibrations), smear corrections due to lack of camera shutters, and removal of cosmic ray signals (20 s cadence only). Background flux is estimated and removed per pixel and cadence; scattered light primarily from the Earth and Moon is identified and flagged for each light curve and cadence. Systematic errors due to spacecraft pointing and focus changes are encapsulated in cotrending basis vectors (CBVs), which are available for download from MAST. PDCSAP (Smith et al. 2012; Stumpe et al. 2012, 2014) light curves are obtained by cotrending SAP light curves against the CBVs. PDCSAP light curves are also corrected for finite photometric aperture and for crowding within the aperture. We downloaded SPOC PDCSAP light curves using `lightkurve`, a Python package for time-series data analysis. We stitched PDCSAP light curves from different TESS sectors together to yield one light-curve object, containing time in BTJD, normalized flux, and normalized flux error for each entry. We also removed nonnumeric entries.

SPOC PDCSAP light curves are already corrected for instrumental noise, but they may contain stellar or other astrophysical sources of noise. To account for this, we removed long-term stellar variability using `wotan`, which applies a sliding biweight filter to flatten the light curve (Hippke et al. 2019). In many instances, detrending with `wotan` did not significantly change the shape of the light curve. However, there were some obvious trends of stellar variability in our TESS light curves for TOIs 444, 455, and 560 that we eliminated with this detrending. Because our results are sensitive to transit depth, we did not want to overcorrect the light curves, and thus applied only minimal detrending. We did not apply regressions, splines, or Gaussian processes (GPs) to our light curves. Our TESS light curves are shown in Figure 18.

5.2. Detrending CHEOPS Light Curves

As described in Section 2.2, we extracted PSF photometry with `PIPE` to generate our CHEOPS light curves from imagettes. Then, we detrended our CHEOPS light curves using `pycheops`, which is a Python library developed for easy and efficient use with CHEOPS data products (Maxted et al. 2022). We used `pycheops` routines to trim outliers, decorrelate the light curves from systematic effects, and fit transit models. Photometric model fitting is described in the following section.

We began by trimming outliers from the light curves, which were those points that were 5σ away from the median value. Given that CHEOPS rolls about its optical axis as it observes, the shape of the PSF changes throughout an observation. Telescope roll angle with respect to a reference CCD position is reported. As such, we detrended against multiple parameters, including (X, Y) pixel position and telescope roll angle, as first-, second-, and third-order sine and cosine functions. We also detrended CHEOPS observations against background flux dominated by zodiacal light or scattered light from Earth, observation time, and stellar contamination in the aperture. Finally, we checked nearby solar system objects in order to account for glint from these objects. To avoid overfitting, we introduced each of these detrending parameters independently of one another and calculated the Bayes factor with and without the parameter, as in Trotta (2007). This allowed us to determine whether each parameter was necessary for the model. We detrended for all of the above sources while simultaneously fitting a transit model with `pycheops` to avoid removing transit features. Both our undetrended and detrended CHEOPS light curves are shown in Figure 19.

5.2.1. Noise Comparison to Other CHEOPS Targets

We report measured photometric noise as a function of Gaia G-band magnitude for our `PIPE`-extracted CHEOPS and detrended light curves and compare against other stars targeted by CHEOPS. Further, comparing to photon-limited noise serves as a check of in-flight performance. Using the "minimum errors" method described in Maxted et al. (2022), we calculated light-curve noise levels after subtraction of the best-fit transit model by finding the transit depth that can be detected at S/N of 1 at timescales including 1 minute, 10 minutes, 30 minutes, 1 hr, 3 hr, and 6 hr, as specified in Figure 10, assuming that our flux errors are minimum bounds on true errors in flux values. We compare to other CHEOPS targets (black points; courtesy of Thomas G. Wilson, priv. comm.). We also compare to photon-limited noise at 100% and 50% observing efficiency (black and red dashed lines, respectively), which were calculated using the CHEOPS exposure time calculator (ETC).[39]

In general, noise in our light curves seems to follow trends from other CHEOPS targets. While we do not add any targets to the CHEOPS sample brighter than eighth magnitude, we are able to fill a gap between magnitudes at about 9.5 and 11.5, where most of our targets reside. As such, it is evident that our targets exhibit slightly more noise than the photon-limited predictions, shown by the dashed line in each panel of Figure 10. This may be due to in-flight noise sources that were not well constrained prior to launch, including atmospheric airglow, CHEOPS's large PSF, hot pixels, and cosmic rays. Despite these sources of noise, in-flight performance appears largely to match what is expected, which is supported by our noise estimates (Fortier 2023, in preparation).

We note that while there appears to be low noise in many of our light curves, there is one notable exception. In particular, our TOI 244 CHEOPS light curve exhibits noise on midrange timescales (30 minutes to 3 hr) at much higher levels than other targets. TOI 244, our dimmest and therefore rightmost star on each panel, pulls farther away from the dashed line than any other target. This may have been impactful for our model

[39] https://cheops.unige.ch/pht2/exposure-time-calculator/

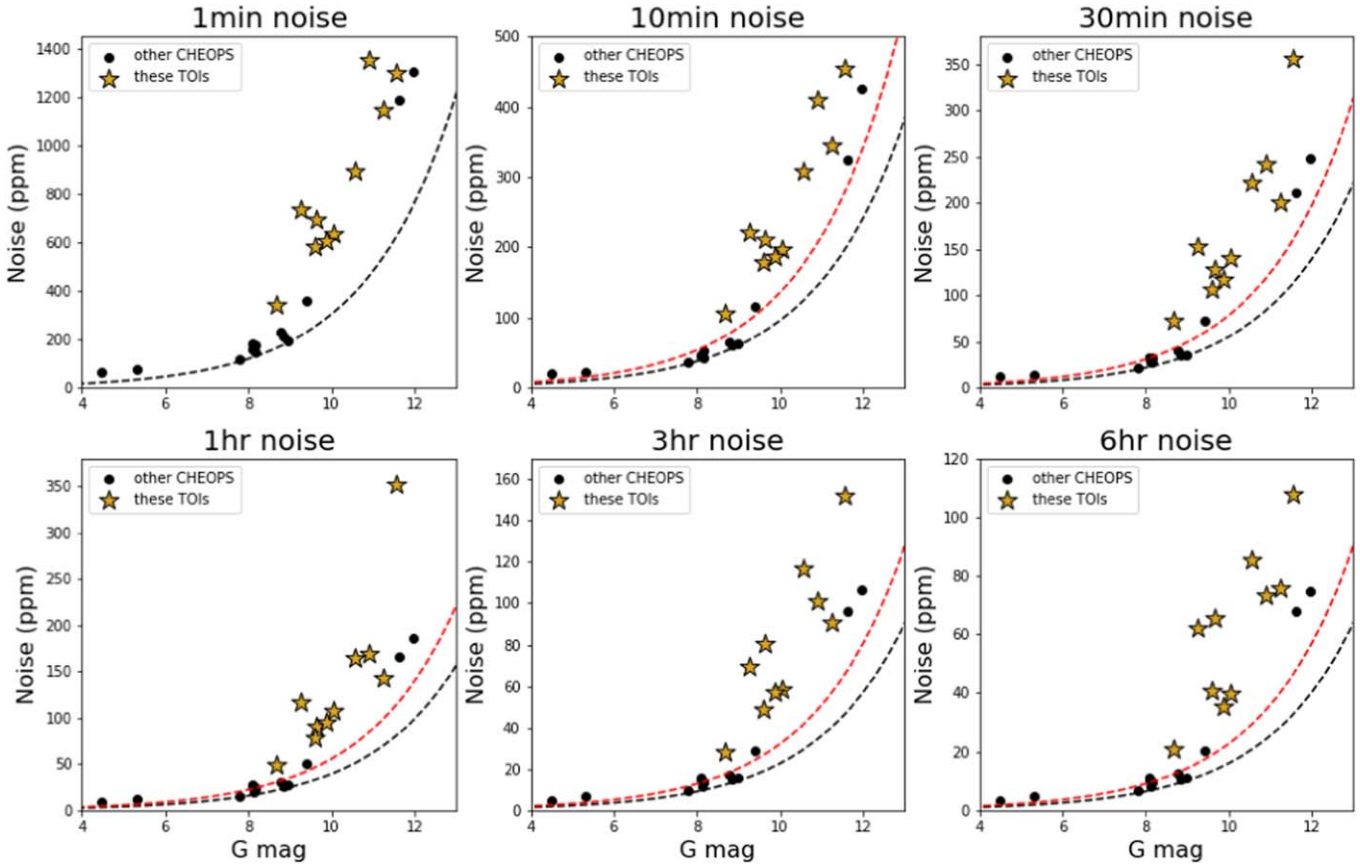

Figure 10. Measured photometric precision for these TOIs (yellow stars) and other CHEOPS targets (black circles, courtesy of Thomas G. Wilson) as a function of Gaia *G*-band magnitude. Black dashed lines represent photon noise limits assuming 100% observing efficiency, whereas red dashed lines represent photon noise limits assuming 50% observing efficiency. Different panels represent different integration times, where photon noise is averaged over the referenced timescale.

fitting, as we will discuss later. This is especially true given that noise on this timescale is approximately equivalent to the duration of a transit for a typical short-period planet (∼30 minutes to 3 hr).

5.3. Treatment of Time-correlated Red Noise

Time-correlated red noise in light curves can significantly bias fit results, and in some cases can lead to a nondetection of a transiting planet (Pont et al. 2006). Therefore, it must be accounted for in model fitting. We do so by following methods similar to those described in Winn et al. (2008) and Wong et al. (2021). Without including corrections for red noise in an initial run, we fit transit models to our TESS and CHEOPS light curves as described below. Then, we binned the residuals from the joint fit of both light curves for each system using our HOMEBREW method (described below) with n points in m bins (for a total of $\sim n \times m$ points in a whole light curve) and calculated the rms. This quantity represents the rms deviation from the model, which should follow a Gaussian $\sqrt{n}$ in the case of uncorrelated errors. We did this for bin sizes n from 1 to 1000, or the maximum number of points in the light curve if the number of points was less than 1000.

Although the rms deviation should follow a $\sqrt{n}$ trend with bin size, this quantity deviated from this trend in every case, presumably due to the presence of time-correlated noise. To account for red noise on the same timescale as a transiting planet, we found the mean deviation β from this trend when binning at 14 and 60 minutes, representing between seven points and 30 points in a bin for our two-minute-cadence TESS light curves and between 14 and 60 points per bin for our 60 s cadence CHEOPS light curves. This factor β differed for each light curve and was typically between one and two (as shown in Table 9). We then inflated our flux errors for each point in each light curve by this factor β. We did so because our previous flux error values were calculated using purely Poisson statistics and were assumed to have no correlated noise, and inflating them in this way is one way to account for red noise to first order (Pont et al. 2006). We then used these new flux error values to rerun our fits and calculate new model parameters, which are reported as our final model fits.

Table 9
β Factors for Each of Our Light Curves, Which Were the Factors by Which We Inflated Our Flux Errors in Order to Account for Red Noise

TOI	CHEOPS	TESS
TOI 118	1.87	1.29
TOI 198	1.91	1.35
TOI 244	1.23	1.19
TOI 262	1.45	1.25
TOI 444	1.58	2.20
TOI 455	2.08	2.35
TOI 470	1.39	1.26
TOI 518	1.62	1.27
TOI 560	2.25	1.90
TOI 562	1.23	1.29

5.4. Modeling

Accurate modeling of a transiting planet across the face of a star is the cornerstone of transcribing photometric data to a set of physical parameters that describe the system. An important piece of accurately modeling transits is the function by which stellar limb darkening is parameterized, which is the subject of much discussion in recent literature (Müller et al. 2013; Espinoza & Jordán 2016; Morello et al. 2017; Neilson et al. 2017). The power-2 limb darkening law (Hestroffer 1997) is a two-parameter form of limb darkening that is both fast and accurate to compute (Maxted & Gill 2019). It is the limb darkening law that is implemented in `pycheops` as qpower2, so we use this parameterization throughout our fits in order to maintain consistency in modeling. The "power-2" limb darkening law follows the functional form

$$I(\mu) = I_o[1 - c_1(1 - \mu^{c_2})], \quad (1)$$

where $\mu = \sqrt{1 - x^2}$ is the projected radial coordinate and I_o is a normalization constant.

In all our models and fits, we use the Python Limb Darkening Toolkit (PyLDTK; paper: Parviainen & Aigrain 2015; code: Parviainen 2015) to calculate stellar limb darkening coefficients. Given a set of stellar parameters as input, PyLDTK uses the library of PHOENIX-generated specific intensity spectra by Husser et al. (2013) to calculate stellar limb darkening coefficients for a given model. We provide estimations of stellar effective temperature, surface gravity ($\log g$), and metallicity, which were obtained from previous publications for known planets or obtained from our SED analysis or spectroscopic characterization for newly validated planets. In addition, we provide the bandpass for which the coefficients are calculated, by providing preexisting TESS and CHEOPS throughput curves. This meant that these coefficients were slightly different for TESS and CHEOPS photometry. We specified the model input as power-2, which gave us limb darkening coefficients for this law, as well as uncertainties on these values. We chose to keep limb darkening coefficients for each star in each bandpass constant through all fits and models for two reasons: to reduce uncertainties on other values, and because neither the TESS nor the CHEOPS photometry is sufficiently precise to allow a meaningful constraint on the limb darkening coefficients.

From fitting a model of a transiting planet to a light curve, we can recover many system parameters. These may include transit depth D (related to the radius ratio of the planet and star as $D = (R_p/R_*)^2$), the time of mid-transit T_o (reported as a time in BJD), the orbital period P (reported in days), and the impact parameter b, which is the sky-projected distance between the stellar midline and the chord traced by the planet across the face of the star, and is thus a scaled value from zero to one. b in turn is related to the semimajor axis a of the orbit for the planet, scaled to the radius of the star, and the planet's orbital inclination with respect to Earth i (reported in degrees). However, different models report these orbital and physical parameters in different ways. For example, the `batman` (Kreidberg 2015) transit model directly fits for orbital inclination i in degrees, meaning impact parameter is a derived quantity, whereas `juliet` directly fits for a parameterization of impact parameter b, meaning orbital inclination is a derived quantity. Therefore, we delineate between fitted and derived quantities for different models in Table 10. The ways in which our model parameterizations differ from one another may account for some deviation in results, despite the fact that parameterizations of many parameters frequently depend on one another.

Table 10
Distinction between Fitted and Derived Properties for Our Various Models

Parameter	`pycheops`	HOMEBREW	`juliet`
Time of mid-transit T_o	fitted	fitted	fitted
Orbital period P	fitted	fitted	fitted
Planet-to-star radius ratio $k = R_p/R_s$	derived	fitted	fitted
Transit depth $D = (R_p/R_s)^2$	fitted	derived	derived
Impact parameter $b = (a/R_s)\cos(i)$	fitted	derived	fitted
Scaled semimajor axis (a/R_s)	fitted	fitted	derived
Orbital inclination i	derived	fitted	derived
Stellar density ρ_s	derived	derived	fitted
Planet radius $R_\oplus$	derived	derived	derived

One of the primary goals of this work is to compare photometric performance between TESS and CHEOPS. One way in which we do this is by comparing model values and uncertainties in transit depth. Transit depth represents a solid metric of comparison because in all cases it is either computed directly by our models or singularly calculated from one other model parameter that is itself fitted directly. Therefore, uncertainties in transit depth are propagated directly from our fits (in the case of `pycheops`) or from only planet-to-star radius ratio.

5.5. Fitting

We used a variety of fitting methods, including MCMC sampling with `emcee` (Foreman-Mackey et al. 2013) and nested sampling with `dynesty` (Speagle 2020). We compare these methods of fitting in order to gauge their effects on the model output uncertainties.

We used different fitting codes for different data sets. `pycheops` is primarily useful for detrending and fitting transit models to CHEOPS light curves, so we used it exclusively on our CHEOPS light curves. Then, we developed our HOMEBREW code for use with both CHEOPS and TESS light curves. Finally, we used `juliet` for both CHEOPS and TESS light curves. We describe each below.

5.5.1. `pycheops: lmfit + emcee`

For our runs with `pycheops` (Maxted et al. 2022), we used the built-in nonlinear least-squares minimization `lmfit` to initially constrain model parameters, and then passed these results to the MCMC sampler `emcee`, which is also built into the functionality of `pycheops`. We employed `lmfit`.

Parameter objects, which are model parameters that can be either varied or kept constant, depending on the part of the model one is constraining. We supplied a loose set of priors for the initial model generation, which were retrieved by the authors from ExoFOP TESS. As previously stated, detrending parameters and limb darkening coefficients are held constant, and we fit for only physical and orbital parameters of the planet. We applied this fitting framework only to CHEOPS photometry. For our MCMC sampler runs, we initialized 80 walkers around the best-fit values provided by the nonlinear least-squares minimization, ran 300 steps of burn-in, and then ran for 1000 steps, at which point we verified the sampler converged for each system by checking the convergence time.

5.5.2. HOMEBREW: Least-squares Minimization + emcee

We built a similar framework as in the previous subsubsection to fit both TESS and CHEOPS photometry, which we call our HOMEBREW method. This code is distinct because we used it to fit models to both data sets, including individual fits and joint fits to both data sets, whereas we used pycheops exclusively for CHEOPS photometry. Therefore, we generated three results for each system with this framework, including one each for TESS and CHEOPS and one that was jointly fitting both data sets. We began by initializing a model in batman, which is informed by the same initial values drawn from ExoFOP TESS as for pycheops. For our fits to CHEOPS and TESS separately, our model fits orbital parameters jointly, but computes a different depth for each data set. For our joint fits to both data sets, all model parameters converge to the same value, including transit depth. We designed our fitting code in this way to strictly examine transit depths and uncertainties on this value, thus maintaining consistency among orbital parameters.

We found an initial model with least-squares minimization by employing the scipy.optimize function. These model parameters are then passed to the MCMC sampler emcee with uniform priors. We initialized 48 walkers for fits to CHEOPS and TESS data, and 40 walkers for fits to both data sets jointly. This is because we fit for one fewer parameter for joint fits, as there is only one transit depth to compute across both data sets. For both types of fits, we ran the MCMC sampler for a burn-in phase of 500 steps, and then ran for 1500 more steps, for a total of 2000 steps. The results of these fits are displayed as corner plots using corner (Foreman-Mackey 2016).

5.5.3. Juliet: Nested Sampling with Dynesty

As a final fitting framework, we used nested sampling as implemented in juliet (Espinoza et al. 2019). Nested sampling is a method of estimating Bayesian evidence for a set of model parameters and allows for the ability to robustly sample from a high-dimensional, multimodal parameter space. Such an algorithm relies on integrating the prior in nested shells of constant likelihood (Speagle 2020). We modified the base code of juliet slightly to include the power-2 limb darkening law. We initialized a transit model in juliet, which is built from the batman transit model, and then applied nested sampling with dynesty to find convergence. We applied this framework to TESS and CHEOPS photometry separately and also used it to find a global fit across both data sets, generating three more results for each system. Given juliet's model parameterization, we were not able to completely maintain consistency between fits by fitting for certain parameters separately. Therefore, we generated one complete set of model parameters each for TESS and CHEOPS light curves separately, and one more complete set of model parameters for our global fits. In Section 6, we verify consistency between parameters generated with HOMEBREW and juliet.

5.6. Comparing TESS and CHEOPS Precision

An overall goal of this work is to compare the relative photometric performances of TESS and CHEOPS. As previously stated, CHEOPS's larger primary aperture size and smaller pixel scale make it a higher-precision instrument relative to TESS. However, as a survey mission, TESS has the advantage of capturing more transits on average per target relative to CHEOPS. Further, the lower observing efficiency, $\epsilon_{\rm CHEOPS,}$ of CHEOPS will increase model uncertainties. As such, we expect that uncertainties in transit depth should theoretically scale according to photon-limited precision as

$$\sigma_{1,\rm TESS} = \sigma_{\rm TESS}\sqrt{N_{\rm tr,TESS}\epsilon_{\rm TESS}} \tag{2}$$

and

$$\sigma_{1,\rm CHEOPS} = \sigma_{\rm CHEOPS}\sqrt{N_{\rm tr,CHEOPS}\epsilon_{\rm CHEOPS}}. \tag{3}$$

Here, we define $\epsilon_{\rm CHEOPS}$ to be the CHEOPS observing efficiency, which we calculate as the number of data points in transit divided by the number of points that should constitute the whole transit given the sampling cadence of 60 s. $\epsilon_{\rm TESS}$ is similarly defined for TESS observations, calculated according to the TESS observing cadence. Further, we define $N_{\rm tr,...}$ as the number of transits in our light curves for either TESS or CHEOPS. Finally, $\sigma_{\rm CHEOPS}$ and $\sigma_{\rm TESS}$ represent depth uncertainties as reported by our models, and $\sigma_{1,\rm CHEOPS}$ and $\sigma_{1,\rm TESS}$ represent depth uncertainties on one ideal CHEOPS or one ideal TESS transit, respectively. As shown by Equations (2) and (3), the reported model uncertainty would be modified by the number of transits captured by a given telescope, as well as the observing efficiency of that telescope for a given target. Uncertainty on one ideal transit would be larger than reported model uncertainty if more than one transit is observed, whereas uncertainty on one ideal transit would be smaller when accounting for observing efficiency. Importantly, we assume that transit coverage with TESS is 100%, meaning we set $\epsilon_{\rm TESS} = 1$ in all cases. This is a safe assumption for our targets as shown in Figure 21, which demonstrates that our transit coverage with TESS for each target is full. However, this is not always the case for TESS observations, as there are instances in which data downlink interrupts transit coverage or photometry is corrupted by stray light. Therefore, TESS observing efficiency ought to be included in general applications of this analysis.

Theoretical photon-limited performance depends on the photon flux of a given star in the relevant bandpass, as well as background and read noise. However, we neglect the contributions from background and read noise, as these are assumed to be sufficiently accounted for during image subtraction and light-curve generation. To compute the ideal theoretical performance for a system, we ought to evaluate the number of captured photons per time. This will be an SED-

dependent ratio between CHEOPS and TESS. The effective wavelengths of the two bandpasses are about 581 nm and 746 nm for CHEOPS and TESS, respectively, meaning there are about 28% more photons per energy in the TESS band. However, CHEOPS has a primary aperture size three times larger than that of TESS, meaning both of these factors should be accounted for.

This implies the following:

$$\frac{\sigma_{1,\mathrm{TESS}}}{\sigma_{1,\mathrm{CHEOPS}}} = \sqrt{\frac{N_{\mathrm{photons,CHEOPS}}}{N_{\mathrm{photons,TESS}}}} = \sqrt{q} \tag{4}$$

where

$$N_{\mathrm{photons}} = A \int \mathrm{SED}(\lambda) F(\lambda) d\lambda \tag{5}$$

and

$$\mathrm{SED}(\lambda) \propto \frac{\mathrm{Energy}}{\mathrm{area} \cdot \lambda \cdot \mathrm{time}}. \tag{6}$$

We have defined q to be the photon ratio between CHEOPS and TESS, SED(λ) to be the wavelength-dependent energy flux per unit time, and $F(\lambda)$ to be the filter function of a given telescope. To find q, we computed the expected energy fluxes for CHEOPS and TESS for a range of model spectra, assuming 100% efficiency for both telescopes. Combining the above, we expect the following ratio of uncertainty in depth:

$$\frac{\sigma_{\mathrm{CHEOPS}}}{\sigma_{\mathrm{TESS}}} = \sqrt{\frac{N_{\mathrm{tr,TESS}}}{N_{\mathrm{tr,CHEOPS}}} \frac{\epsilon_{\mathrm{TESS}}}{q \epsilon_{\mathrm{CHEOPS}}}}. \tag{7}$$

Physically, this means that given the ~3: 1 primary size ratio of CHEOPS to TESS, we would expect that the precision on the depth of one CHEOPS transit should be equivalent to the precision in depth of nine phase-folded TESS transits ($q \approx 9$ in most cases) in the case that the star is equally as bright in both bandpasses and assuming perfect observing efficiency. Equation (7) allows us an effective tool for comparison between these two telescopes even given different observing efficiencies and numbers of transits for each target.

5.6.1. How Many TESS Transits Would We Need to Reach the Same Precision as a Single CHEOPS Transit?

Using the above formulation, we can approach the question of how many TESS transits it would take to reach the precision in one CHEOPS transit. Similar to the way that Equations (2) and (3) show that noise scales as $1/\sqrt{N_{\mathrm{tr}}}$, we can solve for the number of transits needed to equate the precision on one idealized CHEOPS transit and the precision on one idealized TESS transit as

$$\sigma_{1,\mathrm{CHEOPS}} = \sigma_{1,\mathrm{TESS}} \sqrt{N_{\mathrm{tr,equiv}}}. \tag{8}$$

According to photon-limited noise, the number of TESS transits we expect ought to satisfy the above equation is equal to the photon ratio q for any given system. However, by solving Equation (8) for the number of equivalent transits, $N_{\mathrm{tr,equiv}}$, and applying Equations (2) and (3), we arrive at our actual value for the number of equivalent transits as

$$N_{\mathrm{tr,equiv}} = \left(\frac{\sigma_{\mathrm{TESS}}}{\sigma_{\mathrm{CHEOPS}}}\right)^2 \frac{N_{\mathrm{tr,TESS}}}{N_{\mathrm{tr,CHEOPS}}} \frac{\epsilon_{\mathrm{TESS}}}{\epsilon_{\mathrm{CHEOPS}}}. \tag{9}$$

The above equation is generalizable when comparing depth precisions, number of transits obtained, and in-transit observing efficiencies for any two telescopes. Then, Equation (9) can then be interpreted as the total number of transits required with a given telescope to match the precision in depth as measured with the other telescope.

6. Results

In this section, we report physical and orbital parameters for each of our systems. We will highlight some specific examples of interest, but ultimately discuss the results of our fitting in the aggregate. Discussion of particular systems is left to Section 7. Our goal is to compare the performance of CHEOPS relative to the foreseen prelaunch performance estimates via comparison of their depth uncertainties using different fitting methods. Aggregate depth results for each of our fits are shown in Table 11.

For each target, we have calculated the orbital properties with both our HOMEBREW method and `juliet`. However, for simplicity, we report final orbital and physical properties from only our HOMBREW method.

6.1. Fractional Depth Uncertainty Comparison between TESS and CHEOPS

Here we seek to compare the fractional depth uncertainties yielded by different fitting methods for our photometric data sets. We define fractional depth uncertainty as the reported model uncertainty in transit depth divided by transit depth normalized to a percentage. Comparing fractional uncertainty in depth allows us to compare uncertainties in our fitted model parameters without propagating uncertainties from stellar radius, giving us a straightforward comparison of model performance. Figure 11 shows our calculated fractional depth uncertainties for our different modeling and fitting methods, where each bar plot represents a different method for each of our data sets. The top panel shows fractional depth uncertainties for our HOMEBREW method, which consists of fitting a `batman` transit model to our photometric data with `emcee`, the MCMC sampler. The middle panel shows these quantities for our fits using `juliet`, which fits a `batman` transit model using `dynesty`, the dynamic nested sampler. The bottom panel shows the fractional depth uncertainty for fits using `pycheops`, which fits a transit model using `emcee`, the MCMC sampler. The first two panels show fractional depth uncertainties represented as percentages for models computed with TESS data alone (red), CHEOPS data alone (purple), and both data sets jointly (light green), whereas the bottom panel is only for CHEOPS data alone (purple). We have included a horizontal 10% fractional uncertainty target line as a guide for comparison. Comparing fractional uncertainties between data sets and fit methods allows us to compare the photometric properties of these light curves. All panels are normalized to the same vertical axis for uniform comparison.

Inspection of the top panel of Figure 11 shows that many of our fits computed with our HOMEBREW method are below the 10% fractional uncertainty threshold, although there are some notable exceptions. In comparing the fits with TESS photometry alone and CHEOPS photometry alone, we see that for five out of 10 systems, the fractional uncertainties when fitting CHEOPS data alone are lower than those fitting TESS

Table 11
Calculated Transit Depths for Our 10 Systems, Reported in ppm

		TOI 118	TOI 198	TOI 244	TOI 262	TOI 444	TOI 455	TOI 470	TOI 518	TOI 560	TOI 562
CHEOPS only	pycheops	1477 ± 79	1030 ± 102	630 ± 85	538 ± 97	1476 ± 151	1180 ± 85	2563 ± 92	750 ± 150	1500 ± 80	1102 ± 55
	HOMEBREW	1936 ± 238	1018 ± 89	650 ± 112	454 ± 66	1129 ± 81	1024 ± 90	2450 ± 135	640 ± 91	1459 ± 74	973 ± 45
	juliet	1697 ± 247	1009 ± 140	831 ± 100	600 ± 100	1130 ± 81	1171 ± 99	2177 ± 168	646 ± 61	1541 ± 196	1148 ± 78
TESS only	HOMEBREW	1624 ± 210	807 ± 102	841 ± 93	471 ± 65	930 ± 79	2172 ± 168	2061 ± 136	471 ± 100	1122 ± 60	949 ± 37
	juliet	1702 ± 124	871 ± 130	1100 ± 113	566 ± 65	994 ± 126	2335 ± 126	2119 ± 157	622 ± 100	1218 ± 140	1046 ± 39
TESS + CHEOPS	HOMEWBREW	1414 ± 68	894 ± 64	773 ± 95	484 ± 66	1056 ± 46	1665 ± 82	2275 ± 76	605 ± 64	930 ± 56	955 ± 62
	juliet	1549 ± 202	844 ± 64	967 ± 93	586 ± 61	1068 ± 49	1652 ± 105	2071 ± 200	660 ± 62	1235 ± 63	1056 ± 34

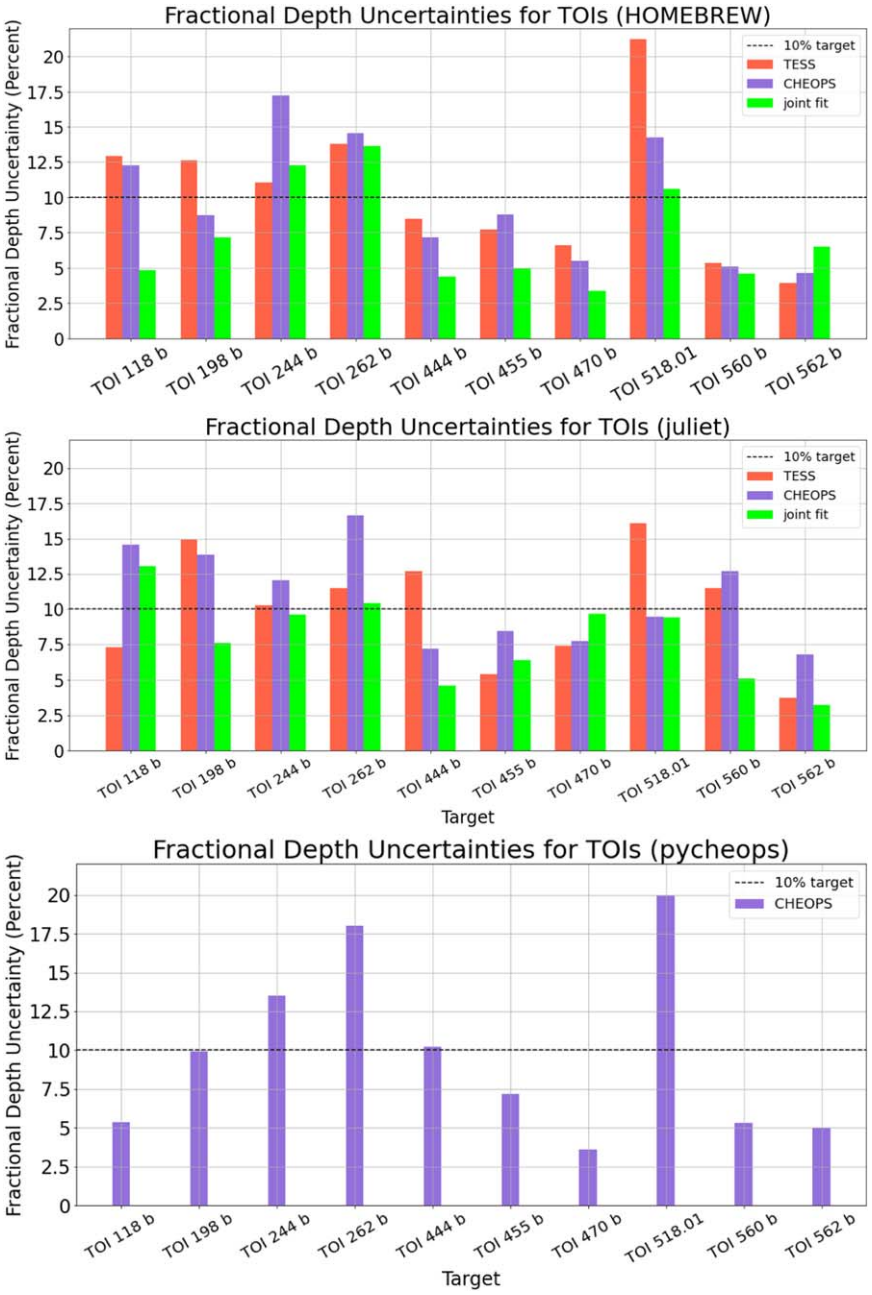

Figure 11. Fractional depth uncertainties for our nine planets and one planet candidate, which is uncertainty in transit as a fraction over calculated transit depth. Top: fractional depth uncertainty for our HOMEBREW method, which consists of fitting a `batman` transit model with `emcee`. Middle: fractional depth uncertainty using `juliet` nested sampling. Bottom: fractional depth uncertainty using `pycheops` transit model with `emcee`. For all panels, models fitted to TESS data only are represented by red bars, models fitting to CHEOPS data only are represented by purple bars, and models fitting to both data sets jointly are represented by light green bars. A 10% fractional uncertainty line is shown for both panels as a guide.

data alone. For eight of our 10 planets, excluding only TOI 244 b and TOI 562 b, we report the lowest fractional uncertainties in depths when using jointly computed models as opposed to either TESS or CHEOPS alone. In the case of both TOI 244 b and TOI 562 b, we report the lowest fractional depth uncertainty using the HOMEBREW method for TESS data alone. Given these results, we can see that in more cases, our HOMEBREW model fits yield lower relative uncertainties to TESS data alone as compared with fits to CHEOPS data alone. Additionally, joint fits to both data sets yield lower uncertainties in more cases and also yield a lower average fractional uncertainty in depth across the ensemble relative to fits to individual data sets.

We examine the cases of larger-than-10% fractional depth uncertainty calculated with the HOMEBREW method in Section 7, including individual fits to TESS data and CHEOPS data for TOI 118 b, our fit to TESS data alone for TOI 198 b, and all our fits to TOI 244 b, TOI 262 b, and TOI 518.01.

We may also compare our fractional depth uncertainties as computed using `juliet`, as shown in the middle panel of Figure 11. There are more fits that do not meet the 10% fractional depth uncertainty threshold using `juliet` compared with our HOMEBREW method. This may have been because orbital parameters were fitted separately for individual fits to TESS and CHEOPS photometry. For seven out of our 10 systems, including TOI 198 b, TOI 244 b, TOI 262 b, TOI 444

b, TOI 518.01, TOI 560 b, and TOI 562 b, we report the lowest fractional uncertainties in depths when using jointly computed models as opposed to either TESS or CHEOPS alone. When comparing fits to TESS data alone and to CHEOPS data alone for `juliet`, we see that fits to CHEOPS data alone yield smaller fractional depth uncertainties for only three out of 10 planets compared with fits to TESS data alone. As an ensemble, these results indicate that while fits to CHEOPS data yield lower uncertainties in fewer cases compared with TESS data, our fits to both data sets jointly yield lower uncertainties more often than either data set alone.

We examine cases of fractional depth uncertainty larger than 10% calculated with `juliet` in Section 7, including fits to TESS data alone for TOI 198 b, TOI 244 b, TOI 262 b, TOI 444 b, TOI 518.01, and TOI 560 b, as well as our fits to CHEOPS data alone for TOI 118 b, TOI 198 b, TOI 244 b, TOI 262 b, and TOI 560 b.

Finally, we compare fractional depth uncertainties for our `pycheops` fits to CHEOPS visits to each target. There are four out of 10 instances in which the fractional depth uncertainty is larger than 10%. We report that the largest fractional depth uncertainty with this fit method was for TOI 518 b, which is also the case for the other fit methods as above. We discuss potential causes for these high uncertainties below.

6.2. Radius Estimates

Here we compare our radius estimates for different fit methods with those from SPOC data validation reports to their PM and EM sector light curves. We calculate planet radius by multiplying the radius ratio of the planet to the star as returned by our models by the radius of the star. For consistency, we use stellar radius values from published results for those systems that have been previously validated, and stellar radius values from our SED analysis of new systems, as in Section 3.1. SPOC DV report planet radii are calculated by multiplying the radius ratio by the stellar radius as listed in the TIC. Figure 12 shows our radius estimates and their uncertainties, propagating uncertainties from both stellar radius and uncertainties in model parameters. The top panel shows our radius estimates from fits using our HOMEBREW method, the middle panel shows our radius estimates from fits using `juliet`, and the bottom panel shows our radius estimates using `pycheops`. In all panels, red bars represent fits to TESS data alone, purple bars represent fits to CHEOPS data alone, and light green bars represent joint fits to both data sets. In each panel, we also include SPOC (a.k.a. TESS project) values and their uncertainties in lightly shaded orange, which allows us a side-by-side comparison of our fits and their uncertainties to these values.

In nearly every case, our fits and models yield a decrease in radius uncertainty relative to their initial uncertainties as calculated by the SPOC pipeline. The only instances in which the radius uncertainties we report with our models are larger than the SPOC radius estimates are our HOMEBREW fits to TESS data alone and CHEOPS data alone for TOI 118, our `juliet` fits to CHEOPS data alone and our joint fit for TOI 118, and our `pycheops` fit to CHEOPS data for TOI 444. Notably, all of our radius estimates are reported with smaller uncertainties for our HOMEBREW joint fits.

We can check consistency between different fits and methods for each system. To do so, we compare radius estimates within 1σ. For our fits using the HOMEBREW method, our radius estimates are self-consistent for all systems, except for TOI 455 b. Whereas radius estimates generated with CHEOPS data, TESS data, or both for all other systems were consistent with one another, our radius estimates computed with TESS and CHEOPS separately are discrepant to nearly 4σ in the case of TOI 455 b as calculated with our HOMEBREW results. Further, discrepancies between the joint fit value and the value calculated with either data set alone are discrepant to $\sim 2\sigma$, where the joint fit estimate sits between the estimate calculated with either data set alone. We discuss potential reasons for this in Section 7.1.6.

Similar to our HOMEBREW method, the only system that exhibits a radius estimate discrepancy as calculated with `juliet` is TOI 455 b, where radius estimates calculated from TESS photometry and calculated jointly are discrepant to $\sim 2\sigma$. The radius estimate for this planet calculated with CHEOPS photometry is not consistent with those calculated either with TESS or jointly. We discuss potential reasons for this in the following section.

The fits that most frequently exhibit the largest deviation between radius estimates are those calculated with `pycheops` for CHEOPS photometry only and with our HOMEBREW method for TESS photometry. In six out of 10 cases, our fits with `pycheops` to CHEOPS photometry yield larger radius estimates relative to those fits calculated with our HOMEBREW method to TESS photometry. However, many of these fits are still consistent, with the exception of TOI 455 b.

We report radius measurements to better than 10% precision for all 10 of our systems, even after incorporating uncertainties in stellar radius. This shows that high-precision results can be obtained from analysis of photometry alone, although our results would be improved by further high-precision characterization of the host stars. Future work could include combining our photometric analysis methods with more precise characterization of the host stars, such as with an ultra-high-precision instrument like Gaia or closer analysis of spectroscopic observations.

6.3. Comparing TESS and CHEOPS Photometry

Table 12 shows our values used for calculation of theoretical predictions for the uncertainty ratio as in Equation (7). The table includes CHEOPS observing efficiency, the number of transits captured by CHEOPS and TESS for each target, and the SED-dependent flux ratio, which wraps contributions from both aperture size and stellar spectral type. Although the CHEOPS DRP gives us a value for observing efficiency, which is the total number of points in the light curve over the number of points that should be in the light curve given the observing cadence of 60 s, we recalculate this value specifically for points in transit. Thus, our observing efficiency is calculated as the number of points in transit over the number of points that should be in transit assuming full coverage with the given observing cadence. This is an important distinction in the case of TOI 470 b, for example, where we captured only a partial transit and had no pre-transit baseline.

The comparison between our theoretical uncertainty ratios given by Equation (7) and our actual uncertainty ratios are shown in Figure 13, where the black bar represents our theoretical value for the ratio of uncertainty in depth from CHEOPS photometry versus TESS photometry, which incorporates CHEOPS observing efficiency and the number of transits captured by both telescopes. Our actual depth uncertainty ratios for our HOMEBREW fits are given by the

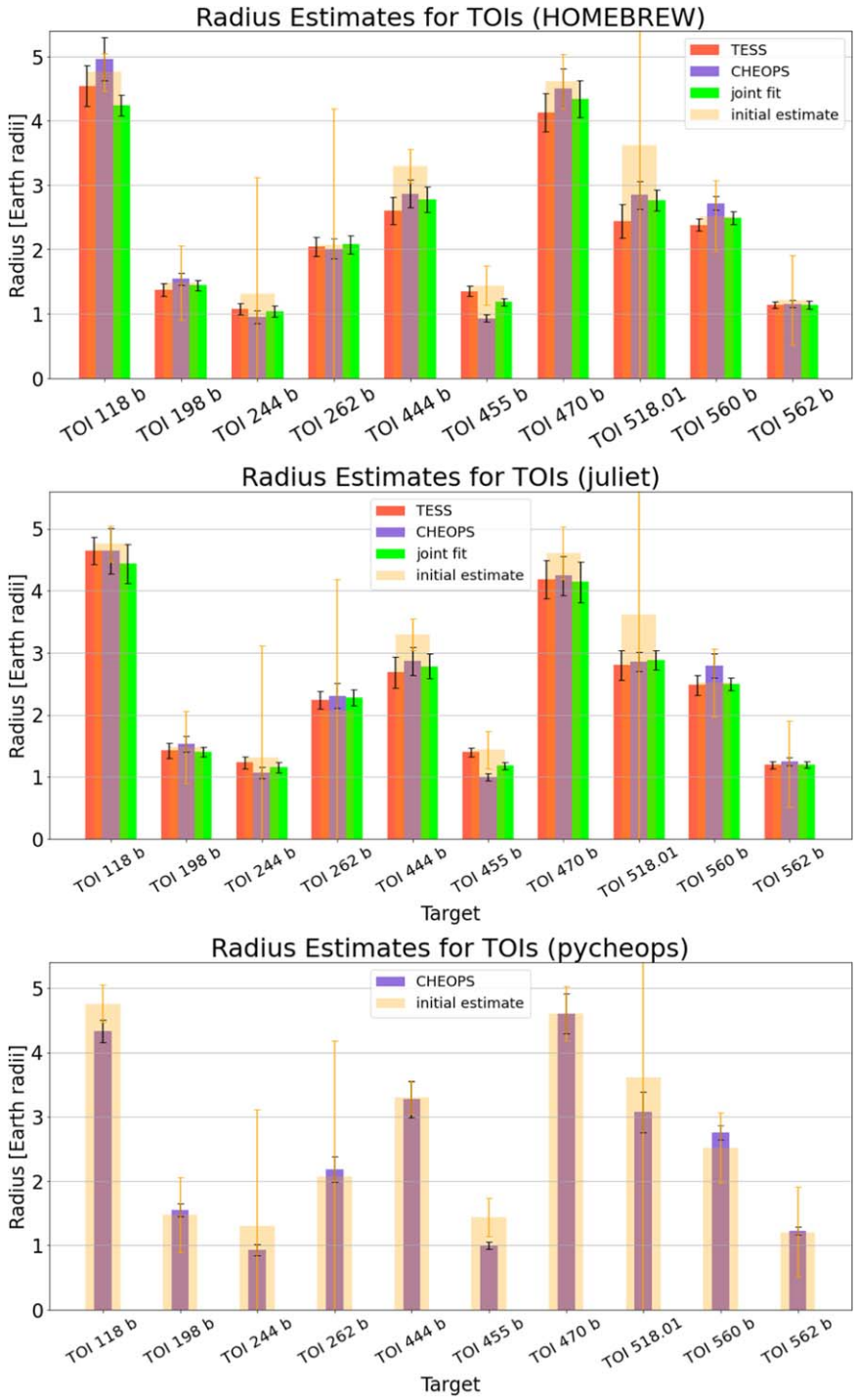

Figure 12. Radius estimates for our 10 planets. Top: radius estimates for our HOMEBREW method, which consists of fitting a `batman` transit model with `emcee`. Middle: radius estimates using `juliet` nested sampling. Bottom: fractional depth uncertainty using a `pycheops` transit model with `emcee`. For all panels, models fitted to TESS data only are represented by red bars, models fitted to CHEOPS data only are represented by purple bars, and models fitted to both data sets jointly are represented by light green bars. The lighter-shaded orange bars represent the initial radius estimates from TESS PM sectors.

red bar for each target. A horizontal dotted line has been placed at 1.0 to guide the eye, which represents a theoretical system with one CHEOPS transit with perfect observing efficiency and nine TESS transits. In many cases, the theoretical prediction is below 1.0, meaning we would expect for model uncertainties as calculated with CHEOPS to be lower than those calculated with TESS, even accounting for the number of transits and CHEOPS observing efficiency. However, given the relative number of photons collected by these telescopes in their respective bandpasses and the number of observed transits, there are four systems in which we may have expected slightly higher uncertainties as calculated with our CHEOPS light curves relative to TESS light curves.

To judge relative performance and compare model uncertainties for each target, we compare the heights of the bars for each of our planets in Figure 13. Our model uncertainties should approach the theoretical values, and thus be represented by the black bars, but are represented in reality by the red bars.

Table 12
Values for Calculation of Theoretical Depth Uncertainty Comparison, Including CHEOPS Observing Efficiency ϵ, Number of Transits Captured by CHEOPS and TESS respectively, and Ratio of Flux of TESS to CHEOPS Band

System	$\epsilon_{\rm CHEOPS}$	$N_{\rm tr,CHEOPS}$	$N_{\rm tr,TEESS}$	q	$N_{\rm tr,equiv}$	Depth (ppm)
TOI 118 b	0.488	1	8	9.47	12.76	1414 ± 68
TOI 198 b	0.955	1	4	6.23	5.50	894 ± 64
TOI 244 b	0.744	2	8	5.89	3.70	773 ± 95
TOI 262 b	0.870	1	4	9.10	4.46	484 ± 66
TOI 444 b	0.864	1	5	8.95	5.50	1056 ± 46
TOI 455 b	0.882	1	8	5.70	31.60	1665 ± 82
TOI 470 b	0.700	1	4	8.89	5.80	2275 ± 76
TOI 518.01	0.610	2	2	10.02	1.98	605 ± 64
TOI 560 b	0.680	1	7	7.72	6.77	1225 ± 56
TOI 562 b	1.000	1	10	6.15	6.76	955 ± 62

Note. We also give the number of equivalent transits, calculated according to Equation (8), and compare to transit depth and uncertainty as obtained with our HOMEBREW joint fits.

The metric for comparison is uncertainty in depth calculated with CHEOPS photometry versus that calculated with TESS, so a red bar that is higher than the black indicates that the uncertainty in depth as calculated with CHEOPS is higher than theoretically expected. In eight of 10 cases, we see that our calculated uncertainty ratio is higher than our theoretical value, indicating that our model uncertainties as calculated with CHEOPS are slightly higher than predicted, even when incorporating the number of transits and the observing efficiency of CHEOPS. In two cases, including TOI 118 and TOI 455, we see that the uncertainty as calculated with our CHEOPS light curves is lower than expected. This may be due to one of two causes. First, this may indicate that our model uncertainties as calculated with CHEOPS photometry were smaller than predicted. Conversely, this may indicate that our model uncertainties as calculated with TESS photometry were larger than expected, given the number of transits we observed. In the case of TOI 118 b, we expect that this uncertainty ratio should be $\frac{\sigma_{\rm CH}}{\sigma_{\rm TE}} \sim 1.3$, which may have been informed by a low measure for CHEOPS in-transit visit efficiency for this system at $\epsilon_{\rm CHEOPS} = 0.488$. However, we found an uncertainty ratio $\frac{\sigma_{\rm CH}}{\sigma_{\rm TE}} \sim 1.1$, meaning that our measure for uncertainty in the CHEOPS depth was lower than predicted relative to TESS. We believe this may have been due to extremely low noise in our light curve, which exhibited a MAD = 220 ppm in the detrended light curve, as well as solid in-transit and out-of-transit baselines. Therefore, despite the poor transit coverage, which would otherwise inflate the expected uncertainty, the reported uncertainty was low.

We also examine the case of TOI 455 b more closely. We believe evidence supports the second case, where model uncertainties calculated with TESS photometry were inflated relative to those calculated with CHEOPS photometry. The fact that this is a hierarchical triple-star system complicates the light curve immensely and would dilute the transit signals, which may have led to actual deviation in transit depth between different transits in our TESS light curve. This in turn would increase model uncertainties as convergence would be more difficult to reach. On the other hand, given that we had only one CHEOPS transit to analyze, convergence would more easily be reached in this case. In general, this showcases the impact that contamination from nearby stars can have on results and their uncertainties, and thus we recommend careful treatment of contamination in future studies.

Further, in three out of six cases when we expected that model uncertainties calculated with CHEOPS photometry would be lower than those calculated with TESS photometry, we actually find that our uncertainty ratio is higher than 1.0, indicating that model uncertainties as calculated with TESS were lower in these instances. These findings would indicate that our models fitted to CHEOPS photometry yield higher uncertainties than we might have predicted, which has implications for fitting models to CHEOPS photometry in the future. We believe that this finding is due to two primary reasons, including (1) important data gaps in CHEOPS visits, and (2) the way in which both CHEOPS and TESS light curves are generated and detrended. In a few instances, we saw inflated model uncertainties in fits to CHEOPS light curves that may have been the result of gaps in the transit in important places. These gaps are difficult to account for and are a consequence of the CHEOPS observing strategy and its low-Earth orbit. On the other hand, we may have seen larger-than-expected errors on models fitted to CHEOPS photometry due to the way in which these light curves are detrended. Each of our CHEOPS light curves were detrended individually by introducing detrending parameters one by one, meaning there is no standard method with which to detrend CHEOPS photometry. On the other hand, TESS light curves are all processed by the same pipeline, which treats the data uniformly. We believe that while the methods we used to detrend CHEOPS data from both instrumental and astrophysical systematics (outlined in Section 5) were effective, they may not have treated the data uniformly, which would introduce errors relative to a uniform treatment of TESS data.

6.3.1. How Many TESS Transits Do We Need to Reach the Same Precision as Our CHEOPS Transits?

Figure 14 shows the number of TESS transits necessary to match the precision we obtained on our CHEOPS transits, where our sample of planets is shown as a series of red dots. These are directly calculated from Equation (8). We compare to the theoretical expectation, q, which depends on stellar spectral type, shown as a black dashed line. For points that sit below the line, we obtained at least enough TESS transits to match the precision of our CHEOPS transits, but for the two systems above the line, we would require $N_{\rm tr,equiv} - N_{\rm tr,TESS}$ more TESS transits to match the precision of our CHEOPS transits. Clearly, according to our calculations, we would require many more

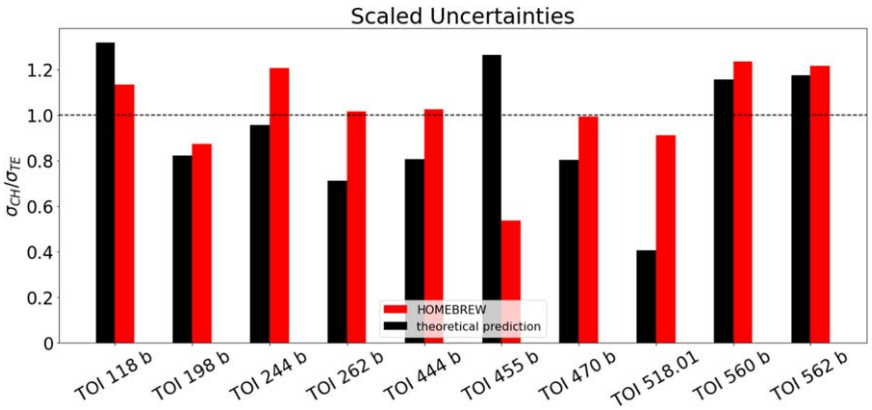

Figure 13. Ratio of depth uncertainties for models using our HOMEBREW method. The black bar for each planet represents our theoretical prediction for the uncertainty ratio, whereas the red bar represents our actual calculated depth uncertainty ratio from CHEOPS models vs. TESS models.

transits with TESS to match the reported precision with our CHEOPS transit for TOI 455 b, where $N_{\rm tr,equiv} = 31.6$. However, given that there is clear evidence of blended light in our light curves for this target, we do not treat this estimate as physical. Rather, this represents further evidence that more careful treatment of contamination is necessary in future studies of this system.

Bonfanti et al. (2021) also report equivalent number of TESS transits by comparing uncertainty in depth for their model fits to TESS data and CHEOPS data. For a V mag $\sim$ 9 star, they report that their precision on one CHEOPS transit with a depth of 500 ppm was equivalent to eight TESS transits, whereas the precision for a CHEOPS transit of depth 250 ppm was equivalent to seven TESS transits, and the precision on a CHEOPS transit of depth 1000 pm was equivalent to two TESS transits. However, given that our analysis differed from theirs in the inclusion of theoretical photon noise limits (i.e., calculation of q), we cannot make a straightforward comparison between our results and theirs.

Finally, Table 12 shows the depth reported by our HOMEBREW joint fits in comparison. We see no trend with transit depth, supporting our prior claim that greater uncertainty in modeling CHEOPS transits may stem from data gaps and nonhomogeneous detrending of CHEOPS light curves, rather than system parameters.

7. Discussion

7.1. Contextualizing these Systems

Here we report physical and orbital properties for each of our planets/planet candidate individually. Our final reported properties are shown in Table 13. We highlight instances of fractional depth uncertainties that are larger than 10%, and discuss these results in context with the TESS and CHEOPS light curves and our fitting methods, where appropriate. Additionally, with the exception of TOI 198, we report predicted masses of these planets using the nonparametric formulation from Ning et al. (2018), who developed R code[40] using the relations therein, which was also translated to the Python package `MRExo`.[41] For planets that are orbiting M dwarfs, we incorporate mass predictions from Kanodia et al. (2019), which is also wrapped into `MRExo`. For classification of planets, we use the framework of Chen & Kipping (2016), who categorized planets as "Terran," "Neptunian," "Jovian," or "Stellar" defined by mass cutoffs at 2 $M_\oplus$, 0.41 $M_{\rm J}$, and 0.08 $M_\odot$, respectively. We report these masses and uncertainties to one decimal place, with the understanding that these are not well-constrained values. In the case of TOI 198 b, our ESPRESSO RVs allowed us an estimation of the planet's mass, so we use this mass estimate when calculating density. Mass and bulk density are important parameters to constrain for all of these planets, as these values help to contextualize formation and evolution for these systems. However, we leave characterization of planet mass to future work, as it is beyond our present scope.

In our reporting of our final parameters for each of these planets/planet candidates we use the HOMEBREW joint fit. This represents a reasonable choice because a joint fit uses all available data, while our HOMEBREW method of fitting was constructed to yield one global set of model parameters. Further, this fit method yielded lowest overall uncertainties.

7.1.1. TOI 118 b

We find that TOI 118 b is a Neptunian world orbiting a Sun-like star on a 6.034-day orbit. We find it has a radius of $4.24 \pm 0.16\ R_\oplus$ and a predicted mass of $8.1^{+12.5}_{-4.8}\ M_\oplus$. TOI 118 b's size places it well above the radius valley, but given the planet's short, $\sim$6-day orbit, it may be experiencing photo-evaporation of its outer atmospheric layers. SPOC characterization of this planet with TESS placed it in a similar part of parameter space on the period–radius diagram, but we improved the radius estimate of this planet by a factor of two relative to its initial uncertainty. Esposito et al. (2019) reported the radius of this planet as $4.71 \pm 0.17\ R_\oplus$, which is discrepant with our radius estimate to $\sim 1.7\sigma$. Interestingly, our joint characterization with HOMEBREW was the only fit method that exhibited a $\geqslant 1\sigma$ discrepancy; our other results for this planet were either larger radius measurements or exhibited larger uncertainties. Further precise photometric characterization is needed to reconcile these deviations for this planet.

We report the lowest fractional depth uncertainty for this target for our joint fit using the HOMEBREW method, and our `pycheops` fit to CHEOPS data and `juliet` to TESS data exhibit similarly low fractional uncertainties in depth. However, we report fractional depth uncertainties at greater than 10% for both the fits to CHEOPS data alone for this target. This may be due to a relatively low in-transit observing efficiency

[40] https://github.com/Bo-Ning/Predicting-exoplanet-mass-and-radius-relationship
[41] https://github.com/shbhuk/mrexo

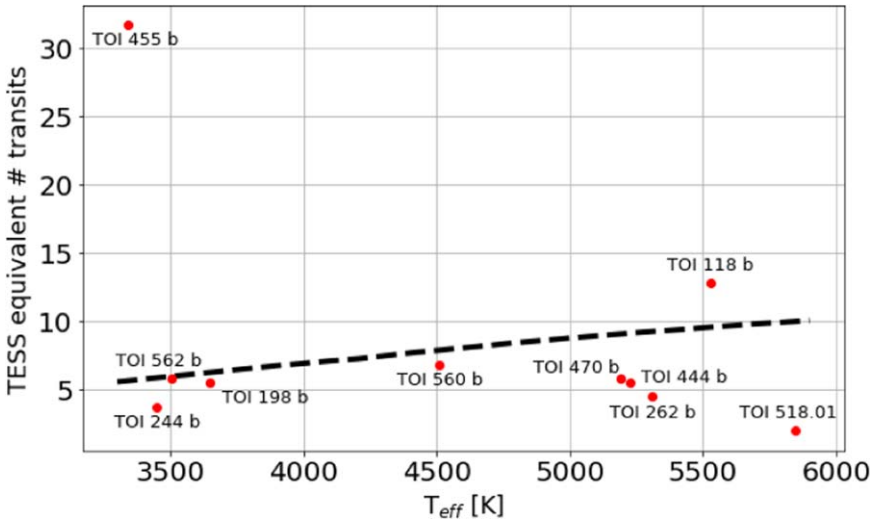

Figure 14. Scatter plot showing equivalent transits vs. stellar effective temperature as calculated with our HOMEBREW joint fits, from Table 12. The dashed line shows our theoretical expectation for the photon ratio q from Equation (4), which is equivalent..

for the CHEOPS visit to this system of 48.8%, where significant gaps in the CHEOPS light curve as a result of Earth occultations of the star may be the cause of the large fractional uncertainty relative.

Errors may have been introduced in joint fitting relative to TESS data alone due to a perceived difference in depth in our `juliet` fit. A perceived difference in transit depth between TESS and CHEOPS may be a result of the slight deviation in bandpass coverage between these two telescopes. The TESS bandpass is optimized for nearby M dwarf stars, whereas CHEOPS has a bluer filter optimized for Sun-like stars. We computed two pairs of limb darkening coefficients for each star for these two bandpasses, but this may not fully account for a discrepancy. Given that a star may appear brighter or dimmer in the TESS bandpass relative to the CHEOPS bandpass, computed transit depths may appear to be different in these bands relative to one another. This may, in part, account for the discrepancy between fits to these light curves. However, as the fractional uncertainty in transit depth for joint fits to both data sets are not statistically different for this target, we cannot meaningfully make the claim that our errors were influenced by this effect. Further, a relatively large fractional depth uncertainty when jointly fitting both data sets is only seen in our `juliet` fit. We report the lowest overall fractional depth uncertainty for this target for our HOMEBREW joint fit.

7.1.2. TOI 198 b

We find that TOI 198 b is a Terran world orbiting an early M dwarf star on a 10.215-day orbit. We find it has a radius of 1.44 ± 0.08 $R_\oplus$ and a mass from our ESPRESSO RVs of 4.0 ± 1.1 $M_\oplus$, making its likely mean density 7.3 g cm^{-3}. This size and density indicate that this planet is likely a dense super-Earth. Using the nonparametric mass from above, we predict its mass as $1.3^{+6.0}_{-1.0}$ $M_\oplus$, which encompasses the measurement from our ESPRESSO RVs.

Given TOI 198 b's radius and orbital period, it sits just below the radius valley, as shown in Figure 17. This density and position in period–radius space would indicate that this planet is likely a bare rock that either never formed with a gaseous envelope or lost such an envelope quickly after formation. Interestingly, initial characterization of this planet with TESS PM photometry upon discovery could not resolve whether it was in the gap or not, but our revised radius estimate places it more precisely.

The fractional depth uncertainty for TOI 198 b fitted with TESS data alone is above 10% for fits with our HOMEBREW method and with `juliet`, whereas the fractional uncertainty with CHEOPS data alone is below this threshold for our HOMEBREW fit but not our `juliet` fit, with the fractional uncertainty in the joint data set being lower still in both cases. This relatively large uncertainty in the fit to TESS data may have been a result of noise in the light curve, which had a MAD after detrending of 1649 ppm across both sectors, but a higher MAD of 1901 ppm in the EM1 sector for this star. We calculated a transit depth of ∼1000 ppm for this planet, meaning that the scatter in the light curve was approximately twice as large in magnitude as the transit signal itself. Therefore, it is sensible that fits to TESS data alone would yield larger uncertainties for this target, given that the noise in CHEOPS photometry was 522 ppm after detrending, representing a significant reduction in noise. Further, only four transits were captured in TESS data, potentially leading to an increase in uncertainty given the low number of transits. Finally, this relatively large uncertainty in our model fit may have been a result of a degeneracy between transit depth and impact parameter, particularly for the `juliet` fit to the TESS photometry, where orbital parameters were computed separately from those computed for fits to the CHEOPS light curve. A high-impact parameter would indicate that the planet is transiting away from the stellar midline, which would would inflate the planet-to-star radius ratio for a constant transit depth. In particular, our `juliet` fit yields a higher-impact parameter for TESS photometry relative to the fit to CHEOPS photometry, potentially accounting for this higher uncertainty in transit depth.

7.1.3. TOI 244 b

Similar to TOI 198 b, we find that TOI 244 b is a Terran world orbiting an M dwarf star, with an orbital period of 7.397 days. We find it has a radius of 1.03 ± 0.08 $R_\oplus$ and a predicted mass of $0.8^{+2.0}_{-0.6}$ $M_\oplus$. We report the predicted mass of TOI 244 b using the nonparametric function for M dwarf exoplanets from

Table 13
Final Fitted Physical and Orbital Parameters for all Systems, from HOMEBREW Joint Fits

Parameter	Unit	TOI 118 b	TOI 198 b	TOI 244 b	TOI 262 b	TOI 444 b
Stellar Parameters:						
CHEOPS limb darkening	c_1	0.695	0.657	0.762	0.706	0.716
CHEOPS limb darkening	c_2	0.826	0.591	0.539	0.852	0.848
TESS limb darkening	c_1	0.627	0.700	0.712	0.637	0.651
TESS limb darkening	c_2	0.722	0.685	0.468	0.746	0.746
Stellar radius	R_s ($R_\odot$)	1.03 ± 0.03	0.441 ± 0.019	0.399 ± 0.019	0.853 ± 0.021	0.779 ± 0.053
Stellar mass	M_s ($M_\odot$)	0.92 ± 0.03	0.467 ± 0.023	0.424 ± 0.021	0.913 ± 0.029	0.96 ± 0.13
Effective temperature	$T_{\rm eff}$ (K)	5527 ± 65	3650 ± 75	3450 ± 75	5310 ± 124	5225 ± 70
Orbital and Transit Parameters						
Orbital period	days	$6.04345 \pm 1e\text{-}5$	$10.2152 \pm 6e\text{-}5$	$7.39726 \pm 2e\text{-}5$	$11.14529 \pm 3e\text{-}5$	$17.96360 \pm 4e\text{-}5$
Time of mid-transit	BTJD	2083.5109 ± 0.0011	2480.048 ± 0.0004	2489.1482 ± 0.0025	2136.5766 ± 0.0010	2190.0391 ± 0.0008
Scaled radius	$\frac{Rp}{Rs}$	0.0376 ± 0.0009	0.0299 ± 0.0022	0.0278 ± 0.0017	0.0220 ± 0.0015	0.0325 ± 0.0007
Scaled semimajor axis	$\frac{a}{Rs}$	21.747 ± 2.023	49.086 ± 3.003	39.663 ± 7.539	41.211 ± 8.024	36.768 ± 2.283
Inclination angle	i(deg)	88.938 ± 0.505	89.890 ± 0.102	89.206 ± 0.657	89.011 ± 0.413	89.647 ± 0.314
Transit duration	$T_{\rm dur}$ (hr)	2.028 ± 0.194	1.631 ± 0.155	1.233 ± 0.118	1.501 ± 0.143	3.761 ± 0.356
Physical Planet Parameters:						
Impact parameter		0.402 ± 0.193	0.094 ± 0.086	0.554 ± 0.494	0.719 ± 0.328	0.225 ± 0.193
Semimajor axis	a (au)	0.104 ± 0.005	0.100 ± 0.006	0.073 ± 0.003	0.163 ± 0.002	0.133 ± 0.006
Radius	R_p ($R_\oplus$)	4.24 ± 0.16	1.44 ± 0.08	1.03 ± 0.08	2.07 ± 0.15	2.77 ± 0.20
Predicted mass	M_p ($M_\oplus$)	$8.1^{+12.5}_{-4.8}$	4.0 ± 1.1[a]	$0.8^{+2.0}_{-0.6}$	$5.5^{+7.9}_{-3.2}$	$6.6^{+9.3}_{-3.8}$
Equilibrium temperature	$T_{\rm eq}$ (K)	838 ± 40	368 ± 26	387 ± 30	584 ± 45	609 ± 61
Parameter	Unit	TOI 455 b	TOI 470 b	TOI 518.01	TOI 560 b	TOI 562 b
Stellar Parameters:						
CHEOPS limb darkening	c_1	0.824	0.709	0.705	0.733	0.751
CHEOPS limb darkening	c_2	0.484	0.778	0.745	0.881	0.578
TESS limb darkening	c_1	0.778	0.635	0.626	0.675	0.707
TESS limb darkening	c_2	0.415	0.689	0.658	0.771	0.499
Stellar radius	R_s ($R_\odot$)	0.265 ± 0.011	0.831 ± 0.021	1.027 ± 0.025	0.65 ± 0.02	0.337 ± 0.015
Stellar mass	M_s($M_\odot$)	0.257 ± 0.014	0.87 ± 0.09	1.07 ± 0.06	0.73 ± 0.02	0.342 ± 0.011
Effective temperature	$T_{\rm eff}$ (K)	3340 ± 150	5190 ± 90	5845 ± 70	4511 ± 110	3505 ± 51
Orbital and Transit Parameters						
Orbital period	days	$5.35876 \pm 1e\text{-}5$	$12.19148 \pm 3e\text{-}5$	$17.87712 \pm 7e\text{-}5$	$6.39805 \pm 1e\text{-}5$	$3.93060 \pm 2e\text{-}6$
Time of mid-transit	BTJD	2152.2189 ± 0.0005	2205.9825 ± 0.0011	2568.4107 ± 0.0014	2240.6702 ± 0.0007	2272.6757 ± 0.0004
Scaled radius	$\frac{Rp}{Rs}$	0.0408 ± 0.0010	0.0477 ± 0.0008	0.0246 ± 0.0013	0.0350 ± 0.0007	0.0309 ± 0.0010
Scaled semimajor axis	$\frac{a}{Rs}$	29.963 ± 3.128	30.917 ± 2.369	47.733 ± 4.451	23.743 ± 3.338	22.890 ± 1.211
Inclination angle	i (deg)	89.203 ± 0.658	89.527 ± 0.432	89.723 ± 0.226	89.428 ± 0.441	89.228 ± 0.483
Transit duration	$T_{\rm dur}$ (hr)	1.392 ± 0.133	3.063 ± 0.292	2.844 ± 0.228	2.069 ± 0.197	1.291 ± 0.123
Physical Planet Parameters:						
Impact parameter		0.840 ± 0.222	0.253 ± 0.216	0.249 ± 0.169	0.248 ± 0.171	0.307 ± 0.160
Semimajor axis	a (au)	0.022 ± 0.003	0.119 ± 0.008	0.227 ± 0.002	0.072 ± 0.002	0.036 ± 0.0004
Radius	R_p ($R_\oplus$)	1.18 ± 0.06	4.34 ± 0.29	2.77 ± 0.16	2.49 ± 0.10	1.20 ± 0.06
Predicted mass	M_p ($M_\oplus$)	$0.9^{+1.7}_{-0.5}$	$8.4^{+7.5}_{-5.6}$	$6.7^{+7.3}_{-4.3}$	$5.7^{+8.3}_{-3.3}$	$0.8^{+2.5}_{-0.5}$
Equilibrium temperature	$T_{\rm eq}$ (K)	555 ± 48	660 ± 70	598 ± 55	655 ± 41	518 ± 44

Note.
[a] Derived from the Keplerian fit to our ESPRESSO RVs.

Kanodia et al. (2019), which predicts smaller masses for small planets compared with the Kepler sample, which is composed of primarily Sun-like stars. Previous studies indicate that even when accounting for observational biases of the Kepler mission, M dwarfs typically yield more small planets compared with FGK stars and fewer giant planets (Mulders et al. 2015). The planet's short period may indicate that photoevaporation may have played a significant role in stripping the planet of a gaseous envelope, if it ever accreted one. Further precise characterization of this planet, particularly with extreme-precision RVs (EPRVs), may illuminate its properties, and thus its formation and evolutionary history, in greater detail. Initial estimation of this planet's radius with TESS PM photometry was imprecise, and determination of its position

relative to the radius valley was not originally possible. Our period and radius estimates place this planet squarely below the radius valley in the Earth-sized regime. This represents an interesting system that includes an Earth-sized planet in a close orbit around an M dwarf star.

We note that the fractional uncertainty in two CHEOPS visits to TOI 244 b was larger than 10% for all three fitting methods. This may be due to the relatively high level of noise in our CHEOPS light curves for this target, as shown in Figure 10. When fitting CHEOPS photometry with our HOMEBREW method, the fractional depth uncertainty is larger than the fractional uncertainty in the fit to TESS data alone. In the case of fitting our TESS and CHEOPS data sets independently with `juliet`, the fractional depth estimates are greater than 10%. In the case of `juliet`, jointly fitting both photometric data sets results in lower than 10% fractional uncertainty, representing an improvement, but this threshold is not met by our joint fit for the HOMEBREW method. This may have been a result of the gaps in both of our CHEOPS visits, which are due to Earth occultations. A significant gap in CHEOPS coverage during our first visit occurred near the midpoint of the transit, which may have made the bottom of the transit difficult to identify. Further, a significant gap in CHEOPS coverage occurred during our second visit during the transit egress, which could have obscured the general shape of the transit and increased the uncertainty. These gaps may have contributed to an overall degeneracy between planet size and impact parameter, increasing model uncertainties for both quantities. It is also notable that our CHEOPS light curves exhibited high noise on timescales that are relevant to characterization of transits, as shown in Figure 10. Further, noise in the TESS light curve, which had a MAD of 2146 ppm across both sectors, may have contributed to a relatively large fractional uncertainty in this case, given that the calculated transit depth was smaller by a factor of two, which is similar to the case of TOI 198 b. However, it seems that this uncertainty was slightly more constrained during model fitting to both data sets jointly for both fitting methods.

7.1.4. TOI 262 b

We find that TOI 262 b is a Neptunian world orbiting a Sun-like star with an orbital period of 11.145 days. We find it has a physical size of $2.07 \pm 0.15\ R_\oplus$ and a predicted mass of $5.5^{+7.9}_{-3.2}\ M_\oplus$. Similar to TOI 244 b, the position of this planet was not well constrained with TESS PM photometry, as it could have been either a sub-Neptune, a super-Earth, or a planet in the radius valley. TOI 262 b represents an interesting case that closely borders—or perhaps falls into—the radius valley. While our models do not conclusively place this planet outside of the radius valley, we are able to more tightly constrain its radius compared with prior estimates.

We report a fractional depth uncertainty of 10% or larger for all fits to TOI 262 photometry, regardless of data set or fit method (where our joint fit to both data sets with `juliet` yields a fractional depth of uncertainty of precisely 10%). When calculating fractional uncertainties, a shallower transit with a similar uncertainty to a deeper one will yield a relatively larger fractional uncertainty. As shown by our calculated transit depths in Table 11, our models vary around ∼500–600 ppm for this target. As such, our model uncertainties, which are otherwise comparable in magnitude to those for other systems, mean that the fractional uncertainty is slightly inflated for this target.

Further, the noise in the TESS light curve was relatively low at MAD ∼ 400 ppm, and the noise in the detrended CHEOPS light curve was lower than this by a factor of two. These are indicative of light curves with low amounts of scatter, and we might expect for our models to be very well constrained. Additionally, our light curves in and out of transit are well sampled, and systematics appear to be well constrained given the apparent flatness of the light curves, further giving credence to the notion that we may have expected our models to be well behaved. However, for all of our models, our comparatively large uncertainties arose from degeneracy between transit depth and impact parameter. For all of our models, we report an impact parameter $b \geqslant 0.7$, with large uncertainties in both $\frac{a}{R_*}$ and inclination angle. A high-impact parameter would indicate the planet is transiting toward the edge of the stellar disk. Even though we hold limb darkening coefficients constant, the prospect of transiting away from the stellar midline introduces more error in our models, thus contributing to the larger-than-expected uncertainties in depth.

7.1.5. TOI 444 b

We find that TOI 444 b is a Neptunian world orbiting a K dwarf star on a 17.964 days orbit. We find it has a radius of $2.77 \pm 0.20\ R_\oplus$ and a predicted mass of $6.6^{+9.3}_{-3.8}\ M_\oplus$. Our characterization of the planet's period and radius place it firmly in the sub-Neptune regime. Our findings match previous findings from SPOC PM sector models, which initially constrained this planet to the sub-Neptune regime.

While all of our fits with the HOMEBREW method yield relatively small fractional depth uncertainties, our fit to the TESS light curves with `juliet` yield a fractional depth uncertainty greater than 10%. Our joint fit and CHEOPS fit with `juliet` yield similarly small uncertainties as our HOMEBREW method, making the aforementioned `juliet` fit to TESS data somewhat anomalously large. This may be a result of the way in which `juliet` handles orbital parameters separately for our individual fits. Specifically, because we compute one set of orbital parameters but different transit depths for our HOMEBREW fits, our errors on these calculated depths are propagated in the same way for both data sets. This is not true for our individual fits with `juliet`, which may have been the cause of such a large uncertainty in depth for our TESS fit for this target. As shown in Table 13, the impact parameter for our joint HOMEBREW fit is relatively low. However, for our `juliet` fit to TESS data for this target, the calculated impact parameter was significantly larger and carried a larger uncertainty. Given the aforementioned degeneracy between transit depth and impact parameter, this may have contributed to a larger uncertainty on transit depth for this particular fit.

7.1.6. TOI 455 b

We find that TOI 455 b is a Terran world orbiting an M dwarf star on a 5.359-day orbit. We find it has a radius of $1.18 \pm 0.06\ R_\oplus$ and a predicted mass of $0.9^{+1.7}_{-0.5}\ M_\oplus$.

Our results yield no large fractional depth uncertainties above the 10% threshold, indicating our results were well constrained. However, as previously mentioned, our radius measurements are discrepant from one another in many cases

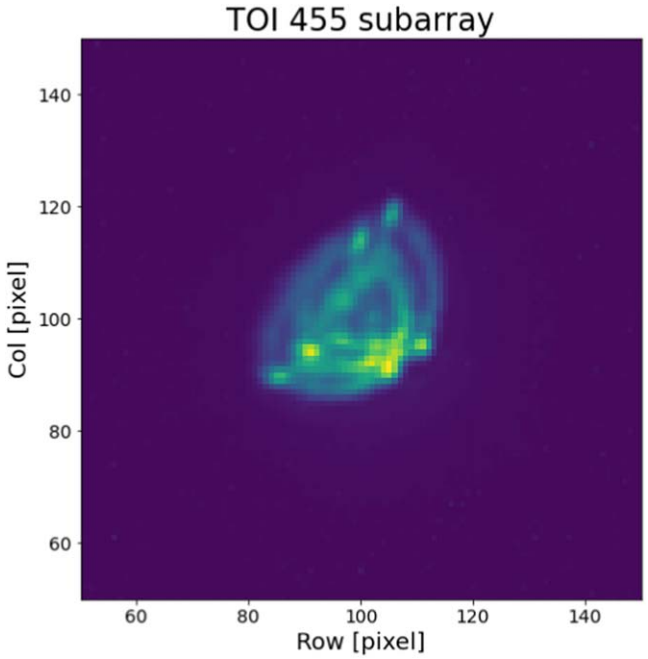

Figure 15. One zoomed-in frame from the CHEOPS subarray for TOI 455 (TIC 98796344), which clearly shows two sources in the center of the image.

for this planet. Interestingly, this planet has been found to be orbiting an M dwarf that is part of a hierarchical triple system (Winters et al. 2019, 2022). Therefore, it is likely that the transits we detect have been severely contaminated by light from its partner stars, as shown by Figure 15. Because we were not able to use `PIPE` to satisfactorily disentangle the strongly confused nearby companion from TOI 455, we instead analyzed the aperture integrated signal of both components as provided by the DRP. We detrended our CHEOPS and TESS light curves as specified in Section 5, but our discrepant radius measurements may mean that our detrending contributed to these deviations. Whereas we subtracted and corrected for background flux in the aperture in our CHEOPS detrending, we merely flattened the TESS light curve, which accounted for short-term variations in flux due to stellar eclipses. This could have led the transits in the TESS light curve to appear systematically deeper as compared with CHEOPS. This differing treatment may have led to an overestimation of the planet radius when examining TESS photometry and an underestimation of the planet radius when examining CHEOPS photometry.

Indeed, Winters et al. (2019) reported a radius of this planet of $1.38^{+0.13}_{-0.12}$ $R_\oplus$ and Winters et al. (2022) later constrained the radius to 1.30 ± 0.06 $R_\oplus$, both of which are consistent with our final reported value, which uses both data sets. However, these estimates are not consistent with our estimates using TESS or CHEOPS alone, which are systematically too high or too low, respectively. It is apparent that while our models that fit TESS data or CHEOPS data separately match each individual data set well, our joint models fall between these data sets, suggesting the final value is influenced by both data sets nearly equally.

We believe this represents a cautionary tale. We believe it is beyond the scope of this work to systematically account for contamination from nearby sources in both TESS and CHEOPS bandpasses, as it was our goal to demonstrate the effects of base-level detrending. However, we believe that fully accounting for contamination from nearby stars is warranted, as it may have helped assuage deviations in transit depth in this case.

7.1.7. TOI 470 b

We find that TOI 470 b is a Neptunian world orbiting a late G dwarf on a 12.191-day orbit. We report that it has a radius of 4.34 ± 0.29 $R_\oplus$ and a predicted mass of $8.4^{+7.5}_{-5.6}$ $M_\oplus$. This size supports the claim that this planet is an ice giant world that has held on to its gaseous envelope and may be composed of as much as 2% H_2 by mass (Zeng et al. 2019). However, further precise characterization with EPRVs of this planet will illuminate its properties.

We report no models that have a fractional depth uncertainty greater than 10%. Our single CHEOPS visit for the target missed the transit ingress, and as such as we report an in-transit observing efficiency of only 70%. This means we did not have a baseline for the flux prior to the beginning of the transit, which may have contributed to some uncertainty regarding the true depth of the planet. However, it seems our models did not significantly suffer from this lack of pre-transit baseline. This may have been aided by the fact that there was a very low amount of noise in the CHEOPS light curve, which had a MAD of 557 ppm after detrending.

7.1.8. TOI 518.01

TOI 518.01 is the only system that we were not able to validate as a planet. As such, we treat conclusions drawn for this system with more caution, as these results will clearly depend on whether the system is later validated. Should these signals be validated, we find that TOI 518.01 may be a Neptunian world orbiting an early G dwarf star on a 17.877-day orbit. We report a potential radius of 2.77 ± 0.16 $R_\oplus$ and a predicted mass of $6.7^{+7.3}_{-4.3}$ $M_\oplus$. Given the size estimate for this candidate planet, this would be a world that has retained its gaseous envelope and it sits well above the radius valley.

The model fit to TESS data alone for TOI 518.01 yielded the largest fractional depth uncertainty for our HOMEBREW method. The fractional depth uncertainties for HOMEBREW fits to CHEOPS and both data sets jointly on this target were 14.2% and 10.5%, respectively, but the fractional uncertainty in the depth for TESS data alone was 21.2%, which also represented the largest overall fractional depth uncertainty for any fit method or data set combination. This may be because this was the only TOI for which we were able to use only one TESS sector, given that our attempts to salvage the EM sector (contaminated with stray light) for TOI 518 were unsuccessful. Therefore, we were only fitting photometry that included two transits in a light curve that had a noise level of MAD $\approx$1000 ppm, which is larger than the transit depth.

Additionally, relatively large uncertainties in fits to our two CHEOPS visits may be due to important data gaps while the planet was in transit, which may obscure the true shape of the transit and thus contribute to a larger uncertainty. These data gaps obscured crucial parts of our two transits, including transit ingress and parts of the bottom of the transit.

7.1.9. TOI 560 b

We find that TOI 560 b is a Neptunian planet orbiting a K dwarf star on a 6.398-day orbit. It has a radius of 2.49 ± 0.10

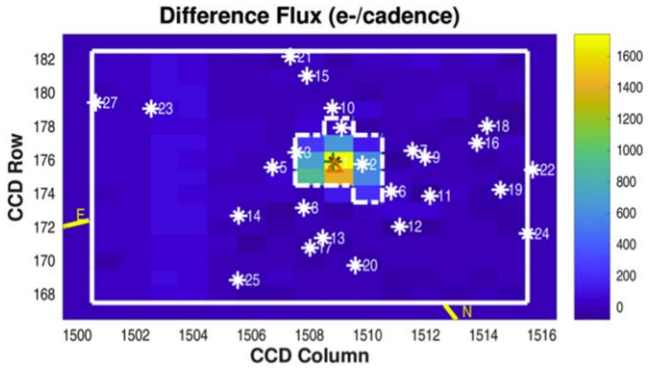

Figure 16. Star field around TOI 560 (TIC 101011575) from the SPOC report for PM sector eight for this star. There are seven TIC entries within 60.″0 of TOI 560, which may be evidence of possible contamination from nearby field stars, which would dilute the transits in the TESS light curves.

$R_\oplus$ and a predicted mass of $5.7^{+8.3}_{-3.3}$ $M_\oplus$. This planet's radius places it above the radius valley, meaning it has held on to its gaseous envelope and likely a rocky core enveloped by a thick H/He atmosphere, despite a relatively short orbital period.

Our final reported radius measurement is not consistent with the radius measurement of 2.79 ± 0.10 $R_\oplus$ from Barragán et al. (2022). Interestingly, our models fitted to the CHEOPS light curve are indicative of deeper transits relative to models fitted to TESS light curves. We compute a planet radius of 2.72 ± 0.11 $R_\oplus$ with our HOMEBREW method from CHEOPS photometry, but we compute a planet radius of 2.38 ± 0.10 $R_\oplus$ with our HOMEBREW method from TESS photometry. Consequentially, these radius estimates are not consistent with one another, and only the radius estimate from our fit to CHEOPS data is consistent with that from Barragán et al. (2022).

In a similar vein to our discussion for TOI 455 b, this possible discrepancy in radius may be a result of contamination in the TESS aperture for this star. Figure 16, which was produced as part of a SPOC report for this planet from sector eight PM photometry, shows the star field around TOI 560. There are seven TIC entries within 60.″0, one of which is TIC 101011568, which has a Tmag of 11.79. This indicates that there may be flux from other stars present in the light curve for this target, which would dilute any transit signals therein. This in turn would make a planet appear smaller than if this contamination were not present, which may be the case for this system. Indeed, as previously stated, we merely flattened our TESS light curves to account for astrophysical noise rather than fully correcting for possible sources of contamination.

7.1.10. TOI 562 b

We find that TOI 562 b is a Terran world orbiting an M dwarf star on a 3.931-day period. We report that it has a radius of 1.20 ± 0.06 $R_\oplus$ and a predicted mass of $0.8^{+2.5}_{-0.5}$ $M_\oplus$. Given these physical parameters, we find that this planet is likely a super-Earth with a high silicon-to-iron ratio, although with no mass estimate, we cannot say for sure. Our radius measurement is consistent with the reported radius measurement from Luque et al. (2019) of $1.217^{+0.084}_{-0.083}$ $R_\oplus$. Based on the fact that none of our models for this target had fractional depth uncertainties above the 10% threshold, and that the largest fractional depth uncertainty for any fit was our `juliet` fit to CHEOPS data at 6.8%, our model parameters are well constrained for this planet.

7.2. Position Relative to the Radius Valley

We have improved radius estimates for these TOIs by jointly fitting TESS and CHEOPS photometry, allowing us to more effectively place them in period–radius space. As noted in Zhu & Dong (2021), the location of the valley decreases with orbital period and increases with host mass. These authors report the location of the valley as a function of scaled radius, which is a double power law of the following form:

$$\tilde{R}_p(P, M_*) = R_p\left(\frac{P}{10 \text{ days}}\right)^{-g}\left(\frac{M_*}{M_\odot}\right)^{-h}, \quad (10)$$

where $\tilde{R}_p$ is the rescaled radius of the planet, and g and h represent power-law coefficients for the gap location according to orbital period and host stellar-mass, respectively. Similar to Zhu & Dong (2021), we choose $g = -0.09$ (Van Eylen et al. 2018) and $h = 0.26$ (Berger et al. 2020).

Figure 17 shows our period-scaled radius diagram, which includes confirmed planets from the California-Kepler survey (CKS) sample. In this figure, our final joint HOMEBREW fits are overplotted as red stars, with our HOMEBREW fits to TESS data only plotted as blue stars. We also include the gap as a light blue shaded region from $R_{p,0} = 1.9 \pm 0.2$ $R_\oplus$. We note that the location of the radius valley with respect to the variables in Equation (10) has important implications for distinguishing between different planet formation and evolution models, and do not claim that the values we chose are definitive. Rather, we chose these values to illuminate the positions of the planets in our sample with respect to the valley.

Two of the planets we present in this work may fall into the radius gap according to the functional form we present here. Upon comparison of our uncertainties in planet radii relative to our TESS-only fits, we see that our uncertainties are smaller, which corresponds to fewer planets potentially falling into the gap. With a relatively small sample of 10 planets/planet candidate, we do not claim to resolve the valley, but rather seek to add to the sample of small planets that are characterized with high precision. Improving the precision with which we place these planets and other small planets in period–radius space will inform theories of small planet formation and evolution (see Section 1), and this work had added a valuable contribution to the overall small planet sample.

8. Summary and Conclusion

In this work, we have presented our characterization of 10 small planets via observations with both TESS and CHEOPS. We vetted and validated transit signals as being planetary in nature for planets that had not yet been published, including TOI 198 b, TOI 244 b, TOI 444 b, and TOI 470 b, although we could not conclusively validate transit signals for TOI 518.01. To this end, we introduced and analyzed follow-up observations of these systems to verify that these stars do not have previously unseen companions, and that the transit signals we analyze are due to transiting planets on the target star. We detrended our TESS and CHEOPS light curves from sources of instrumental and astrophysical noise. We fitted transit models to these light curves three different ways to check consistency between our fits.

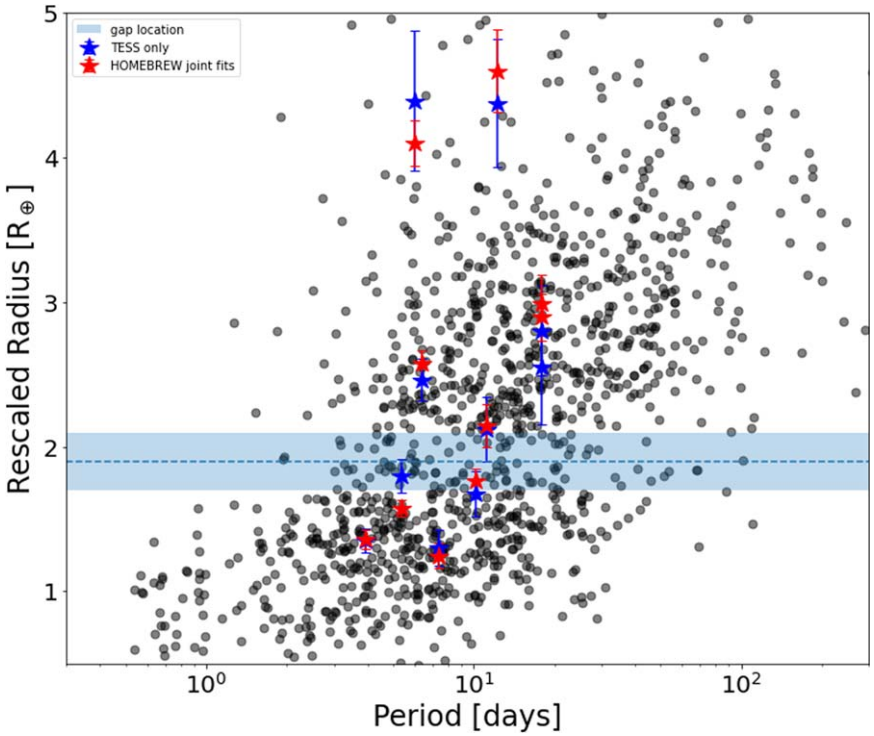

Figure 17. Period-scaled radius diagram for the California-Kepler survey (CKS) sample of planets (black circles; Petigura et al. 2022), with initial estimates from our fits to TESS data only (blue stars) and our HOMEBREW joint fit results overlaid (red stars). All radii have been rescaled according to Equation (10), clearly exhibiting a deficiency of planets around 2 $R_\oplus$.

We summarize our results and findings below:

1. We report updated physical and orbital properties for 10 planets, including four Terran worlds and six Neptunian worlds.
   (a) We find that TOI 118 b is a Neptunian world orbiting a Sun-like star on a 6.034-day orbit, and that it has a radius of 4.24 ± 0.16 $R_\oplus$. Our fits for this system may have yielded slightly higher fractional depth uncertainties due to deviations in perceived transit depth between different filters.
   (b) We find that TOI 198 b is a Terran world orbiting an M dwarf star on a 10.215-day orbit, and that it has a radius of 1.44 ± 0.08 $R_\oplus$. While most fits for this target were well constrained, fits to the TESS light curve for this target might have suffered from relatively high photon noise.
   (c) We find that TOI 244 b is a Terran world orbiting an M dwarf star on a 7.397-day orbit, and that it has a radius of 1.03 ± 0.08 $R_\oplus$. Our fits to CHEOPS photometry for this target may have been affected by data gaps that obscured crucial parts of our transits.
   (d) We find that TOI 262 b is a Neptunian world orbiting a Sun-like star on a 11.145-day orbit, and that it has a radius of 2.07 ± 0.15 $R_\oplus$. We report a fractional depth uncertainty of 10% or larger for almost all fits to TOI 262 photometry. This may have been due to either a comparatively shallow computed transit depth or a degeneracy between transit depth and impact parameter.
   (e) We find that TOI 444 b is a Neptunian world orbiting a Sun-like star on a 17.964-day orbit, and that it has a radius of 2.77 ± 0.20 $R_\oplus$. The fractional depth uncertainty for the `juliet` fit to TESS photometry was anomalously large, perhaps because orbital parameters are computed separately for `juliet` fit, leading to a degeneracy between transit depth and impact parameter in this case.
   (f) We find that TOI 455 b is a Terran world orbiting an M dwarf star on a 5.359-day orbit, and that it has a radius of 1.18 ± 0.06 $R_\oplus$. Different detrending methods for our CHEOPS and TESS light curves may have led to different transit depths as seen by these telescopes, and may have contributed to an inflation of model uncertainties when fitting TESS data relative to model uncertainties when fitting CHEOPS data.
   (g) We find that TOI 470 b is a Neptunian world orbiting a Sun-like star on a 12.191-day orbit, and that it has a radius of 4.34 ± 0.29 $R_\oplus$. Despite not having an out-of-transit baseline prior to the transit in the CHEOPS visit for this target, our models for this planet were well constrained.
   (h) We find that TOI 518.01 may be a Neptunian world orbiting a Sun-like star on a 17.877-day orbit, with a potential radius of 2.77 ± 0.16 $R_\oplus$. Our models for this system yielded the largest fractional depth uncertainties relative to any other system, perhaps due to data gaps in our CHEOPS transits and photon noise in our TESS light curves.
   (i) We find that TOI 560 b is a Neptunian world orbiting a Sun-like star on a 6.398-day orbit, and that it has a radius of 2.49 ± 0.10 $R_\oplus$. A possible discrepancy between our fits to TESS photometry and the radius valley reported by Barragán et al. (2022) may have

been the result of contamination from nearby field stars in the TESS aperture for this star.

(j) We find that TOI 562 b is a Neptunian world orbiting an M dwarf star on a 3.931-day orbit, and that it has a radius of 1.20 ± 0.06 $R_{\oplus}$. Our models were well constrained for this target, and matched well with previously published values.

2. We improved radius estimates with all fitting methods relative to initial characterization with TESS PM estimates. We report radius measurements to better than 10% precision for all 10 of our planets/candidate planet, even when wrapping in uncertainties in stellar parameters. This shows that high-precision results can be obtained from analysis of photometry alone, although our results would be improved by further high-precision characterization of the host stars. Further, interesting information regarding these systems' formation and evolutionary histories could be gained from mass measurements via spectroscopic observations.
3. We compared relative photometric performances of TESS and CHEOPS, finding that our models fitted to CHEOPS photometry under-performed relative to our predictions in most cases, as indicated by the fact that we needed fewer TESS transits than we obtained to match depth precision on CHEOPS transits. We believe that finding is due to two primary reasons, including (1) important data gaps in CHEOPS visits, and (2) the way in which both CHEOPS and TESS light curves are generated and detrended. There is no standard method with which to detrend CHEOPS photometry, whereas TESS light curves are all processed by the same pipeline, which treats the data uniformly. Regardless, when we compare precision from one CHEOPS transit, our results indicate that precision of our CHEOPS observations are equivalent to between two and 12 TESS transits, excluding TOI 455 b as anomalous.
4. Finally, we were able to place these planets precisely in period–radius space. Two of the planets from our sample may fall into the gap, or immediately border it. With a relatively small sample of 10 planets, we do not claim to resolve the valley, but rather seek to add to the sample of small planets that are characterized with high precision. Improving the precision with which we place these planets and other small planets in period–radius space will inform theories of small planet formation and evolution (see Section 1), and this work has added a valuable contribution to the overall small planet sample.

We graciously thank the anonymous referee and data editor, who both provided valuable feedback on this publication.

D.D. acknowledges support from the TESS Guest Investigator Program grants 80NSSC21K0108 and 80NSSC22K0185.

We acknowledge contributions from Thomas G. Wilson, Andrea Fortier, and other members of the CHEOPS GTO team, regarding estimation of noise in CHEOPS light curves and comparisons to other systems observed by CHEOPS.

This paper includes data collected by the TESS mission. Funding for the TESS mission is provided by NASA's Science Mission Directorate.

We acknowledge the use of public TESS data from pipelines at the TESS Science Office and at the TESS Science Processing Operations Center. Resources supporting this work were provided by the NASA High-End Computing (HEC) Program through the NASA Advanced Supercomputing (NAS) Division at Ames Research Center for the production of the SPOC data products.

Some/all of the data presented in this paper were obtained from the Mikulski Archive for Space Telescopes (MAST) at the Space Telescope Science Institute. The specific observations analyzed can be accessed via doi:10.17909/dshz-jz09 .

This work makes use of observations from the LCOGT network. Part of the LCOGT telescope time was granted by NOIRLab through the Mid-Scale Innovations Program (MSIP). MSIP is funded by NSF.

This research has made use of the NASA Exoplanet Archive, which is operated by the California Institute of Technology, under contract with the National Aeronautics and Space Administration under the Exoplanet Exploration Program.

This research made use of Lightkurve, a Python package for Kepler and TESS data analysis (Lightkurve Collaboration et al. 2018).

Some of the observations in the paper made use of the High-Resolution Imaging instruments 'Alopeke and Zorro obtained under Gemini LLP Proposal Number: GN/S-2021A-LP-105. 'Alopeke and Zorro were funded by the NASA Exoplanet Exploration Program and built at the NASA Ames Research Center by Steve B. Howell, Nic Scott, Elliott P. Horch, and Emmett Quigley. 'Alopeke (Zorro) was mounted on the Gemini North (South) telescope of the international Gemini Observatory, a program of NSF's OIR Lab, which is managed by the Association of Universities for Research in Astronomy (AURA) under a cooperative agreement with the National Science Foundation on behalf of the Gemini partnership: the National Science Foundation (United States), National Research Council (Canada), Agencia Nacional de Investigación y Desarrollo (Chile), Ministerio de Ciencia, Tecnologóa e Innovación (Argentina), Ministério da Ciência, Tecnologia, Inovações e Comunicações (Brazil), and Korea Astronomy and Space Science Institute (Republic of Korea).

Facilities: TESS, CHEOPS, LCOGT, VLT-ESPRESSO, CTIO/SMARTS-CHIRON, FLWO-TRES, Gemini-'Alopeke/Zorro, Keck2-NIRC2, Palomar-PHARO, SOAR-HRCam.

Software: AstroImageJ (Collins et al. 2017), astropy (Astropy Collaboration et al. 2013, 2018, 2022), numpy (Harris et al. 2020), matplotlib (Hunter 2007), lightkurve (Lightkurve Collaboration et al. 2018), pycheops (Maxted et al. 2022), PyLDTK (Parviainen & Aigrain 2015), juliet (Espinoza et al. 2019), emcee (Foreman-Mackey et al. 2013), batman (Kreidberg 2015), corner (Foreman-Mackey 2016), MRExo (Kanodia et al. 2019), TAPIR (Jensen 2013).

Appendix A
TESS Light Curves

In this Appendix, we show the TESS light curves used in our analysis (e.g., Figure 18). The gray points show the PDCSAP flux, and the red line in each panel shows the detrending trend line.

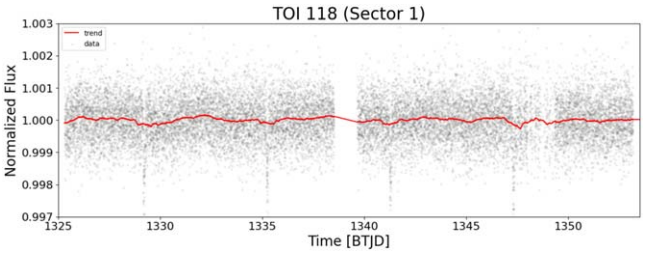

Figure 18. TESS light curves (LCs) for our 10 TOIs. The complete figure set (19 figures) is available in the online journal.

(The complete figure set (19 images) is available.)

Appendix B
CHEOPS Light Curves

In this appendix, we show our *CHEOPS* light curves (e.g., Figure 19). For each of our systems, we show both the raw flux and detrended flux.

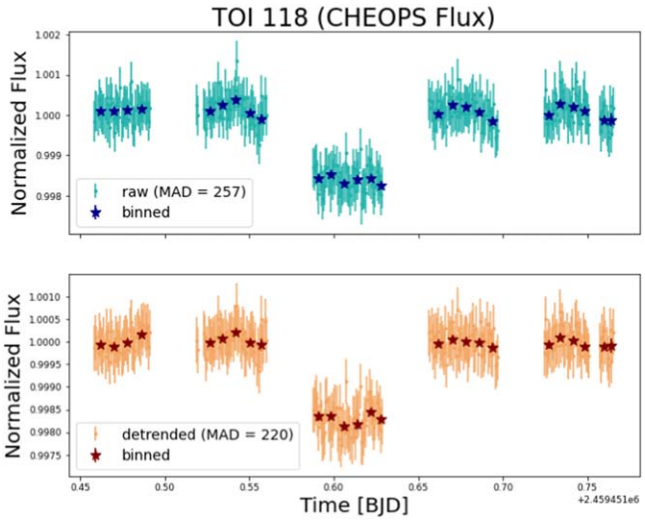

Figure 19. CHEOPS LCs for our targets. The complete figure set (12 figures) is available in the online journal.

(The complete figure set (12 images) is available.)

Appendix C
SED Analysis

In this Appendix, we show our SED fits to stars which are hosts to newly-validated planets (Figure 20).

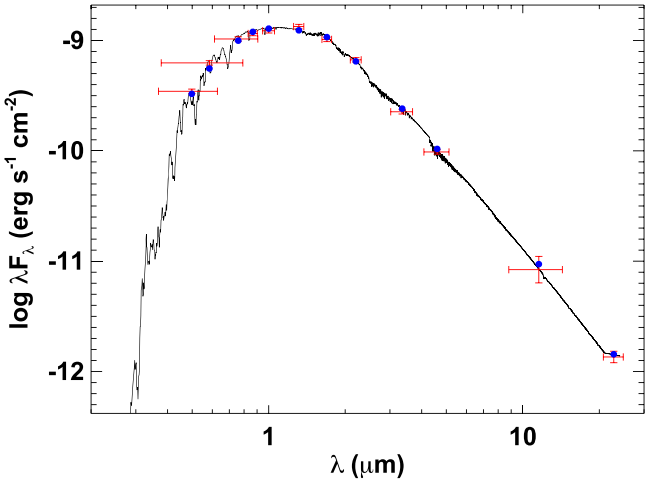

Figure 20. SED fit for our newly validated systems. Red symbols represent the observed photometric measurements, where the horizontal bars represent the effective width of the passband. Blue symbols are the model fluxes from the best-fit Kurucz atmosphere model (black). The complete figure set (five or six figures) is available in the online journal.

(The complete figure set (5 images) is available.)

Appendix D
Phase-folded Data and Models

Phase-folded light curves and models centered around the time of mid-transit for both CHEOPS and TESS light curves, including residuals around the HOMEBREW joint model.

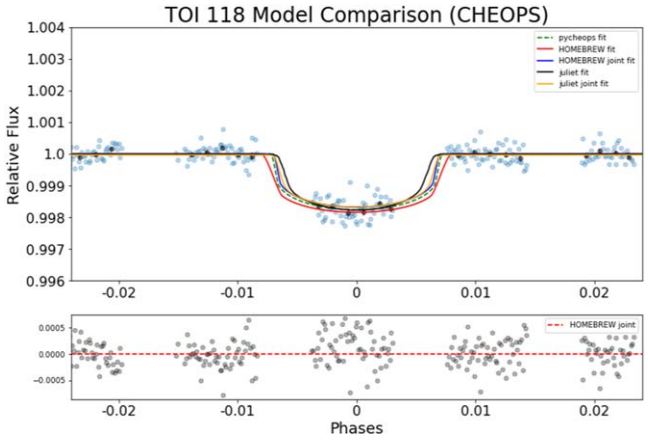

Figure 21. Phase-folded fits and photometry for our targets. The complete figure set (21 figures) is available in the online journal.

(The complete figure set (21 images) is available.)

In this Appendix, we show our various transit models fitted to the *CHEOPS* and *TESS* photometry, phase-folded to the mid-transit time (Figure 21). Additionally, we show residuals from the HOMEBREW joint model below the fits.

Appendix E
Corner Plots for HOMEBREW Joint Fits

In this Appendix, we show corner plots for our HOMEBREW joint fit MCMC runs (Figure 21).

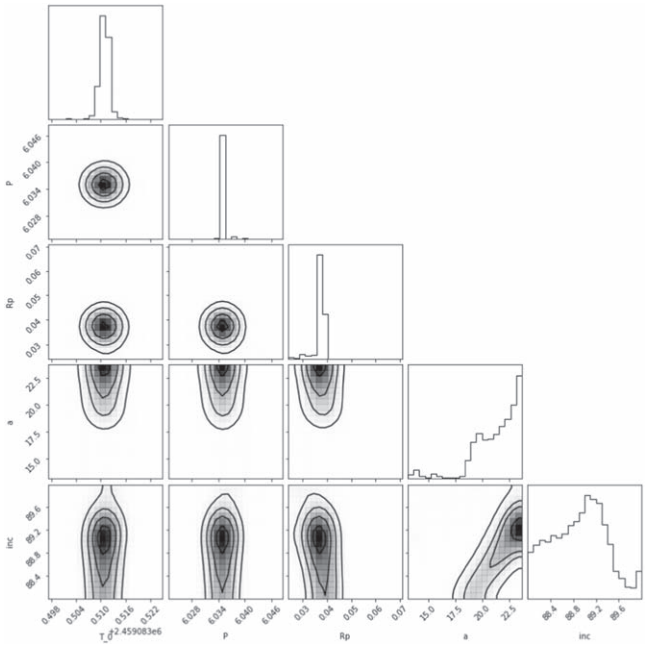

Figure 22. Corner plots for our HOMEBREW joint fits. The complete figure set (10 figures) is available in the online journal.

(The complete figure set (10 images) is available.)

ORCID iDs

Dominic Oddo https://orcid.org/0000-0002-2702-7700
Diana Dragomir https://orcid.org/0000-0003-2313-467X
Alexis Brandeker https://orcid.org/0000-0002-7201-7536
Hugh P. Osborn https://orcid.org/0000-0002-4047-4724
Karen Collins https://orcid.org/0000-0001-6588-9574
Keivan G. Stassun https://orcid.org/0000-0002-3481-9052
Nicola Astudillo-Defru https://orcid.org/0000-0002-8462-515X
Allyson Bieryla https://orcid.org/0000-0001-6637-5401
Steve B. Howell https://orcid.org/0000-0002-2532-2853
David R. Ciardi https://orcid.org/0000-0002-5741-3047
Samuel Quinn https://orcid.org/0000-0002-8964-8377
Jose M. Almenara https://orcid.org/0000-0003-3208-9815
César Briceño https://orcid.org/0000-0001-7124-4094
Kevin I. Collins https://orcid.org/0000-0003-2781-3207
Knicole D. Colón https://orcid.org/0000-0001-8020-7121
Dennis M. Conti https://orcid.org/0000-0003-2239-0567
Nicolas Crouzet https://orcid.org/0000-0001-7866-8738
Elise Furlan https://orcid.org/0000-0001-9800-6248
Tianjun Gan https://orcid.org/0000-0002-4503-9705
Crystal L. Gnilka https://orcid.org/0000-0003-2519-6161
Robert F. Goeke https://orcid.org/0000-0003-1748-5975
Jon M. Jenkins https://orcid.org/0000-0002-4715-9460
Eric L. N. Jensen https://orcid.org/0000-0002-4625-7333
David Latham https://orcid.org/0000-0001-9911-7388
Nicholas Law https://orcid.org/0000-0001-9380-6457
Michael B. Lund https://orcid.org/0000-0003-2527-1598
Andrew W. Mann https://orcid.org/0000-0003-3654-1602
Bob Massey https://orcid.org/0000-0001-8879-7138
Felipe Murgas https://orcid.org/0000-0001-9087-1245
George Ricker https://orcid.org/0000-0003-2058-6662
Pamela Rowden https://orcid.org/0000-0002-4829-7101
Richard P. Schwarz https://orcid.org/0000-0001-8227-1020
Joshua Schlieder https://orcid.org/0000-0001-5347-7062
Avi Shporer https://orcid.org/0000-0002-1836-3120
Sara Seager https://orcid.org/0000-0002-6892-6948
Guillermo Torres https://orcid.org/0000-0002-5286-0251
Joseph D. Twicken https://orcid.org/0000-0002-6778-7552
Roland Vanderspek https://orcid.org/0000-0001-6763-6562
Joshua N. Winn https://orcid.org/0000-0002-4265-047X

References

Al, Z. E. 2020, The Fourth U.S. Naval Observatory CCD Astrograph Catalog, IPAC, doi:10.26131/IRSA17
Astropy Collaboration, Price-Whelan, A. M., Lim, P. L., et al. 2022, ApJ, 935, 167
Astropy Collaboration, Price-Whelan, A. M., Sipőcz, B. M., et al. 2018, AJ, 156, 123
Astropy Collaboration, Robitaille, T. P., Tollerud, E. J., et al. 2013, A&A, 558, A33
Astudillo-Defru, N., Forveille, T., Bonfils, X., et al. 2017, A&A, 602, A88
Barragán, O., Armstrong, D. J., Gandolfi, D., et al. 2022, MNRAS, 514, 1606
Bean, J. L., Raymond, S. N., & Owen, J. E. 2021, JGRE, 126, e2020JE006639
Benz, W., Broeg, C., Fortier, A., et al. 2021, ExA, 51, 109
Berger, T. A., Huber, D., Gaidos, E., van Saders, J. L., & Weiss, L. M. 2020, AJ, 160, 108
Bonfanti, A., Delrez, L., Hooton, M. J., et al. 2021, A&A, 646, A157
Bouchy, F., Pepe, F., & Queloz, D. 2001, A&A, 374, 733
Broeg, C., Fortier, A., Ehrenreich, D., et al. 2013, EPJ Web Conf., 47, 03005
Brown, T. M., Baliber, N., Bianco, F. B., et al. 2013, PASP, 125, 1031
Buchhave, L. A., Bakos, G. Á., Hartman, J. D., et al. 2010, ApJ, 720, 1118
Buchhave, L. A., Latham, D., Johansen, A., et al. 2012, Natur, 486, 375
Castelli, F., & Kurucz, R. L. 2003, in IAU Symp. 210, Modelling of Stellar Atmospheres, ed. N. Piskunov, W. W. Weiss, & D. F. Gray (San Francisco, CA: ASP), A20
Chen, J., & Kipping, D. 2016, ApJ, 834, 17
Chouqar, J., Benkhaldoun, Z., Jabiri, A., et al. 2020, MNRAS, 495, 962
Ciardi, D. R., Beichman, C. A., Horch, E. P., & Howell, S. B. 2015, ApJ, 805, 16
Collins, K. 2019, AAS Meeting Abstracts, 233, 140.05
Collins, K. A., Kielkopf, J. F., Stassun, K. G., & Hessman, F. V. 2017, AJ, 153, 77
Dekany, R., Roberts, J., Burruss, R., et al. 2013, ApJ, 776, 130
Dressing, C. D., Charbonneau, D., Dumusque, X., et al. 2015, ApJ, 800, 135
Engle, S. G., & Guinan, E. F. 2018, RNAAS, 2, 34
Espinoza, N., & Jordán, A. 2016, MNRAS, 457, 3573
Espinoza, N., Kossakowski, D., & Brahm, R. 2019, MNRAS, 490, 2262
Esposito, M., Armstrong, D. J., Gandolfi, D., et al. 2019, A&A, 623, A165
Fűrész, G. 2008, PhD thesis, Univ. Szeged, Hungary
Findeisen, K., Hillenbrand, L., & Soderblom, D. 2011, AJ, 142, 23
Foreman-Mackey, D. 2016, JOSS, 1, 24
Foreman-Mackey, D., Hogg, D. W., Lang, D., & Goodman, J. 2013, PASP, 125, 306
Fulton, B. J., & Petigura, E. A. 2018, AJ, 156, 264
Fulton, B. J., Petigura, E. A., Blunt, S., & Sinukoff, E. 2018, PASP, 130, 044504
Furlan, E., Ciardi, D. R., Everett, M. E., et al. 2017, AJ, 153, 71
Furlan, E., & Howell, S. B. 2020, ApJ, 898, 47
Gaia Collaboration 2018, Gaia Source Catalogue DR2, IPAC, doi:10.26131/IRSA12
Gaia Collaboration 2020, Tycho-Gaia Astrometric Solution (TGAS) Source Table, IPAC, doi:10.26131/IRSA15

Gangestad, J. W., Henning, G. A., Persinger, R. R., & Ricker, G. R. 2013, arXiv:1306.5333
Garai, Z., Pribulla, T., Kovács, J., et al. 2022, MNRAS, 513, 2822
Giacalone, S., & Dressing, C. D. 2022, triceratops: Candidate Exoplanet Rating Tool, Astrophysics Source Code Library, ascl:2002.004
Giacalone, S., Dressing, C. D., Jensen, E. L. N., et al. 2021, AJ, 161, 24
Guerrero, N. M., Seager, S., Huang, C. X., et al. 2021, ApJS, 254, 39
Harris, C. R., Millman, K. J., van der Walt, S. J., et al. 2020, Natur, 585, 357
Hayward, T. L., Brandl, B., Pirger, B., et al. 2001, PASP, 113, 105
Hestroffer, D. 1997, A&A, 327, 199
Hippke, M., David, T. J., Mulders, G. D., & Heller, R. 2019, AJ, 158, 143
Howell, S. B., Everett, M. E., Sherry, W., Horch, E., & Ciardi, D. R. 2011, AJ, 142, 19
Howell, S. B., & Furlan, E. 2022, FrASS, 9, 871163
Howell, S. B., Matson, R. A., Ciardi, D. R., et al. 2021a, AJ, 161, 164
Howell, S. B., Scott, N. J., Matson, R. A., et al. 2021b, FrASS, 8, 10
Hoyer, S., Bonfanti, A., Leleu, A., et al. 2022, A&A, 668, A117
Hoyer, S., Guterman, P., Demangeon, O., et al. 2020, A&A, 635, A24
Huang, C. X., Vanderburg, A., Pál, A., et al. 2020a, RNAAS, 4, 204
Huang, C. X., Vanderburg, A., Pál, A., et al. 2020b, RNAAS, 4, 206
Hunter, J. D. 2007, CSE, 9, 90
Husser, T. O., Wende-von Berg, S., Dreizler, S., et al. 2013, A&A, 553, A6
Irwin, J. M., Charbonneau, D., Esquerdo, G. A., et al. 2018, AJ, 156, 140
Jenkins, J. M. 2002, ApJ, 575, 493
Jenkins, J. M., Chandrasekaran, H., McCauliff, S. D., et al. 2010, Proc. SPIE, 7740, 77400D
Jenkins, J. M., Tenenbaum, P., Seader, S., et al. 2020, Kepler Data Processing Handbook: Transiting Planet Search, Kepler Science Document KSCI-19081-003 (Washington, DC: NASA)
Jenkins, J. M., Twicken, J. D., McCauliff, S., et al. 2016, Proc. SPIE, 9913, 99133E
Jensen, E. 2013, Tapir: A Web Interface for Transit/Eclipse Observability, Astrophysics Source Code Library, ascl:1306.007
Kanodia, S., Wolfgang, A., Stefansson, G. K., Ning, B., & Mahadevan, S. 2019, ApJ, 882, 38
Kreidberg, L. 2015, PASP, 127, 1161
Kurucz, R. L. 1992, in The Stellar Populations of Galaxies, ed. B. Barbuy & A. Renzini, Vol. 149 (Angra dos Reis, Brazil: IAU), 225
Lester, K. V., Matson, R. A., Howell, S. B., et al. 2021, AJ, 162, 75
Li, J., Tenenbaum, P., Twicken, J. D., et al. 2019, PASP, 131, 024506
Lightkurve Collaboration, Cardoso, J. V. D. M., Hedges, C., et al. 2018, Lightkurve: Kepler and TESS Time Series Analysis in Python, Astrophysics Source Code Library, ascl:1812.013
Luque, R., & Pallé, E. 2022, Sci, 377, 1211
Luque, R., Pallé, E., Kossakowski, D., et al. 2019, A&A, 628, A39
MacDonald, M. G. 2019, MNRAS, 487, 5062
Mamajek, E. E., & Hillenbrand, L. A. 2008, ApJ, 687, 1264
Mann, A. W., Dupuy, T., Kraus, A. L., et al. 2019, ApJ, 871, 63
Matson, R. A., Howell, S. B., Horch, E. P., & Everett, M. E. 2018, AJ, 156, 31
Maxted, P. F. L., Ehrenreich, D., Wilson, T. G., et al. 2022, MNRAS, 514, 77
Maxted, P. F. L., & Gill, S. 2019, A&A, 622, A33
McCully, C., Volgenau, N. H., Harbeck, D.-R., et al. 2018, Proc. SPIE, 10707, 107070K
Morello, G., Tsiaras, A., Howarth, I. D., & Homeier, D. 2017, AJ, 154, 111
Morris, B. M., Heng, K., Brandeker, A., Swan, A., & Lendl, M. 2021, A&A, 651, L12
Mugrauer, M., & Michel, K.-U. 2020, AN, 341, 996
Mugrauer, M., & Michel, K.-U. 2021, AN, 342, 840
Mulders, G. D., Pascucci, I., & Apai, D. 2015, ApJ, 814, 130
Müller, H. M., Huber, K. F., Czesla, S., Wolter, U., & Schmitt, J. H. M. M. 2013, A&A, 560, A112
NASA Exoplanet Science Institute 2020, Planetary Systems Table, IPAC, doi:10.26133/NEA12
Neilson, H. R., McNeil, J. T., Ignace, R., & Lester, J. B. 2017, ApJ, 845, 65
NExScI 2022, Exoplanet Follow-up Observing Program Web Service, IPAC, doi:10.26134/EXOFOP5
Ning, B., Wolfgang, A., & Ghosh, S. 2018, ApJ, 869, 5
Paredes, L. A., Henry, T. J., Quinn, S. N., et al. 2021, AJ, 162, 176
Parviainen, H. 2015, PyLDTk: Python Toolkit for Calculating Stellar Limb Darkening Profiles and Model-specific Coefficients for Arbitrary Filters, Astrophysics Source Code Library, ascl:1510.003
Parviainen, H., & Aigrain, S. 2015, MNRAS, 453, 3821
Parviainen, H., Wilson, T. G., Lendl, M., et al. 2022, A&A, 668, A93
Pepe, F., Cristiani, S., Rebolo, R., et al. 2013, Msngr, 153, 6
Pepe, F., Cristiani, S., Rebolo, R., et al. 2021, A&A, 645, A96
Petigura, E. A., Rogers, J. G., Isaacson, H., et al. 2022, AJ, 163, 179
Pont, F., Zucker, S., & Queloz, D. 2006, MNRAS, 373, 231
Ricker, G. R., Winn, J. N., Vanderspek, R., et al. 2014, JATIS, 1, 014003
Sandstrom, K. 2019, z = 0 Multiwavelength Galaxy Synthesis, IPAC, doi:10.26131/IRSA6
Schlegel, D. J., Finkbeiner, D. P., & Davis, M. 1998, ApJ, 500, 525
Scott, N. J., Howell, S. B., Gnilka, C. L., et al. 2021, FrASS, 8, 138
Serrano, L. M., Gandolfi, D., Hoyer, S., et al. 2022, A&A, 667, A1
Skrutskie, M. F., Cutri, R.M., Stiening, R., et al. 2003, 2MASS All-Sky Point Source Catalog, IPAC, doi:10.26131/IRSA2
Smith, J. C., Stumpe, M. C., Cleve, J. E. V., et al. 2012, PASP, 124, 1000
Speagle, J. S. 2020, MNRAS, 493, 3132
Stassun, K. G., Collins, K. A., & Gaudi, B. S. 2017, AJ, 153, 136
Stassun, K. G., Corsaro, E., Pepper, J. A., & Gaudi, B. S. 2018, AJ, 155, 22
Stassun, K. G., Oelkers, R. J., Paegert, M., et al. 2019, AJ, 158, 138
Stassun, K. G., Oelkers, R. J., Pepper, J., et al. 2018, AJ, 156, 102
Stassun, K. G., & Torres, G. 2016, AJ, 152, 180
Stassun, K. G., & Torres, G. 2021, ApJL, 907, L33
Stumpe, M. C., Smith, J. C., Catanzarite, J. H., et al. 2014, PASP, 126, 100
Stumpe, M. C., Smith, J. C., Cleve, J. E. V., et al. 2012, PASP, 124, 985
Swain, M. R., Estrela, R., Sotin, C., Roudier, G. M., & Zellem, R. T. 2019, ApJ, 881, 117
Szabó, G. M., Gandolfi, D., Brandeker, A., et al. 2021, A&A, 654, A159
Tokovinin, A. 2018, PASP, 130, 035002
Tokovinin, A., Fischer, D. A., Bonati, M., et al. 2013, PASP, 125, 1336
Torres, G., Andersen, J., & Giménez, A. 2010, A&ARv, 18, 67
Trotta, R. 2007, MNRAS, 378, 72
Twicken, J. D., Catanzarite, J. H., Clarke, B. D., et al. 2018, PASP, 130, 064502
Van Eylen, V., Agentoft, C., Lundkvist, M. S., et al. 2018, MNRAS, 479, 4786
Wilson, T. G., Goffo, E., Alibert, Y., et al. 2022, MNRAS, 511, 1043
Winn, J. N., Holman, M. J., Torres, G., et al. 2008, ApJ, 683, 1076
Winters, J. G., Cloutier, R., Medina, A. A., et al. 2022, AJ, 163, 168
Winters, J. G., Medina, A. A., Irwin, J. M., et al. 2019, AJ, 158, 152
Wizinowich, P. L., Acton, D. S., Lai, O., et al. 2000, Proc. SPIE, 4007, 2
Wong, I., Kitzmann, D., Shporer, A., et al. 2021, AJ, 162, 127
Zeng, L., Jacobsen, S. B., Sasselov, D. D., et al. 2019, PNAS, 116, 9723
Zhou, G., Quinn, S. N., Irwin, J., et al. 2020, AJ, 161, 2
Zhou, G., Wirth, C. P., Huang, C. X., et al. 2022, AJ, 163, 289
Zhu, W., & Dong, S. 2021, ARA&A, 59, 291
Ziegler, C., Tokovinin, A., Briceño, C., et al. 2020, AJ, 159, 19